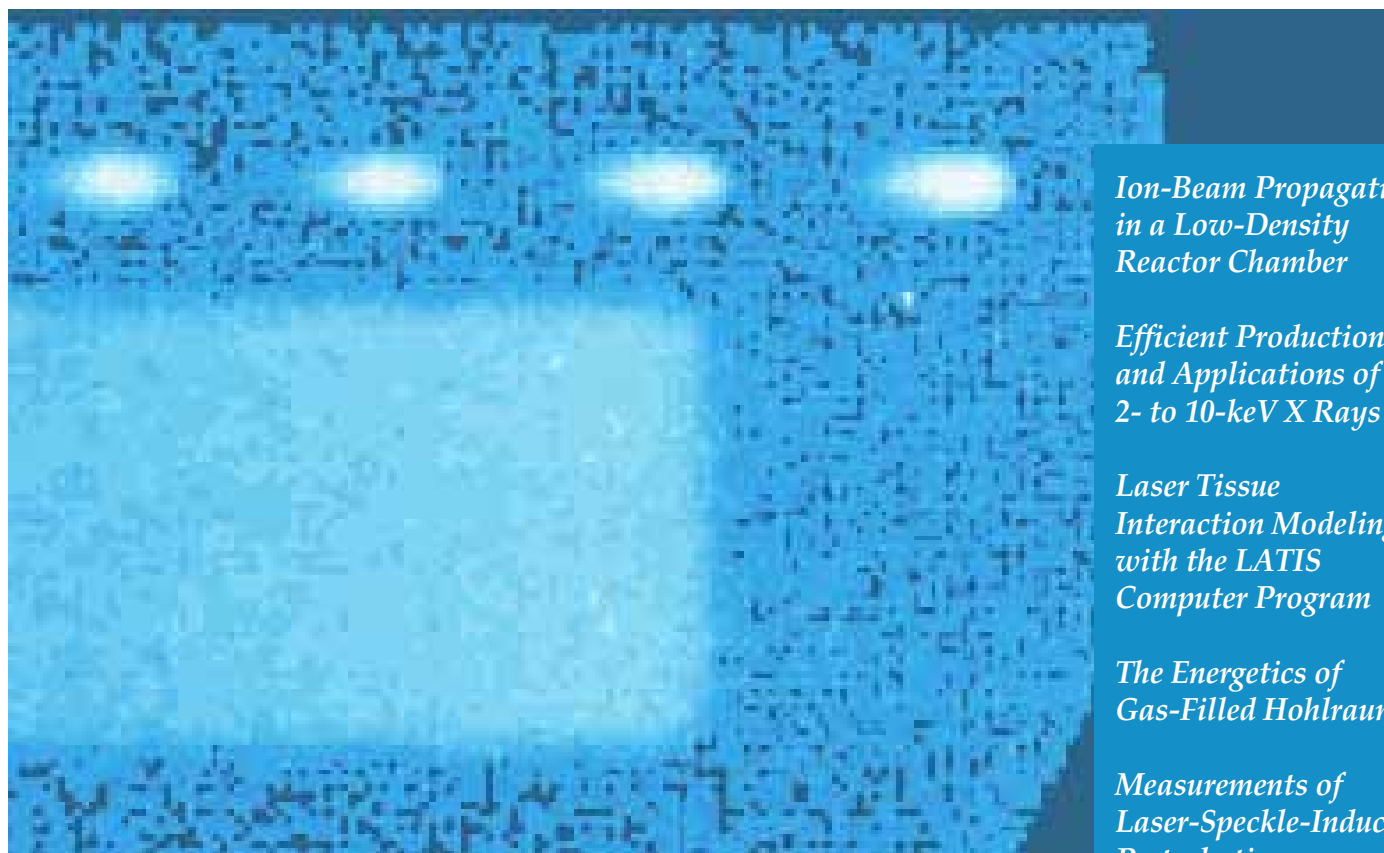


INERTIAL CONFINEMENT FUSION

Lawrence
Livermore
National
Laboratory

ICF Quarterly Report

April–June 1996, Volume 6, Number 3



*Ion-Beam Propagation
in a Low-Density
Reactor Chamber*

*Efficient Production
and Applications of
2- to 10-keV X Rays*

*Laser Tissue
Interaction Modeling
with the LATIS
Computer Program*

*The Energetics of
Gas-Filled Hohlraums*

*Measurements of
Laser-Speckle-Induced
Perturbations*

*Fusion Reaction-Rate Measurements —
Nova and NIF*

The Cover: Image of a time-resolved neutron signal and related timing pulses recorded with an LLNL optical streak camera. Clearly visible detector pixels in this magnified image and a low-level signal accent the statistical variation in the background region to create an interesting mosaic pattern. The encoded neutron signal shows an abrupt edge corresponding to the instant in which neutrons first reach the detector (time goes from right to left). Neutron signals like this are used to determine reaction rates with ~30 ps resolution for ICF targets. Evenly spaced pulses 500 ps apart (across top of image) are used to precisely time the neutron signal relative to the laser power irradiating a target. For details, see the article "Fusion Reaction-Rate Measurements—Nova and NIF," beginning on page 115.

UCRL-LR-105821-96-3
Distribution Category UC-712
April–June 1996

Printed in the United States of America
Available from
National Technical Information Service
U.S. Department of Commerce
5285 Port Royal Road
Springfield, Virginia 22161
Price codes: printed copy A03, microfiche A01.

This document was prepared as an account of work sponsored by an agency of the United States Government. Neither the United States Government nor the University of California nor any of their employees makes any warranty, express or implied, or assumes any legal liability or responsibility for the accuracy, completeness, or usefulness of any information, apparatus, product, or process disclosed, or represents that its use would not infringe privately owned rights. Reference herein to any specific commercial products, process, or service by trade name, trademark, manufacturer, or otherwise, does not necessarily constitute or imply its endorsement, recommendation, or favoring by the United States Government or the University of California. The views and opinions of authors expressed herein do not necessarily state or reflect those of the United States Government or the University of California and shall not be used for advertising or product endorsement purposes.

The ICF Quarterly Report is published four times each fiscal year by the Inertial Confinement Fusion Program at the Lawrence Livermore National Laboratory. The journal summarizes selected current research achievements of the LLNL ICF Program. The underlying theme for LLNL's ICF Program research is defined within DOE's Defense Programs missions and goals. In support of these missions and goals, the ICF Program advances research and technology development in major interrelated areas that include fusion target theory and design, target fabrication, target experiments, and laser and optical science and technology.

While in pursuit of its goal of demonstrating thermonuclear fusion ignition and energy gain in the laboratory, the ICF Program provides research and development opportunities in fundamental high-energy-density physics and supports the necessary research base for the possible long-term application of inertial fusion energy for civilian power production. ICF technologies continue to have spin-off applications for additional government and industrial use. In addition to these topics, the *ICF Quarterly Report* covers non-ICF funded, but related, laser research and development and associated applications. We also provide a short summary of the quarterly activities within Nova laser operations, Beamlet laser operations, and National Ignition Facility laser design.

LLNL's ICF Program falls within DOE's national ICF program that includes the Nova and Beamlet (LLNL), OMEGA (University of Rochester Laboratory for Laser Energetics), Nike (Naval Research Laboratory), and Trident (Los Alamos National Laboratory) laser facilities. The Particle Beam Fusion Accelerator and Saturn pulsed power facilities are at Sandia National Laboratory. General Atomics, Inc., develops and provides many of the targets for the above experimental facilities. Many of the *Quarterly Report* articles are co-authored with our colleagues from these other ICF institutions.

Questions and comments relating to the technical content of the journal should be addressed to the ICF Program Office, Lawrence Livermore National Laboratory, P.O. Box 808, Livermore, CA 94551.

Work performed under the auspices of the U.S. Department of Energy by Lawrence Livermore National Laboratory under Contract W-7405-Eng-48.

INERTIAL CONFINEMENT FUSION

ICF Quarterly Report

April–June 1996, Volume 6, Number 3

In this issue:

Foreword iii

Ion-Beam Propagation in a Low-Density Reactor Chamber for Heavy-Ion Fusion 89

We have assessed constraints of spot size and vacuum for ballistic transport of ion beams in inertial fusion energy reactors. We have simulated transport of a partially neutralized beam at low pressures and examined interactions of multiple beams. Further simulations show that partial beam neutralization allows higher chamber pressures and higher charge-to-mass ions, both of which allow for lower reactor cost.

Efficient Production and Applications of 2- to 10-KeV X Rays by Laser-Heated Underdense Radiators 96

The proposed National Ignition Facility (NIF) offers the prospect of producing up to several hundred kilojoules of multi-keV x rays. This may allow us to perform experiments and field diagnostics we could never consider with current laser facilities. We discuss applications of high-energy, multi-keV sources with the NIF.

Laser–Tissue Interaction Modeling with the LATIS Computer Program 103

A new computer program, based on many years of experience in laser-matter interaction modeling, is being used to design new laser-medical instruments and procedures.

The Energetics of Gas-Filled Hohlräume 110

We have measured the effect of gas-fill on the drive temperature in Nova scale-1 hohlraums. Increasing electron density results in a reduced drive temperature. A significant part of the reduced drive can be attributed to stimulated scattering of the incident laser light. This scattering may be reduced by beam smoothing.

Fusion Reaction-Rate Measurements—Nova and NIF 115

At Nova, we measure ICF targets' burn history with a resolution of <30 ps. Our neutron-based technique uses a fast-rise-time plastic scintillator and a high-speed optical streak camera. Measured burn durations range from ~50 ps to ~1 ns. For the NIF, we are investigating new measurement techniques based on gamma rays released in the fusion process.

Laser-Speckle-Induced Perturbations in Laser-Driven Foils 123

We have calibrated the amplitude and Rayleigh–Taylor growth of modulations imprinted by laser speckle in CH₂ foils with single-mode surface perturbations, converting the imprint to an equivalent surface finish. The addition of bandwidth and dispersion to the drive laser reduced the imprinted modulations, with the highest bandwidth showing the largest reduction in imprint, in agreement with LASNEX simulations.

Program Updates U-1

Publications P-1

Scientific Editor
Alan Burnham

Publication Editors
Jason Carpenter
Al Miguel
Ann Parker
Dabbie Schleich

Design Staff
Daniel Moore

Art Staff
Sandy Lynn
Linda Wiseman

FOREWORD

This issue of the *ICF Quarterly* presents a diverse set of articles ranging from interpretation of current Nova experiments to weapons effect testing on the proposed National Ignition Facility (NIF), to medical uses of lasers, and to inertial fusion energy (IFE) drivers.

The lead article, “Ion-Beam Propagation in a Low-Density Reactor Chamber for Heavy-Ion Inertial Fusion” (p. 89), explores the ability of heavy-ion beams to be adequately transported and focused in an IFE reactor. Such beams are a leading candidate for reactors because of their high efficiency, repetition rate, and lifetime. The vapor pressure of the molten chamber wall has the potential to prevent adequate beam focusing because of beam stripping, but the authors show that partial beam neutralization by several candidate techniques can overcome that problem. Neutralization also provides the possibility of using lower-cost, lighter-ion beams such as Cs^+ .

The next article, “Efficient Production and Applications of 2- to 10-KeV X Rays by Laser-Heated Underdense Radiators” (p. 96), explores the ability of the NIF to produce sufficient high-energy x rays for diagnostic backlighting, target preheating, or uniform irradiation of large test objects for Nuclear Weapons Effects Testing. The latter application illustrates the increasing emphasis of the NIF for nonignition experiments. By appropriate high-power illumination of low-density, high-Z materials, a considerable fraction of the laser energy can be converted into KeV x rays. For example, focusing six of the 10-TW 4-beamlet clusters on the NIF into a Xe-filled hohlraum would convert 30% of the laser energy into x rays with energies greater than 4 KeV and 48% into energies greater than 1 KeV.

For capsule implosion experiments, the increasing energies and distances involved in the NIF compared to Nova require the development of new diagnostics methods. The article “Fusion Reaction-Rate Measurements—Nova and NIF” (p. 115) first reviews the use of time-resolved neutron measurements on Nova to monitor fusion burn histories and then explores the limitations of that technique, principally Doppler broadening, for the proposed NIF. It also explores the use of gamma rays to follow burn history and reports the first measurement of ICF fusion gamma rays on Nova, thereby providing a proof-of-principle for using gamma rays for monitoring fusion burn histories on the NIF.

The articles “The Energetics of Gas-Filled Hohlraums” (p. 110) and “Measurements of Laser-Speckle-Induced Perturbations in Laser-Driven Foils” (p. 123) report measurements on Nova of two important aspects of implosion experiments. The first characterizes the amount of energy lost from a hohlraum by stimulated Brillouin and Raman scattering as a function of gas fill and laser-beam uniformity. Some amount of hohlraum gas fill is anticipated for indirectly driven implosions on the NIF in order to minimize x-ray drive asymmetry due to ablation of the hohlraum wall. Although energy losses by scattering up to 25% were observed for unsmoothed beams, scattering loss was reduced to about 5% for a single smoothed beam and a gas fill producing a plasma with 0.04 of its critical density. The second of these articles shows that the growth of density nonuniformities implanted on smooth capsule surfaces by laser speckle can be correlated with the effects of physical surface roughness. This work helps define the laser beam smoothness required for directly driven implosions.

The article “Laser-Tissue Interaction Modeling with the LATIS Computer Program” (p. 103), explores the use of modeling to enhance the effectiveness—maximize desired effects and minimize collateral damage—of lasers for medical purposes. The program LATIS, a two-dimensional, time-dependent simulation tool recently developed using the experience of LASNEX, is used to predict heat deposition and the resultant thermal, material, and hydrodynamic responses from lasers interacting with tissue. When fully developed and validated, LATIS can be used to optimize medical procedures such as photothermal therapy, tissue welding, hard-tissue ablation, and thrombolysis.

Alan Burnham
Scientific Editor

ION-BEAM PROPAGATION IN A LOW-DENSITY REACTOR CHAMBER FOR HEAVY-ION INERTIAL FUSION

D. A. Callahan

A. B. Langdon

Introduction

Heavy-ion fusion (HIF) is an attractive candidate for inertial fusion energy (IFE) production. In HIF, beams of heavy ions (mass ~ 100 to 200 amu) are accelerated and focused on an indirectly driven inertial confinement fusion (ICF) target. At the target, the ion energy is converted in a hohlraum into x rays, which implode the capsule. Accelerator drivers have the long lifetime (~ 30 years), high repetition rate (~ 5 Hz), and high efficiency ($\sim 30\%$) needed for commercial energy production. In addition, final focusing is accomplished via magnetic fields, which are not damaged by the blast.

The accelerator requirements are set by the target. In order to get efficient coupling of ion energy into x rays, the amount of radiator material in the target (Fig. 1) that needs to be heated must be kept reasonably small. Because the ions must be stopped in the target, the ion range (equal to the stopping distance times the material density) is related to the amount of material necessary. In order to keep the target mass reasonably small, an ion range ≤ 0.1 g/cm² is used. For ions of mass 100 to 200 amu, this corresponds to an ion energy of 3 to 10 GeV. To get the required beam power on target (5 to 10 MJ in 10 ns = 0.5 – 1.0×10^{15} W), the beam current must be greater than 50 kA. This current is broken into several beams to keep the space-charge forces manageable. In

most conventional ion accelerators, space-charge plays only a small role; in a HIF accelerator, space-charge is very important.

The gain of a heavy-ion target generally increases as the size of the beam focal spot decreases. In order to get a small spot (radius ~ 2 to 5 mm), the beam emittance must be kept small. The beam emittance (a term used in accelerator physics) is proportional to the phase space area occupied by the beam and is related to the beam temperature. Keeping the emittance small throughout the accelerator in the presence of nonlinear fields (resulting from imperfect accelerator elements, misalignments, fringe fields, etc.) while performing the necessary beam manipulations (beam bending, beam combining, etc.) is a challenge. Recent *Quarterly* articles by W. M. Sharp¹ and A. Friedman² discuss issues and progress towards understanding the accelerator needed for a HIF power plant.

Once the beams leave the accelerator, they must be focused and transported through the reactor chamber to the target. Transporting the heavy-ion beams from the accelerator to the target is extremely important for a successful HIF reactor. Chamber transport (along with the target) sets the requirements on the accelerator driver.³ As a result, improvements in chamber transport and final focus can significantly reduce the cost of electricity. Relaxing the requirements on the accelerator reduces the cost of the driver, which directly impacts the cost of electricity; reducing the beam spot size at the target allows a larger target gain, which also reduces the cost of electricity. Improvements in beam transport and final focusing can be exploited in optimizing the end-to-end HIF system.

The main-line approach to chamber transport is low-density, ballistic or nearly ballistic transport. The HYLIFE-II reactor⁴ uses a low-density chamber with a pressure of a few millitorr. Even at the low density of the HYLIFE-II chamber (5×10^{13} cm⁻³ ≈ 0.003 torr), partial beam-charge neutralization is needed to overcome

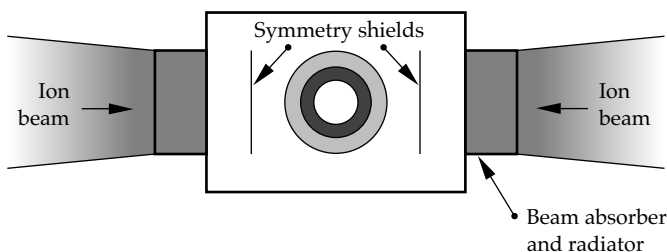


FIGURE 1. Schematic IFE heavy-ion indirect-drive target with end radiators. (40-00-1096-2401pb01)

the effects of beam stripping. In this case, beam stripping refers to collisional ionization of the beam ions to a higher charge state by the background gas. Beam stripping and neutralization have been recognized as important issues in chamber transport for many years.^{4,5} Low-density transport is the most conservative option, but puts strict requirements on the beam quality out of the accelerator.

In this article, we first discuss different effects that impact the beam spot size at the target. We then show that ballistic transport in a near vacuum is possible, but puts undesirable constraints on the reactor chamber design. We then discuss simulations of partially neutralized beam transport in a low-density chamber. Finally, we discuss calculations of multiple beam effects in the chamber. Partial neutralization allows chamber operation at higher pressures, and the use of ions with higher charge-to-mass ratio which are easier to accelerate. Both increases in flexibility allow for lower reactor cost.

Total Beam Spot Size at the Target

In this section we describe the different effects that lead to the final beam spot size at the target. The beam spot size is increased by the beam's space charge and emittance, chromatic aberrations in the final focusing system, and errors in aiming the beams at the target. These sources are roughly independent and add in quadrature,⁶

$$r_{\text{target}}^2 \approx r_s^2 + r_c^2 + r_a^2, \quad (1)$$

where r_{target} is the final spot radius at the target, and r_s , r_c , and r_a are the spot radius due to space charge and emittance, chromatic aberrations, and aiming, respectively. The simulation results presented in the sections below do not include chromatic aberrations or aiming errors; Eq. (1) is used to estimate the total spot radius. The spot radius necessary for a high gain (≥ 40) ranges from 2 to 6 mm depending on the details of the target design.

In the HYLIFE-II reactor concept, the targets are injected into the chamber at a rate of six per second using a gas gun. Petzoldt⁷ estimates that the spot radius due to errors in aiming the beams at the target is 0.4 mm. This estimate takes into account translational positioning errors and rotations of the target.

Chromatic aberrations occur in the final focusing system because particles with different longitudinal momenta are focused at different distances. This causes a radial spread in the particles at target, which is proportional to $\delta p/p$, the longitudinal momentum spread divided by the longitudinal momentum. For a focusing system of four thin lenses, single-particle calculations (neglecting space charge) show that $r_c = 8F\theta\delta p/p$, where F is the focal distance, and θ is the half convergence

angle of the beam. Including space charge reduces the chromatic aberrations by about a factor of 3/4, so

$$r_c \approx 6F\theta \frac{\delta p}{p}. \quad (2)$$

Generally F is set by the reactor geometry and has a value of ~ 5 m. The convergence angle θ is generally limited to ~ 15 mrad to avoid geometric aberrations in the final focusing magnets. It is possible to use larger angles and correct the geometric aberrations using an octupole correction.⁸ A larger convergence angle results in a larger aperture for the final focusing magnets, however, which increases the cost of those magnets. For the purposes of these calculations, we will keep $\theta \approx 15$ mrad.

Limiting the spot radius from chromatic aberrations to 1 to 1.5 mm sets a limit on the allowable momentum spread in the final focusing system. Using $F = 5$ m and $\theta = 15$ mrad, we find $\delta p/p \leq 2.2 - 3.3 \times 10^{-3}$ in the final focusing system. In the conventional HIF driver scenario, the beam is drift compressed by a factor of 10 or more between the end of the accelerator and the final focusing system. This is accomplished by giving the beam a velocity "tilt" so that the beam tail is moving faster than the beam head. After the tilt is applied, the beam is allowed to drift and it compresses as the tail catches up with the head. This drift compression increases the longitudinal momentum spread, and, as a result, $\delta p/p \leq 2.2 - 3.3 \times 10^{-4}$ at the end of the accelerator if the beam is to be drift-compressed by a factor of 10 prior to focusing.

If $r_a = 0.4$ mm, and $r_c = 1.5$ mm, then 2.57 mm are left for space charge and emittance (r_s) in a total spot (r_{target}) of 3 mm. An optimization needs be done to weigh the relative costs of each of the spot size contributions. We need to assess the cost of increasing $\delta p/p$ at the expense of beam emittance, for example.

The beam-spot radius from space charge and emittance can be estimated using the envelope equation

$$a'' = \frac{K}{a} + \frac{\epsilon^2}{a^3}, \quad (3)$$

where each ' indicates a derivative with respect to z , K is the perveance (which is a measure of the beam's space charge), ϵ is the unnormalized emittance, and a is the beam edge radius. Multiplying by a' and integrating gives

$$(a_f')^2 - (a_0')^2 = 2K \ln\left(\frac{a_f}{a_0}\right) - \epsilon^2 \left(\frac{1}{a_f^2} - \frac{1}{a_0^2}\right) \quad (4)$$

where 0 and f denote the initial and final values. At the beam waist $a_f = r_s$ and $a_f' = 0$. At the entrance,

$a'_0 = \theta$ and $a_0 \approx F\theta$. Using these substitutions and assuming $a_0 \gg r_s$, Eq. (4) becomes

$$\theta^2 = 2K \ln\left(\frac{a_0}{r_s}\right) + \frac{\varepsilon^2}{r_s^2}. \quad (5)$$

In the absence of space charge (i.e., a perfectly neutralized beam), $K = 0$ and the spot radius due to emittance r_e is given by

$$r_e = \frac{\varepsilon}{\theta}. \quad (6)$$

If $r_e = 1$ mm and $\theta = 15$ mrad, then transverse beam emittance is restricted to $\varepsilon \leq 15$ mm-mrad.

Using Eq. (5), we can estimate the maximum beam perveance allowed for a given r_s . Using $\theta = 15$ mrad, $a_0 = 7.5$ cm, $r_s = 2.5$ mm, and $\varepsilon = 15$ mm-mrad, Eq. (5) gives a maximum perveance of $K = 2.8 \times 10^{-5}$. The perveance is related to the beam current by

$$K = \frac{2Z}{(\gamma\beta)^3 A} \frac{I_b}{I_0}, \quad (7)$$

where Z is the ion charge state, β is the beam velocity over the speed of light, γ is the Lorentz factor, I_b is the beam current, A is the ion mass in amu, and $I_0 = m_{\text{amu}} c^3 / e = 31$ MA. For $K = 2.8 \times 10^{-5}$, this leads to a maximum current per beam of 2.3 kA for a mass-200 ion and 1.6 kA for a mass-135 ion, both at $\beta\gamma = 0.3$. Neutralization is needed if the current per beam is larger than these values.

Ballistic Transport in a Near Vacuum

Using the equations introduced in the previous section, we can show that a beam of 10-GeV, singly charged, heavy (~ 200 -amu) ions can be ballistically transported with a reasonable spot size provided the chamber density is low enough to avoid beam stripping. The target requires a main pulse with 4 MJ of energy in 10 ns (an additional 1 MJ is carried by a low-power prepulse). The total current necessary in the main pulse is $4 \text{ MJ} / (10 \text{ GeV} \times 10 \text{ ns}) = 40$ kA. Without neutralization, the maximum current per beam found in the previous section was 2.3 kA, so 17 beams are needed for the main pulse. This provides a reasonable, conservative scenario for transporting the beam to the target.

Beam stripping is an issue, however. Estimates of the cross section⁹⁻¹¹ for stripping the beam ions by the background gas in HYLIFE-II (BeF_2 from the

molten LiF-BeF_2 chamber wall) range from 1.3 to $4.0 \times 10^{-16} \text{ cm}^2$. Stripping only about 1% of the beam ions requires a chamber density $\approx 10^{11} \text{ cm}^{-3}$. This density is two orders of magnitude below the chamber density in the HYLIFE-II reactor ($\approx 5 \times 10^{13} \text{ cm}^{-3}$). Since a HIF reactor has a repetition rate of about 5 Hz, it is difficult to achieve densities lower than used in HYLIFE-II after each shot. Thus, purely ballistic transport puts an undesirable restriction on the chamber density.

Low-Density, Nearly Ballistic Transport

One option for improving the beam focus at the density of HYLIFE-II is to partially charge neutralize the beam. At the density of the HYLIFE-II chamber, the stripping mean-free-path is 0.5 to 1.5 m. In the HYLIFE-II design, the chamber radius from “first wall” to the target is 3 m (from target to the center of the last focusing magnets is about 5 m, as used in the “Total Beam Spot Size at the Target” section). Therefore, the beam will strip 2 to 6 times during chamber transport. Simulations with the BICrz code¹²⁻¹⁵ show that most of the stripped electrons tend to stay with the beam. However, in the higher charge state, the ions respond more strongly to the electric fields and the spot size increases. Simulations with a stripping mean-free-path of 1.2 m in a 3-m chamber show an increase in the beam spot radius from 2.6 mm (vacuum transport) to 8 mm. This is an unacceptably large spot, and partial beam neutralization must be used to offset this increase.

While beam stripping makes chamber propagation more difficult, ionization of the background gas by the beam ions can partially neutralize the beam and aid transport. Cross sections for collisional ionization of BeF_2 by the beam have a larger uncertainty than stripping cross sections because calculating molecular cross sections is more difficult than calculating atomic cross sections. Estimates of the mean-free-path for ionizing the background gas range from 0.7 to 25 m. For BeF_2 , the ratio of stripping to gas ionization cross sections is not favorable (i.e., more stripping than gas ionization). Other chamber gases, such as Li, may have a more favorable cross section ratio.¹⁶

Simulations show that including a stripping mean-free-path of 1.2 m and a gas ionization mean-free-path of 3.0 m reduced the spot radius from 8 to 5.4 mm. Neutralization by gas ionization occurs “for free” since we do not have to add anything to the reactor for it to occur; however, gas ionization neutralizes the beam slowly, so radial velocities develop before neutralization occurs. The solid

curve in Fig. 2 shows the neutralization fraction as a function of distance from the chamber wall for a simulation without beam stripping. The beam is more than 70% neutralized, but it takes about 2.5 m of propagation distance to reach this level of neutralization. To get a smaller spot, additional neutralization is needed.

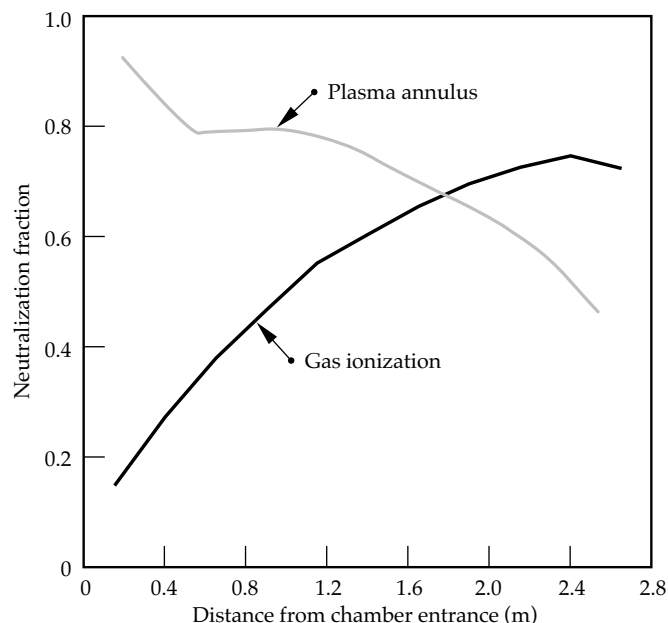


FIGURE 2. Neutralization fraction as a function of distance from the chamber entrance for neutralization using collisional ionization of the background gas (black curve) and neutralization using a preformed plasma annulus in the chamber (gray curve). (50-00-0696-1362pb01)

Neutralization Using a Preformed Plasma Annulus

Neutralizing an ion beam is more difficult than neutralizing an electron beam. When an electron beam passes through a plasma, the plasma electrons are moved out of the beam path, and the beam is neutralized by the immobile ions. For an ion beam, however, electrons must be pulled in from outside the beam path in order to reduce the net charge.

One method for neutralizing the beam quickly is to create a preformed plasma in the chamber before the beam enters. Simulations used a small ($0.3\text{-m} = 40\%$ of the beam length) annulus of plasma just inside the chamber entrance. A 4-kA beam of Pb^+ ions entered the chamber through the annulus. The annulus had a total electron charge of four times the beam charge.

As the beam entered the chamber, electrons were pulled from the inner surface of the annulus by the large radial electric field of the beam ($E_r = 16\text{ MV/m}$ at the beam edge for a 4-kA beam of radius 5 cm). The

electrons are accelerated longitudinally by the z electric field of the beam and oscillate back and forth across the beam in both the radial and longitudinal direction. The details of the acceleration and deceleration of the electrons in the longitudinal direction will depend on the shape of the beam. These simulations used a beam with a current profile that was parabolic in z .

Because the BICrz code is axisymmetric, particles cannot gain or lose angular momentum. The only angular momentum a particle has is the momentum it is created with. For the plasma annulus, we used an initial isotropic temperature of 100 eV. The particles can heat in r and z , but not in θ . As a result, a temperature anisotropy develops, which causes an excess of electrons near the axis. This causes the radial fields to become nonlinear. Figure 3 shows the radial velocity

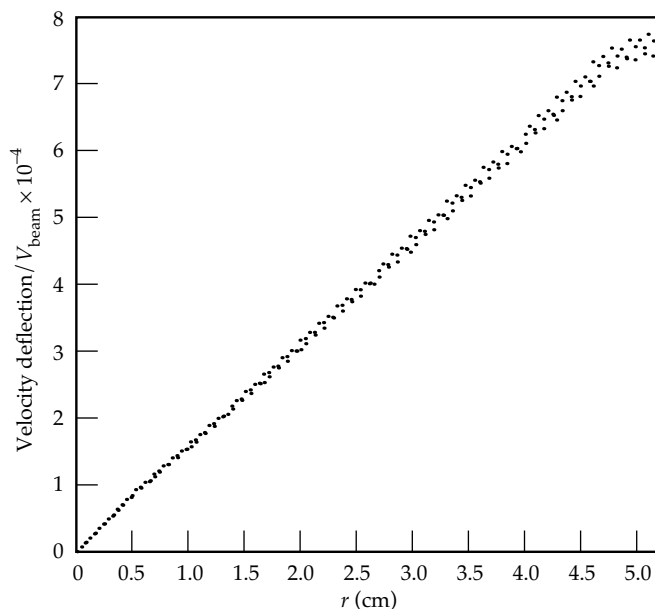


FIGURE 3. The radial velocity deflection of particles near the axial center of the beam as a function of radius shows the electric field is linear when no electrons are present. (50-00-0696-1363pb01)

deflection of particles near the center of the beam as a function of radius when no electrons are present. As expected, the field is linear. Figure 4 shows the same plot when the beam has passed through a plasma annulus (but with no beam stripping). The field is greatly reduced from the previous case, but the nonlinearity is also apparent. Because of the abundance of electrons near the axis, the field is negative at small radii. We can compensate for linear fields by increasing the focusing angle at the final optic. We cannot compensate for the nonlinear fields in this way; as a result the nonlinear fields can make it more difficult to focus the beam.

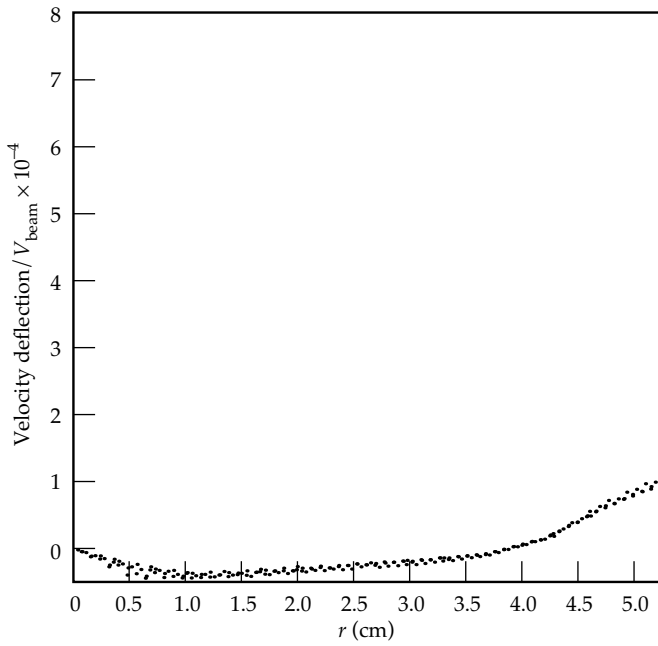


FIGURE 4. When electrons are present, the radial velocity deflection of particles near the axial center of the beam as a function of radius shows that the electric field is reduced, but nonlinear. (50-00-0696-1364pb01)

The charge neutralization fraction can be estimated using the Child–Langmuir space-charge-limited current from the inner surface of the annulus. For the 0.5-cm gap between the beam radius and the inner edge of the annulus used in this simulation, this estimate yields a neutralization fraction of 90%. Simulations are in agreement with this estimate, and the gray curve in Fig. 2 shows that the beam is quickly neutralized to slightly more than 90% while inside the annulus. As expected, neutralization reduces the beam spot size at the target. In a simulation with a stripping mean-free-path of 1.2 m and a plasma annulus, the final spot was 3.5 mm. This is a significant decrease over the 8-mm spot found without neutralization, but is not as good as the pure vacuum transport result of 2.6 mm.

The gray curve in Fig. 2 shows that while the beam is well neutralized near the chamber entrance, it does not remain well neutralized. The electrons pulled in from the plasma annulus are hot ($v_{th} \approx 0.3c$). As the beam compresses, the electrons do not compress as readily as the beam, and the neutralization fraction falls off as the beam approaches the target. The fact that these electrons are hot and as a result do not neutralize well near the target was seen in earlier studies.^{17,18} Electrons created by collisional ionization of the background gas are cooler than those pulled in from the plasma annulus, and we expect the smallest spot when both collisional ionization and a plasma annulus are included. Simulations confirm this, and the spot is reduced from 3.5 to 3.0 mm when a gas ionization mean-free-path of 3 m is added to the simulation.

Neutralization Using a Plasma Column

In the case of the plasma annulus, neutralization was quite good (>90%) inside the annulus, but the neutralizing electrons did not compress with the beam. As a result, neutralization got worse as the beam got closer to the target. One method to remedy this problem is to put the plasma throughout the entire chamber so the beam can continually pull in new electrons as it compresses.

The plasma density required in the plasma column is not large. Simulations show that ionizing just 0.44% of the background gas ($n_e = 2.5 \times 10^{11} \text{ cm}^{-3}$) in a cylinder of radius $\sqrt{2r_{\text{beam, initial}}}$ is enough to eliminate the effects of beam stripping when the stripping mean-free-path is 1.2 m. In this case, the electron density was six times the initial beam density. As the beam compressed, the beam density became much larger than the electron density.

One method for reducing the cost of the driver is to use a lighter, lower-energy ion such as 5.3-GeV Cs^+ . The cost of using the lighter, lower-energy ion is that more current is necessary to deliver the same energy to the target. For 5.3-GeV Cs^+ , 75 kA of current is needed to provide 4 MJ of energy in the 10-ns main pulse. We found in the second section that the maximum current we can transport in the chamber for a mass-135 ion without neutralization is 1.6 kA per beam. This means we would need more than 45 unneutralized Cs beams. With about 80% neutralization, we can transport the 75 kA of Cs in 10 beams.

In the simulation, the low-density plasma column neutralized the Cs beam quite well. A simulation with a 7.5-kA beam of 5.3-GeV Cs^+ ions (without beam stripping) and a low-density plasma column ($n_e = 2.3 \times 10^{11} \text{ cm}^{-3}$) produced a spot of 1.2 mm. This simulation used a smaller emittance (15 mm-mrad) than was used in some of the previous cases (33 mm-mrad). For these parameters, the unneutralized beam spot radius was 9 mm and the perfectly neutralized spot radius (from emittance only) was 0.9 mm. Figure 5 shows

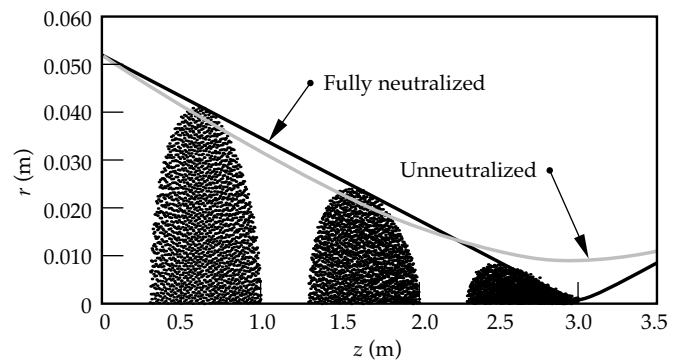


FIGURE 5. A particle-in-cell simulation shows that a 7.5-kA beam of 5.3-GeV Cs^+ ions is well neutralized by a low-density plasma column. The gray curve shows the envelope solution with no neutralization while the solid curve shows the envelope solution with perfect neutralization. (50-00-0696-1365pb01)

the simulation particles at three times plus the envelope solution for the unneutralized beam (gray curve) and the fully neutralized beam (black curve). The particles follow the fully neutralized envelope solution quite well indicating a high degree of neutralization.

Adding a beam stripping mean-free-path of 3.2 m to the Cs beam simulation produced a spot of 2 mm. This mean-free-path would correspond to a decrease of about a factor of two in the chamber density from the standard HYLIFE-II case.

Producing the plasma column in the HYLIFE-II chamber still needs to be addressed. Some methods under consideration are using an electrical discharge or a laser to ionize some of the chamber vapor and using a plasma gun to create the plasma and inject it in the chamber. Any equipment used to create the plasma (lenses, insulators, etc.) must be protected from the blast. This work is in progress.

Interactions Between Neighboring Beams

Most indirect-drive, HIF target designs have two radiation converters (one located at either end of the hohlraum). However, many beams (i.e., more than two) are necessary to reduce the space-charge forces. This means that half the beams will be aimed at each radiation converter, and these beams will be fairly close to one another in the chamber (see Fig. 6). As a result, each beam will be affected by the fields from neighboring beams, which can result in an increase in the beam spot size.

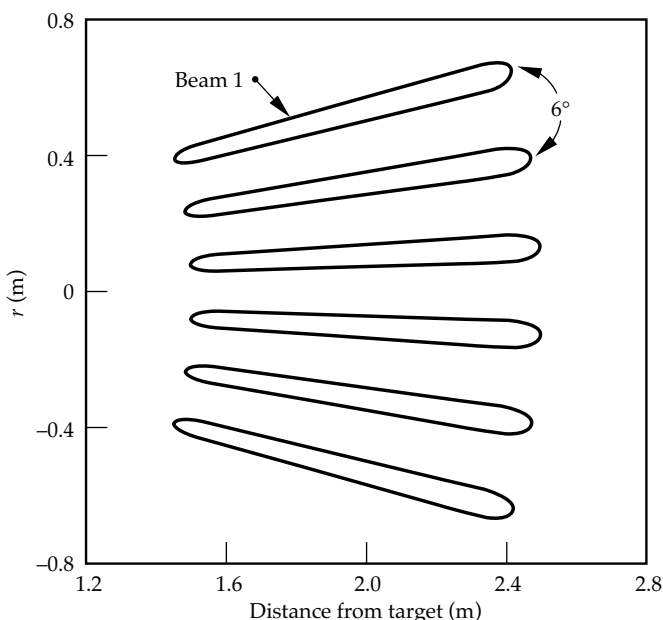


FIGURE 6. One option for multiple beam transport in the HYLIFE-II reactor is to place six beams in a “fan” aimed at one radiation converter. (50-00-0696-1366pb01)

If the fields due to the neighboring beams were constant along the beam length, we could compensate for them by increasing the focusing angle slightly. The fields are not constant, however, and vary along the pulse because of variations in the beam current as a function of z and the finite length of the beams. These two effects cause the field at the ends of the beam to be smaller than the field at the beam center. Since we cannot adjust the focusing angle on the time scale of the beam pulse duration (10 ns for the main pulse), the beam ends will be overfocused if the beam center is focused.

Hofmann, Hasse, and Reiser studied this problem for a cone of beams produced by an RF Linac with storage rings.¹⁹ In the RF Linac approach to HIF, beam compression is done by a phase rotation and results in a beam with a roughly Gaussian current profile. The variation in current along with the finite length of the beams causes a large variation in the electric field between the beam center and the beam ends. Hofmann et al. found that the increase in spot size due to the neighboring beams was tolerable for a charge state +1 beam, but scaled as the charge state squared, so that it was not acceptable for higher-charge-state ions.

This problem is less severe for beams produced by an induction linac. With careful longitudinal beam control, the induction linac can produce a nearly flat topped current pulse so that variations in the electric field come almost exclusively from the finite length of the beams. Calculations show $\leq 5\%$ beam loss for a “fan” of either six unneutralized, 4-kA beams of 10-GeV Pb^+ ions or six 70% neutralized, 7.5-kA beams of 5.3-GeV Cs^+ ions.²⁰

Complete simulations of the neighboring beams problem will require a fully three-dimensional, electromagnetic code. Such a code is under development by J.-L. Vay and C. Deutsch at University of Paris-Orsay.²¹

Summary

Transporting the heavy-ion beam through the reactor chamber to the target is a critical step in a HIF power plant. We have simulated low-density, nearly ballistic transport in a chamber that is consistent with the HYLIFE-II reactor design. Our simulations show that even at the relatively low densities of HYLIFE-II, beam stripping plays an important role. We have found that we can overcome the effects of beam stripping by charge neutralizing the beam using a low-density plasma column in the chamber.

Charge-neutralized transport has also opened up new accelerator regimes by allowing lower-mass, lower-energy ions to be used. Using lower-energy ions should reduce the cost of the accelerator driver, which in turn reduces the cost of electricity. Using

lower energy ions requires a larger beam current to deliver the same amount of energy to the target; transporting this large current requires either a very large number of beams or charge-neutralized transport. Our simulations showed that ionizing less than 0.5% of the background gas in the HYLIFE-II chamber is sufficient to transport a 7.5-kA beam of Cs^+ ions.

Experiments are needed to verify the results of the simulations. We believe that experiments to study beam neutralization can be done using existing facilities at LBNL or Sabre at Sandia National Laboratories.

Beam neutralization thus far has concentrated on "passive" neutralization using plasmas in the chamber. "Active" neutralization by co-injecting an electron beam along with the ion beam is another possibility for beam neutralization. Further study in this area is needed.

Notes and References

1. W. M. Sharp, *ICF Quarterly Report* 4(2), 70–77, Lawrence Livermore National Laboratory, UCRL-LR-105820-94-2 (1994).
2. A. Friedman et al., *ICF Quarterly Report* 5(3), 179–186, Lawrence Livermore National Laboratory, UCRL-LR-105821-95-3 (1995).
3. V. O. Brady, A. Faltens, D. Keefe, E. P. Lee, J. Hovingh, *Heavy Ion Fusion System Assessment: Final Focus and Transport Model*, LBL-23040, July 1987.
4. R. W. Moir et al., *Fusion Technology* 25, 5 (1994).
5. W. A. Barletta, W. M. Fawley, D. L. Judd, J. W.-K. Mark, and S. S. Yu, "Heavy-Ion Inertial Fusion, Interface between Target Gain, Accelerator Phase Space, and Reactor Transport Revisited," *Proc. of International Symposium of Heavy Ion Accelerators*, Tokyo, Japan, January 23–27, 1984 (UCRL-90246).
6. E. P. Lee, *Heavy Ion Inertial Fusion*, M. Reiser, T. Godlove, and R. Bangerter, Eds., *AIP Conference Proceedings*, American Institute of Physics, New York, NY, p. 461 (1986).
7. R. W. Petzoldt, Ph. D. Thesis, University of California at Davis, 1995.
8. D. D.-M. Ho, I. Haber, K. R. Crandall, S. T. Brandon, *Particle Accelerators* 36, 141 (1991).
9. N. Barboza, U.C. Berkeley, private communication (1994).
10. W. R. Meier et al., *Osiris and Sombro Inertial Confinement Fusion Power Plant Designs*, WJSA-92-01, DOE/ER/54100-1 (1992).
11. B. Badger et al., *HIBALL-2, An Improved Conceptual Heavy Ion Beam Driven Fusion Reactor Study*, UWFD-625, U. of Wisconsin (1984).
12. C. K. Birdsall and A. B. Langdon, *Plasma Physics via Computer Simulation*, McGraw-Hill, New York, 1985.
13. A. B. Langdon, *Computer Physics Communications* 70, 447 (1992).
14. A. B. Langdon, *Bull. Am. Phys. Soc.* 35, 2415 (1991).
15. D. A. Callahan and A. B. Langdon, *Proc. of the 1995 Particle Accelerator Conference*, pp. 3238–3240, Dallas, TX, May 1–5, 1995.
16. N. Barboza, submitted to *Fusion Engineering and Design*.
17. G. R. Magelssen and D. W. Forslund, *Heavy Ion Inertial Fusion, AIP Conference Proceedings*, p. 330, M. Reiser, T. Godlove, and R. Bangerter, Eds., American Institute of Physics, New York, NY (1986).
18. D. S. Lemons, M. E. Jones, *Heavy Ion Inertial Fusion*, M. Reiser, T. Godlove, and R. Bangerter, Eds., *AIP Conference Proceedings*, American Institute of Physics, New York, NY, p. 287 (1986).
19. I. Hofmann, R. W. Hasse, and M. Reiser, *J. Appl. Phys.* 73, 7061 (1993).
20. D. A. Callahan, *Appl. Phys. Lett.* 67, 27 (1995).
21. J.-L. Vay, accepted for publication in *Fusion Engineering and Design*.

EFFICIENT PRODUCTION AND APPLICATIONS OF 2- TO 10-keV X RAYS BY LASER-HEATED “UNDERDENSE RADIATORS”

L. J. Suter

M. S. Maxon

R. L. Kauffman

J. F. Davis*

Introduction

Within the next decade, very-high-power, high-energy laser facilities may be constructed in Europe^{1,2} and the United States.³ Two-dimensional (2-D) numerical simulations with the LASNEX code⁴ at Lawrence Livermore National Laboratory (LLNL) indicate that this next generation of lasers offers the prospect of producing multi-keV x rays with unprecedented efficiency: as much as 14% above 10 keV, 30% above 4 keV. Such efficiencies, coupled with the intrinsically high energy of these facilities, should allow us to produce great quantities of multi-keV x rays—as much as several hundred kilojoules. This, in turn, may allow us to perform experiments and field diagnostics we could never consider with current facilities. Applications of high-energy, multi-keV sources with the proposed National Ignition Facility (NIF) include volume pre-heating of experimental targets; bright, multi-keV backlighting; pumps for fluorescent imaging of capsule dopants and Doppler velocimetry; and uniform irradiation of large test objects for Nuclear Weapons Effects Testing (NWET).

Projections of Efficiency

Conventional slab targets irradiated by current lasers produce multi-keV x rays with relatively low efficiency. At photon energies >3 keV, the typical efficiency for converting laser light into multi-keV x rays is less than 1%.⁵ Multi-keV efficiencies well in excess of those commonly obtained today are predicted to be achieved with “underdense radiators,” a nontraditional source of laser-generated x rays (so called because the density of these targets is less than critical density of the laser light). Figure 1 shows two examples of such sources. Figure 1(a) is a column of gas (or foam) irradiated from one end by a single $0.35\text{-}\mu\text{m}$ (blue) laser beam. In simulations using 0.01 g/cm^3 of Xe gas irradiated by a 2-ns flattop pulse at an intensity of 10^{15} W/cm^2 , we find

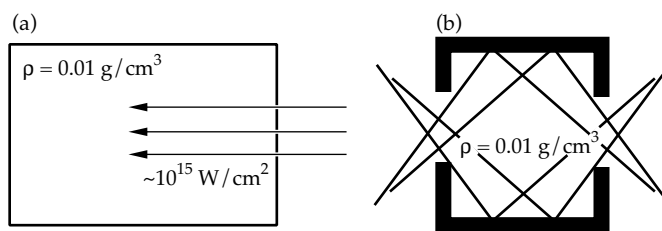


FIGURE 1. Two types of “underdense radiators.” (a) is a gas (or foam) column irradiated from one end with a single, large-f-number beam. (b) is a transparent container, filled with underdense gas or foam, irradiated with several beams. NIF target type (a) can be irradiated with, at most, 10 TW. Target type (b) can accept several beams, so it can be irradiated with higher total power. (20-03-0696-1296pb01)

efficiencies into photons of energy >4 keV (L-shell Xe and continuum) to be 19% with a 10-TW beam. Since a cluster of four “beamlets” of the proposed National Ignition Facility (NIF)³ will deliver 10 TW in the geometry of Fig. 1(a), good efficiency may be achievable with such gas-column sources. However, simulations indicate that higher efficiencies and higher photon energies with such a target will require more than 10 TW. This would be incompatible with the 10-TW/beam maximum of the NIF. Figure 1(b) shows a higher power source compatible with the NIF. It is a low-Z container, transparent to x rays of interest, filled with an appropriate-Z, low-density gas or foam. Since it is heated by more than one beam, it can be irradiated at much more than 10 TW. In simulations where the can is filled with Xe gas at 0.01 g/cm^3 , we find near-optimal performance for containers 2 mm diameter and 1.6 mm long with 1-mm-diam laser entrance holes. For 2-ns pulses, simulated, >4 -keV efficiencies range from 17% at 20 TW to 30% at 60 TW.

We have efficient 2-D designs of target type (b) at photon energies up to ~ 10 keV. Table 1 summarizes our LASNEX study. In all cases, the densities are 0.01 g/cm^3 , and the rest of the laser energy appears as either thermal emission (<1 to 2 keV) or plasma energy.

*Alme Associates, Alexandria, VA.

Figure 2 plots the highest source efficiencies in the third column of Table 1 vs photon energy and compares them with current disc backlighter efficiencies.⁵ The figure forcefully illustrates how much more efficient underdense radiators, heated by powerful lasers, can be compared to current backlighters.

TABLE 1. Summary of LASNEX study results.

Material	Power (TW)	Fraction of laser energy $> h\nu$ (keV)
Kr	60	4% > 13 ; 30% > 2
Ge	60	14% > 10 ; 26% > 2
Ge	50	10% > 10 ; 26% > 2
Ge	30	7% > 10 ; 20% > 2
Cu	40	11% > 8.5 ; 26% > 2
Cu	30	10% > 8.5 ; 24% > 2
Dy	60	9% > 8 ; 24% > 2
Xe	60	30% > 4 ; 48% > 1
Xe	50	26% > 4 ; 48% > 1
Xe	30	22% > 4 ; 40% > 1
Xe	20	17% > 4 ; 37% > 1

Physics of Efficient Production

Analysis of LASNEX simulations leads to a simple understanding of such high efficiencies in the multi-kilovolt regime and tells us why these are qualitatively different from standard discs. In the following discussion, we use Xe as an example, although the arguments are valid for other materials as well.

Good Multi-KeV Efficiency Is Intrinsically Possible

First, we show how high, multi-keV efficiency is possible with an underdense radiator. Figure 3 illustrates

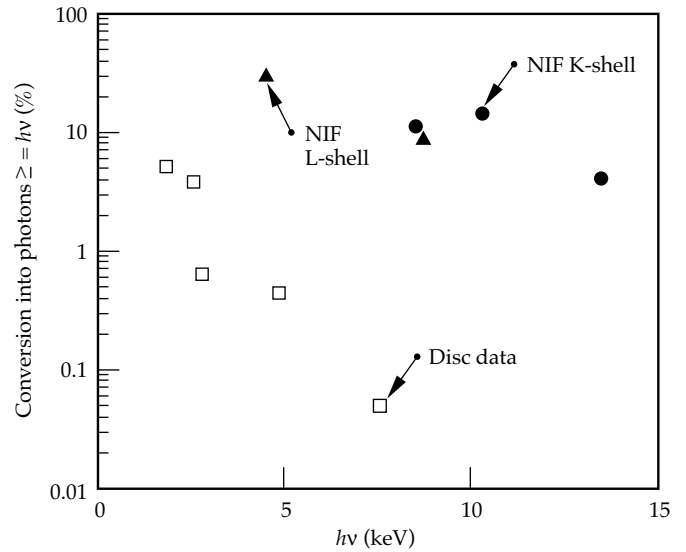


FIGURE 2. The projected multi-keV efficiencies for sources like those of Fig. 1(b) are much higher than current disc efficiencies. K-shell refers to the Ge, Cu, and Kr sources of Table 1. L-shell refers to the Dy and Xe sources. (20-03-0696-1301pb01)

the first component of high, multi-keV efficiency. It shows theoretical estimates of Xe emission at electron temperatures of 2 keV and at 5 keV. The Xe density is 0.01 g/cm³. This plot makes a widely known but essential point: x-ray emission shifts to higher energy as plasma is made hotter. Figure 4, which plots radiation production/cm³ vs electron temperature, contains the next step in the argument. This is from an optically thin LASNEX simulation. The black line is total emission vs T_e . The gray line is the emission > 4 keV (see Fig. 3). This plot shows that the overall radiation production does not change greatly with plasma temperature. However, at higher temperatures almost all the emission will be multi-keV (see Fig. 3). Figure 4 illustrates an important point: a material that efficiently produces x rays in the softer, “thermal” region may also efficiently

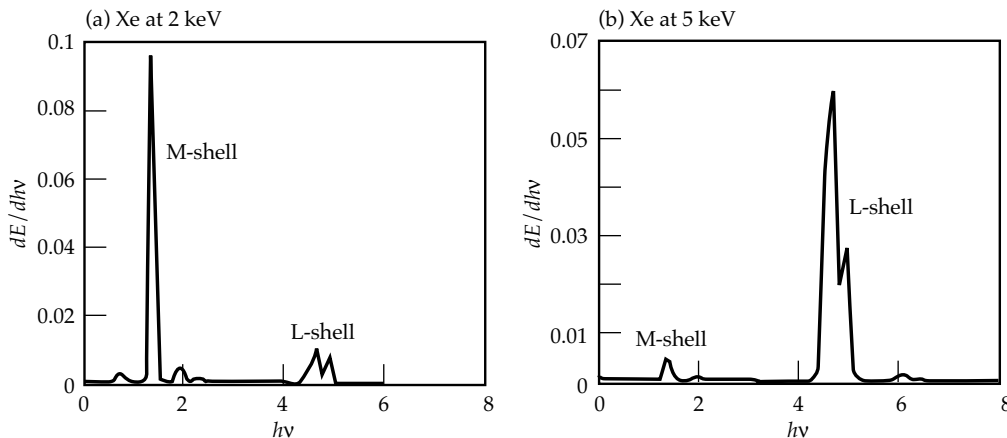


FIGURE 3. Emission from 0.01 g/cm³ Xe at electron temperatures of (a) 2 keV and (b) 5 keV, simulated by XSN. Heating a material causes more of its total emission to be produced at higher photon energies. (20-03-0696-1302pb01)

produce x rays in a much more energetic region if it is made hotter.

Figure 5 is the plot needed to reach a simple, quantitative understanding of efficient multi-keV production. It shows Xe L-shell radiation production vs electron density for material at electron temperatures of 3, 4 and 5 keV. The Xe volume is that of a 1.4-mm-radius standard “gasbag”⁶ similar to ones we have shot on Nova for studies of laser-plasma instabilities.⁷ Figure 5 shows that at densities ~ 1 to 1.5×10^{21} /cm³, a 4- to 5-keV Xe-filled gasbag would produce ~ 5 to 12 TW of L-shell emission. Thus, if we can heat such a gasbag to these temperatures with a 30-TW, 1-ns Nova pulse (30 kJ energy), and if it remains together for ~ 1 ns, we might expect to produce ~ 5 to 10 kJ of L-shell emission, or 16 to 33% multi-keV efficiency.

That we can both heat the bag and that it does not disassemble too quickly follow from simple arguments. If all the material in the gasbag is at constant temperature, then its thermal energy in kJ is approximately $2.75T_e$ (in keV) $\times n_e$ (in units of 10^{21} /cm³). For the temperature and density regimes of interest (4 to 5 keV, 1 to 1.5×10^{21}), this corresponds to 10 to 20 kJ. Moreover, the sound speed of Xe gas at 4 keV is $\sim 6 \times 10^7$ cm/s, so the rarefaction takes more than 1 ns to propagate to the center of the 1.4-mm-radius bag.

The Xe emission calculations just discussed were made with a non-local-thermodynamic-equilibrium average-atom model known as XSN.⁸ Better theoretical estimates using a detailed configuration approximation model⁹ give essentially the same result. Our estimates above also assume the radiation can get out. Detailed simulations with radiation transport of the lines indicate that the radiation can escape.

Hydrodynamics for Good Efficiency

Above we reasoned that efficient multi-keV radiation production is possible. It also indicates that the achievement of good multi-keV efficiency requires a hydrodynamic system that converts most of the laser energy into hot plasma at sufficient density that it can radiate a considerable fraction of the energy before it disassembles. Underdense plasmas can provide such a hydrodynamic system. Moreover, they do this better than discs, which is the main reason underdense plasmas can be considerably more efficient multi-keV sources than discs (see Fig. 2).

We can see the hydrodynamic differences by analyzing three simulated Xe gas-column sources of different densities (0.01, 0.02 and 0.1 g/cm³) but irradiated by the same laser. Figure 6 shows the total L-shell radiation escaping 1-D simulations of these gas columns vs time. (1-D analogs of the 2-D gas column of Fig. 1[a]). The 1-D efficiency is higher than 2-D efficiency

because there is no radial hydrodynamic disassembly.) The gas column that started at 0.01 g/cm³ ($\sim 0.2n_c$ when fully ionized) has the highest efficiency. At the

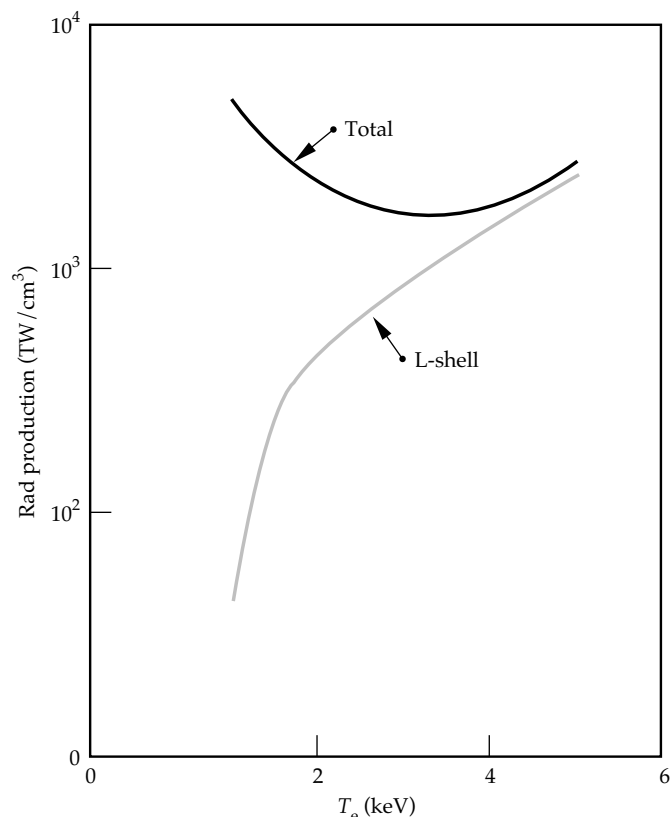


FIGURE 4. Total emission per cm³ vs electron temperature and L-shell emission (Xe at 0.01 g/cm³). A material that is an efficient source of thermal x rays can also be a good source of multi-keV x rays, if we can make it hot enough. (20-03-0696-1303pb01)

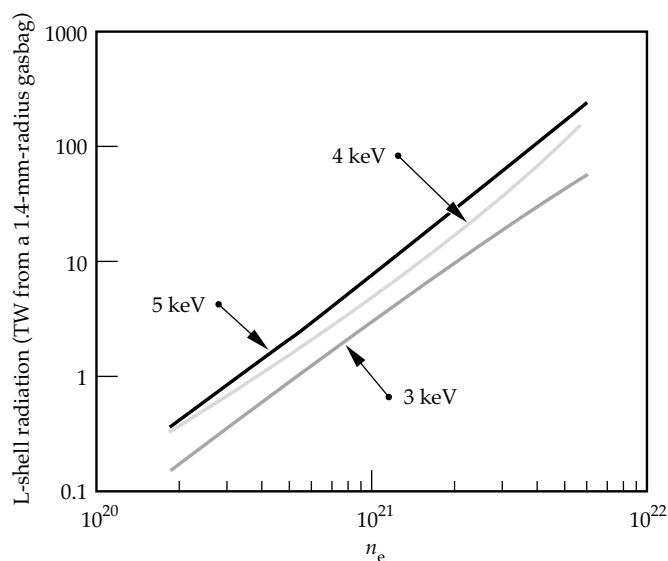


FIGURE 5. L-shell emission from the volume of a 1.4-mm-radius, Xe-filled gasbag, vs electron density. (20-03-0696-1304pb01)

end of the 2-ns pulse, more than half of the incident 48-TW laser power is escaping this column as L-shell emission. The column that started at 0.02 g/cm^3 behaves like the lower density one for $\sim 1 \text{ ns}$, but then its efficiency drops notably. The 0.1-g/cm^3 gas column has comparatively low efficiency the whole time. We call it disc-like since its simulated L-shell radiation production is the same as a frozen Xe slab's (not shown).

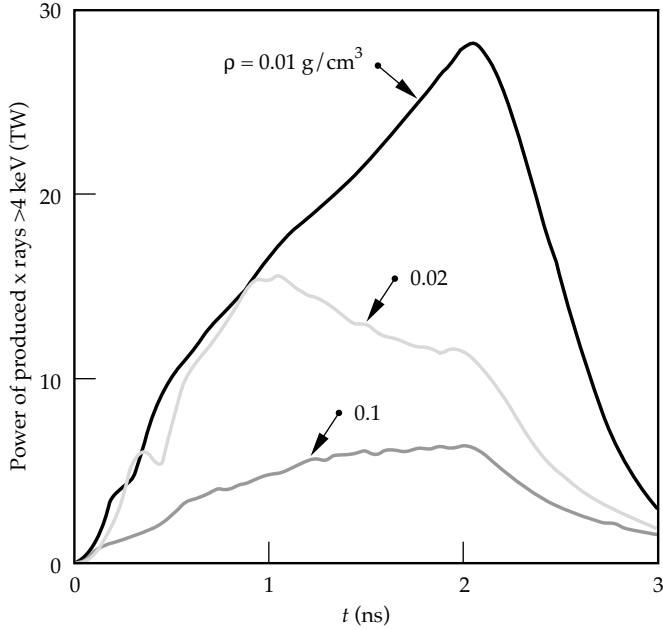


FIGURE 6. Time dependence of L-shell emission escaping 1-D LASNEX simulations of Xe gas columns of different densities. The three columns were all irradiated with 48 TW of blue laser light. (20-03-0696-1305pb01)

Now we can pass on to the next level of understanding. Figure 7 plots electron density and temperature, at 1 ns, vs length along the gas columns. The three 1-D gas columns clearly have very different hydrodynamics. In Fig. 7(a), in the 0.01-g/cm^3 gas column, the heating front moves nearly supersonically (also known as a bleaching front). However, in the poorest-efficiency, 0.1-g/cm^3 gas column, Fig. 7(b), the heating front moves subsonically (also known as an ablative front). Unlike the bleaching front, the ablative front drives a shock of dense material ahead of itself. The 0.02-g/cm^3 gas column is a transitional case; early in time it was heating in an approximately supersonic manner. However, residual hydrodynamics caused a density bump ahead of the front to accumulate, finally causing a transition, at $\sim 1 \text{ ns}$, to completely ablative heating. The transition from bleaching to ablative coincides with the efficiency drops at 1 ns seen in Fig. 6.

Further analysis shows that a bleaching front creates far hotter plasma than an ablative front, hotter plasma that is denser and therefore more efficient in producing multi-keV x rays. In particular, we find the following:

- In producing a given mass of hot plasma, more energy is lost to low-photon-energy radiation when the heating occurs in a dense ablation front than when the matter is heated in the uncompressed bleaching front. The ablative front's dense material, which is being heated by conduction from the laser-deposition region, has a very high radiation production rate. However, since it is relatively cold, the emission is not multi-keV. This emission is energy lost from the system that cannot contribute to heating plasma and, since it is low-photon energy, does not contribute to multi-keV production. From the viewpoint of multi-keV radiation production, it is a parasitic loss.

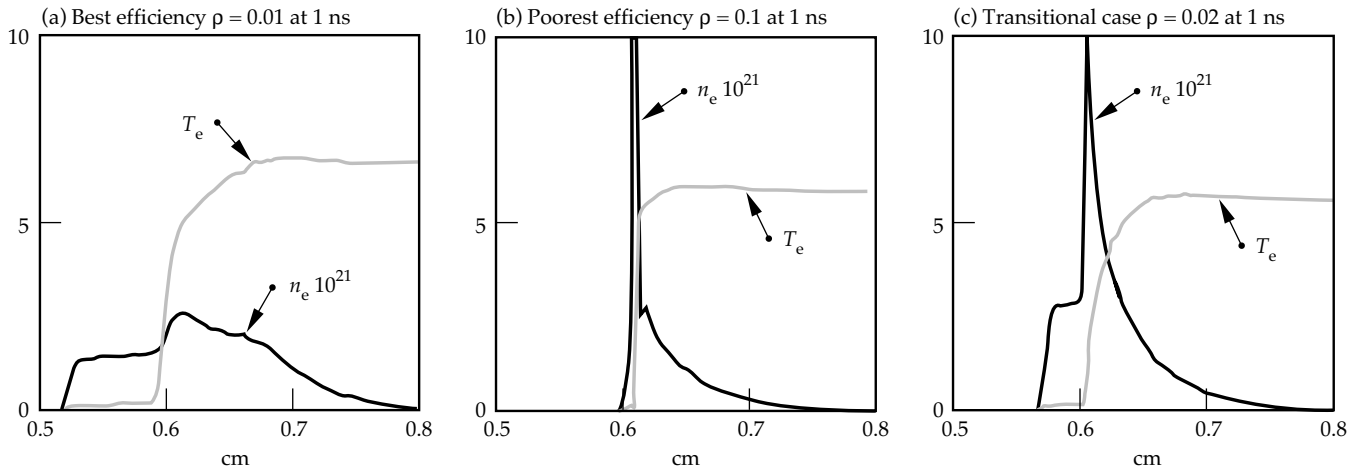


FIGURE 7. Electron temperature (keV) and electron density ($\times 10^{21}$) at 1 ns vs axial position (cm) for the three 1-D gas-column sources in Fig. 6. (20-03-0696-1306pb01)

- Because of the higher density, the material in the ablation front rises to higher pressure. This ends up as more kinetic energy per unit of mass heated.
- More kinetic energy causes the hot blowoff behind an ablative heating front to be less dense than behind a bleaching front; compare electron density profiles of Fig. 7(a) and 7(b). Consequently, the blowoff behind the bleaching front produces more coronal, multi-keV x rays per unit mass because such emission scales approximately as $(n_e)^2$ (see Fig. 5).

Experimental Validation of Modeling

Calculations similar to those above provided the first indication that we might be able to very efficiently produce multi-keV x rays with laser-heated underdense sources.¹⁰ Following these initial findings, we performed theoretical and experimental work to examine the validity of these predictions. This involved testing our ability to properly estimate the multi-keV efficiencies of published slab data,^{11–13} as well as efficiencies from Xe-filled gasbags⁶ specifically shot at Nova to test these predictions.¹⁴ Figure 8 compares simulated and experimental absolute multi-keV efficiencies for all these experiments. Except for two low-intensity (1.4×10^{14} W/cm²) slab targets, there is general agreement between the experiment and simulations. In particular, the >4 keV, L-shell production from our Xe gasbag experiments¹⁴ agrees satisfactorily with the 2-D LASNEX estimates. They are actually slightly higher than the simulations. This favorable comparison seems to lend credibility to the predictions discussed above.

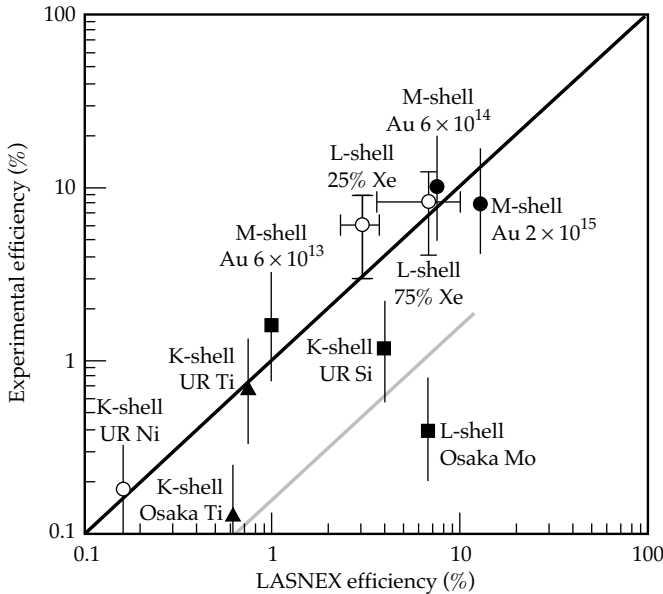


FIGURE 8. Comparison of simulated and experimental multi-keV conversion efficiencies from several databases. (20-03-0696-1307pb01)

In addition to this comparison with experiment, there is a fairly extensive and documented database indicating that LASNEX reasonably models the electron temperature in gasbags and gas-filled hohlraums.¹⁵ The capacity to properly estimate underdense plasma electron temperatures is an essential component of believable, multi-keV predictions.

Applications of Efficient Multi-KeV X-Ray Sources

Below we discuss four applications of high-energy, multi-keV sources with the NIF:

1. Volume preheating of experimental targets.
2. Bright, multi-keV backlighting.
3. Pumping for fluorescent imaging of capsule dopants and doppler velocimetry.
4. Uniform irradiation of large test objects for NWET.

Preheat Sources

Multi-keV x rays can be used to preheat experimental packages. The preheat temperature T_e produced in a package located distance d away from a multi-keV source can be found by balancing x-ray deposition with internal energy. Neglecting ionization energy, this balance is approximately

$$\frac{\eta_x E_L}{4\pi d^2 \ell} = \left(\frac{3}{2}\right) \frac{\rho(Z+1)T_e}{A} (9 \times 10^4) \quad (1)$$

Here η_x is the multi-keV efficiency; E_L is the laser power; ℓ is the scale length over which x-ray absorption occurs in the experimental package; ρ , Z , and A are the density, atomic number, and weight of the experiment we are preheating. Using $\eta_x = 30\%$, $E_L = 10^6$ J, $d = 0.5$ cm, $\rho = 1$ g/cm³, and $(Z+1)/A = 0.33$ gives $T_e = 2$ eV-cm/ ℓ . Depending on ℓ , it may be possible to preheat large $\rho = 1$ samples to ~5 eV and thinner ones up to several tens of eV, possibly approaching 100 eV. NIF applications for preheat sources like this include off-Hugoniot equation-of-state measurements and low-temperature hydrodynamics.

Backlighter Sources

Sources like these could serve as the bright, high-photon-energy, large-area backlighters needed for bigger targets. Consider, for example, the 60-TW Ge source listed in Table 1 scaled up to 100 TW (14% > 10 keV). Viewed from the end of the 2-mm-diam cylinder, the >10-keV emission/cm²/sr will be 3.5×10^{13} W/cm²/sr. This is equivalent to viewing a 10-keV hemi-isotropic

disc source of 1% efficiency irradiated by 700 TW at an intensity of $\sim 2.2 \times 10^{16}$ W/cm².

Pumps for Fluorescence-Based Diagnosis

Efficient multi-keV sources and high-power lasers may allow us to field fluorescence-based diagnostics—a qualitatively new way of studying hydrodynamics. The principle is simple: a multi-keV source at distance d pumps a dopant in a capsule. In imaging, the number of photons collected from a resolution element r is given by

$$\# \text{ of photons} = \frac{\eta_x P_L}{4\pi d^2} r^2 \left(\frac{r}{\ell} \right) \frac{\eta_F \delta\Omega \eta_{\text{det}} \delta\tau}{E_x} \quad (2)$$

Here, P_L is the laser power; E_x , the source's average photon energy; η_F , the dopant's fluorescent efficiency; and $\delta\Omega$, η_{det} and $\delta\tau$, the camera's solid angle, efficiency, and time resolution. Using $r = 10 \mu\text{m}$, $P_L = 60$ TW, $\eta_x = 10\%$, $E_x = 10$ keV, $d = 0.5$ cm, $\delta\tau = 100$ ps, and $\eta_F = 0.2$ (i.e., Cu-K at 8 keV has $\eta_F = 0.2$ in Ref. 16) gives

$$\# \text{ of photons} = (3.2 \times 10^9) \left(\frac{10 \mu\text{m}}{\ell} \right) \delta\Omega \eta_{\text{det}} \quad (3)$$

For a 10- μm pinhole at 1 cm and the dopant concentration arranged so that $10 \mu\text{m}/\ell \approx 0.01$ to 0.1, we collect 40 to 400 photons from each 10- μm resolution element. For a curved crystal/Rowland circle system, the number of photons could be ~ 300 to 3000, at 1% crystal reflectivity.

A compelling possibility is using doppler spectroscopy of fluorescent lines to measure pusher velocity and, possibly, show the evolution of turbulence (via line broadening) at stagnation. Figure 9 indicates how the fluorescent lines may be shifted when the pusher starts to

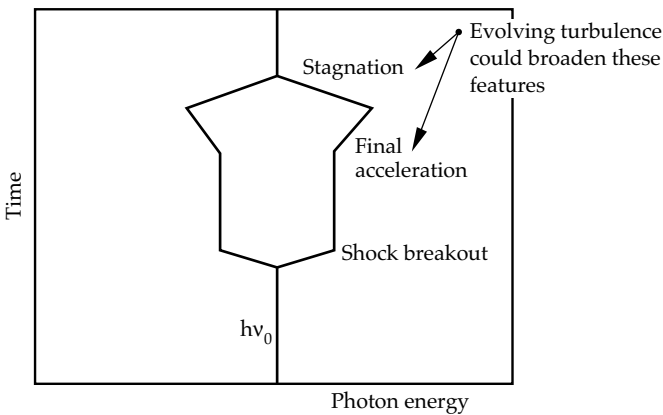


FIGURE 9. Doppler spectroscopy of fluorescing dopants in a capsule could measure pusher velocity and, possibly, show the evolution of turbulence, via line broadening, at stagnation. Efficient multi-keV sources could pump such fluorescence. (20-03-0696-1308pb01)

move, during final acceleration, and during stagnation. A requirement for this will be an efficient spectrometer which sees only diametrically opposed parts of a doped capsule. Related to this, fluorescence might produce cut-away pictures of capsule mix, perhaps similar to those used to visualize mixing in 3-D simulations. At a velocity of 10^7 cm/s or more, narrowband Doppler imaging with a camera of spectral resolving power 1500 or greater^{17,18} could image only one side of the imploding pusher.

Large Fluence-Area Products with Good Uniformity

A requirement for NWET is that the flux over a test object be uniform to $\pm 10\%$. This allows us to describe an NWET simulator by the fluence \times area product that it can produce with that uniformity. In general, the fluence \times area product in a given spectral region will be

$$\text{fluence} \times \text{area} = \left(\frac{E_L \eta}{4\pi} \right) T_{\text{debris-shield}} (\delta\Omega_{10\%}) \quad (4)$$

The first term ($E_L \eta / 4\pi$) is the source output per steradian in the spectral range of interest. It is determined by multi-keV source efficiency and total laser energy. $T_{\text{debris-shield}}$ is the debris shield transmission. It will be \sim unity at 5 keV and higher, but may be significantly <1 at lower energies. The last term $\delta\Omega_{10\%}$ is the solid angle we can collect from each source and still get $\pm 10\%$ uniformity. It is a strong function of geometry. If all the emission is concentrated at a single point, as in typical pulse-power NWET simulators, we can collect only 0.45 sr with $\pm 10\%$ uniformity. However, if we produce x rays in a number of properly distributed sources, the useful solid angle increases. With four distributed sources, we can collect up to 1.6 sr from each source, and with 25 distributed sources, 4.5 sr. Thus, with proper facility capabilities, it is possible for 1 J of laser-produced multi-keV energy to be worth up to 10 J produced by a more conventional NWET simulation source. However, this improvement comes at a facilitization price. The sources need to be distributed over an area comparable to the size of the test object. For objects ~ 1 m across, this requires steering beams to irradiate sources much as 50 cm from chamber center.

On the NIF, the estimated fluence \times area products with four distributed sources and 100% debris-shield transmission are as follows: 1 to 5 keV, 50,000 J-cm²; 5 to 15 keV, 14,000 J-cm². With 25 distributed sources: 1 to 5 keV, 140,000 J-cm²; 5 to 15 keV, 40,000 J-cm². This prospect for simulation capacity has led to the formation of a joint U.S. Department of Defense–Department of Energy working group (NIF Radiation Sources Users Group¹⁹) that works with the NIF Project aiming to optimize the NIF's NWET capabilities.

Acknowledgments

This work was supported by the Defense Nuclear Agency (Department of Defense) and the U.S. Department of Energy. We would like to acknowledge very useful discussions with Mike Tobin and Greg Simonsen of LLNL, C. P. Knowles of JAYCOR, and William Summa and Ralph Schneider of DNA.

Notes and References

1. M. Andr , M. Novaro, and D. Schirmann, "Technologie pour un Laser Megajoule," *Revue Scientifique et technique de la Direction des applications militaires*, Chocs, Num ro 13, 73, April 1995.
2. J. MacMordie, private communication (AWE, Aldermaston, UK, 1995).
3. J. T. Hunt et al., *A Design Basis for the National Ignition Facility*, Lawrence Livermore National Laboratory, Livermore, CA, UCRL-JC-117399 (1994).
4. G. B. Zimmerman and W. L. Kruer, *Comments Plasma Phys. Controlled Fusion* **2**, 51 (1975).
5. R. L. Kauffman, *Handbook of Plasma Physics, Vol. 3: Physics of Laser Plasma*, p. 123, Eds. M. N. Rosenbluth and R. Z. Sagdeev, Elsevier Science Publishers B. V. (1991).
6. R. L. Kirkwood et al., "Effect of Ion Wave Damping on Stimulated Raman Scattering in High Z Laser Produced Plasmas," *Phys. Rev. Lett.*, accepted for publication.
7. B. J. MacGowan et al., *Phys Plasmas* **3**, 2029 (1996).
8. D. E. Post, R. V. Jensen, C. B. Tarter, W. H. Grasberger, and W. A. Lokke, *At. Data and Nuclear Data Tables* **20**, 397 (1977); G. B. Zimmerman and R. M. More, *J. Quant. Spectros. Radiat. Transfer* **23**, 517 (1980).
9. P. L. Hagelstein, *Physics of Short Wavelength Laser Design*, Lawrence Livermore National Laboratory, Livermore, CA, UCRL-53100 (1981).
10. L. J. Suter et al., "NIF will be a very useful DNA simulation facility just using laser produced x rays," *Proceedings of the NWET Applications for NIF Workshop*, G. Simonsen, Ed., Lawrence Livermore National Laboratory, Livermore, CA, March 15-17, 1994.
11. Kondo et al., *J. Appl. Phys.* **67**, 2693, (1990).
12. Yaakobi et al., *Opt. Commun.* **38**, 196 (1981).
13. R. L. Kauffman et al., *Laser Program Annual Report, 1986*, Lawrence Livermore National Laboratory, Livermore, CA, UCRL-50021-86 (1986).
14. R. L. Kauffman et al., *ICF Quarterly Report* **6**(2), Lawrence Livermore National Laboratory, Livermore, CA, UCRL-50021-96 (to be published fourth quarter, 1996).
15. L. V. Powers et al., *Phys. Plasmas* **2**, 2473 (1995).
16. S. T. Perkins et al., *Tables and Graphs of Atomic Subshell and Relaxation Data Derived from the LLNL Evaluated Atomic Data Library (EADL), z=1-100*, UCRL-50400 Vol. 30, Lawrence Livermore National Laboratory, Livermore, CA, October 31, 1991.
17. F. J. Marshall and J. Ortel, "A Framed Monochromatic X-Ray Microscope for ICF," *11th Topical Conference High Temperature Plasma Diagnostics*, Monterey, CA, May 12-16, CONF-960543-Absts., E-1, submitted to RSI.
18. S. A. Pikuz et al., "High-Luminosity Monochromatic X-Ray Backlighting Using Incoherent Plasma Source to Study Extremely Dense Plasma," *11th Topical Conference High Temperature Plasma Diagnostics*, Monterey, CA, May 12-16, CONF-960543-Absts., E-2, submitted to RSI.
19. Wendland Beezhold (SNLA), George Ulrich (DNA), and Greg Simonsen (LLNL), private communication (December, 1994).

LASER-TISSUE INTERACTION MODELING WITH THE LATIS COMPUTER PROGRAM

R. A. London M. E. Glinsky

D. S. Bailey G. B. Zimmerman

D. C. Eder

Introduction

The development of new instruments and procedures for use in laser medicine typically involves extensive experimental and clinical studies. Computational modeling of the laser-tissue interaction process can be used to explore and reduce the experimental parameter space (e.g., laser wavelength, pulse length and pulse energy), and to gain a deeper understanding of specific laser-medical processes. In this way, modeling can lead to more rapid development of new instruments and protocols and to the genesis of new ideas. In addition, modeling will be useful in the future for patient-specific treatment planning and for physician training. Modeling will only be useful, however, if it is closely linked to experiments; a project to develop a specific instrument or protocol must involve iteration between modeling and experiment, converging on a set of optimized design parameters. Figure 1 shows a likely iterative process using LATIS, a

computer program we have recently developed at the Lawrence Livermore National Laboratory to treat a wide range of laser-tissue interaction phenomena.

The therapeutic uses of lasers fall into three broad classes, depending on the physical mechanism by which the laser interacts with and alters the living tissue: photothermal, photochemical, and photomechanical. The physical processes involved in these three laser-tissue interactions include laser light propagation, thermal heat transport, thermal coagulation, and other material changes; photochemistry; and hydrodynamic motion, respectively. An excellent introduction to many aspects of these processes can be found in a recently published textbook in which chapters have been written by several of the experts in this field.¹ In this article, we present the structure and contents of the LATIS program. We also present a brief discussion of several applications, and a detailed discussion of one application: the problem of laser-light dosimetry with dynamic optical properties.

The LATIS Program

LATIS is a two-dimensional, time-dependent simulation program. It is based on the experience gained during 25 years of modeling high-intensity laser-matter interactions for fusion research, particularly with the LASNEX code.² LATIS uses cylindrical geometry, with spatial positions described by radial and axial coordinates, r and z . The spatial domain of a calculation is defined by a connected mesh of line segments containing quadrilateral zones. Each line segment intersection is called a mesh point. Positions and velocities are defined at the mesh points, while most material properties, such as temperature and density, are defined at the zone centers. Physical properties are modeled mathematically by analytic formulas, table interpolations, and both ordinary and partial differential equations. Partial differential equations are solved by finite-difference or finite-element methods. In addition, the Monte Carlo method is also used for laser transport, as described below. LATIS is written in

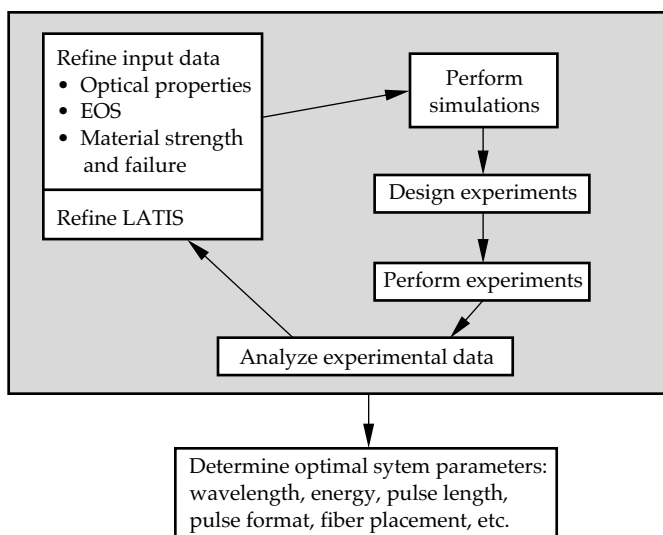


FIGURE 1. LATIS is used in an iterative method along with experiments to design a laser-medicine system. The cycle eventually converges on optimized experiment design parameters. (50-03-0796-1584pb01)

FORTRAN and controlled by a computer-science back-plane called Basis.³ Basis is an interpreter that allows the user considerable flexibility in setting up problems, adding user-defined functions without recompiling the code, and mathematical and graphical post-processing.

The physical processes considered by LATIS are grouped into four categories, as illustrated in Fig. 2: laser propagation, thermal response, material response, and hydro response. For most applications, laser propagation is calculated in the radiation-transfer approximation, although for certain situations, such as ultrashort laser pulses, a wave treatment is needed. Reference 1 describes the radiation transfer approximation in the context of laser-tissue interaction and the associated calculational methods.

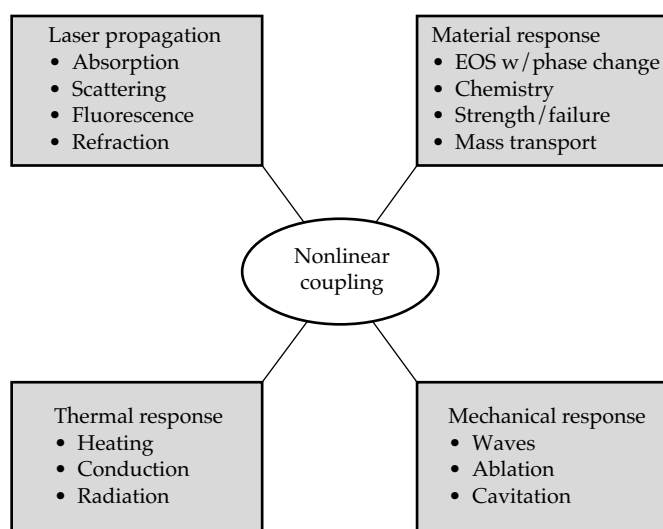


FIGURE 2. LATIS models laser-tissue interactions considering four areas of coupled physical processes. Features such as the hydro response are being developed for future use in tissue ablation applications. (50-03-0796-1585pb01)

Laser Propagation

To model the laser propagation portion of a simulation, we mainly use the time-dependent Monte Carlo method, in which light is represented by a finite number of "super photons"—typically 10^3 to 10^4 . Since a typical problem involves on the order of 1 J of laser energy, each super photon represents on the order of 10^{15} real photons. (Henceforth we refer to the super photons simply as photons.) The propagation of the photons is treated in a probabilistic manner. In LATIS, laser photons are created along one or several line segments of the numerical mesh with specified spatial energy distribution and angular distribution relative to the segment normal. A fixed number of photons is introduced at the first time step of the simulation. The photons are then tracked time-dependently through the spatial domain of the calculation. When they cross material interfaces with unequal indices of refraction,

such as an air-tissue interface, Fresnel reflection and refraction are calculated. Scattering is calculated probabilistically along a photon's path, according to the scattering coefficient, which may vary in space and time. An anisotropic angular phase function is used to select the scattering angle. We currently use the Henyey-Greenstein phase function, which has been found to be a good approximation to tissue scattering.^{4,5} Absorption is calculated analytically along each photon path according to the absorption coefficient, without destroying the photons. Each photon is assigned a weight, which decreases with absorption. When the weight drops below a specified value, typically 1%, the photon is retired from the Monte Carlo calculation. The energy absorbed along the photon path is tabulated in spatial zones, where it is added to the material internal energy. At the end of a time step, a certain number of photons are still "alive" within the spatial domain of the simulation, and a certain number have been removed, either by leaving the domain or by having dropped below the minimum weight. At the beginning of the next time step, new photons are injected if the laser source is still turned on. In order to keep the total number constant at the user-specified value, and to ensure the best statistics, an attempt is made to make the ratio of the number of source photons to the source energy for that particular time step equal to the ratio of the number of living photons to their total energy. If the number of photons that were removed during the time step is not enough to create the desired number of new photons to do this, we use a technique called "combing." Combing reduces the number of photons in zones having two or more photons in a statistical but energy-conserving manner.

In addition to the Monte Carlo method, we have the ability to invoke the diffusion approximation for laser transport, which is generally faster, but not as accurate near the surface of the material and for complicated geometries. For ultrashort pulses, we are adapting a wave equation solver to calculate the laser propagation and absorption.⁶ This is necessary because the absorption occurs via an evanescent wave extending into a high-density plasma, which cannot be described in the radiation transfer approximation.

Thermal Response

Absorption of the laser light primarily goes into raising the tissue temperature according to its specific heat. (For soft tissues this quantity is approximately that of water.) Heat is then carried away from the laser deposition region by thermal conduction and other processes. This is modeled with the well known "bio-heat" equation—essentially a diffusion equation with cooling and heating terms due to blood perfusion and boundary effects (see Refs. 7 and 8 for a basic discussion of the bio-heat equation). The effects of blood perfusion are

important for relatively long pulses (>1 s), which are used mainly for photothermal therapies. Heat exchanges between blood and tissue occurs most effectively in the smallest vessels (the arterioles, venules, and capillaries). In these vessels, the blood and tissue come to the same temperature very rapidly. (In larger vessels, there is little heat transfer between the blood and the tissue due to the rapid flow rate and lower surface-to-volume ratio.) Because the small vessels are generally short (≈ 1 mm or less) compared to other scales of interest, such as the laser spot size, the blood thermal effects are assumed to be local. By further assuming that the blood coming into the arterioles has a temperature equal to the body core temperature (37°C), we represent the blood-tissue exchange as local heating and cooling rates that are linear in temperature and that drive the tissue towards body temperature. In the models discussed below, we assume specific temperature and damage dependence to the blood perfusion, representing increases due to vessel dilation at slightly elevated temperatures and a decrease due to coagulation at long exposures to high temperature.

Material Response

The material response portion of the LATIS simulation includes calculation of the equation of state (EOS) that specifies the internal energy and pressure of a material as functions of the density and temperature. We usually use steady-state, equilibrium models; however, time-dependent models can be incorporated. It is important to accurately describe phase changes in the EOS, such as the liquid-vapor change in water. In the primary implementation, the EOSs are generated in the form of tables and placed in a simple library format for easy access by LATIS. The tables are produced by the Livermore EOS generator HQEOS,^{9,10} which is a global model including solid, liquid, vapor, and plasma states over a wide range of temperatures and densities. Models for chemical processes, such as protein denaturation and tissue coagulation, are included. We have also implemented an “Arrhenius” model, which describes such chemical processes by a single temperature-dependent rate equation.¹¹ Henceforth these processes are generically called damage. The rate equation is integrated to give a “damage integral”

$$\Omega = \int k dt, \quad (1a)$$

where the damage rate is

$$k = \frac{k_b T}{h} \exp\left[\frac{\Delta S}{R} - \frac{\Delta H}{RT}\right]. \quad (1b)$$

In these equations, k_b , h , and R are the Boltzmann, Planck, and gas constants, T is temperature, and ΔS

and ΔH are the entropy and enthalpy of the reaction. This formula applies formally only to ideal first-order reactions. Although in reality the damage processes in tissue are likely to be more complicated, we still use Eq. (1) as a convenient fitting formula to experimental data for such highly temperature-sensitive reactions. The undamaged fraction of the tissue $f_u = \exp(-\Omega)$, while the damaged fraction $f_d = 1 - f_u$. The damage integral is used to alter both the blood perfusion and the scattering coefficient. Other chemical processes, such as those responsible for tissue fusion in a welding procedure or photochemical processes during photodynamic therapy can be modeled in a similar manner. Another set of important material properties are the strength and failure characteristics under mechanical forces. We currently use simple prescriptions, such as a stress-strain relation, but more sophisticated time-dependent models are under development.

Hydrodynamic Response

The fourth category of physical process considered by LATIS is the hydrodynamic response of the tissue. These effects include acoustic waves, elastic and plastic deformations, and large motions such as cavitation and ablation. LATIS solves partial differential equations describing mass and momentum conservation using the Lagrangian method. In this method, the spatial zones represent small mass elements. The mesh points move in response to pressures generated in neighboring zones. The mass stays in each zone, moving with the mesh. The hydro equations are solved by a finite difference method and advanced in time via a second-order differencing scheme. The method is explicit, so that a maximum time step is set by a numerical stability criterion (the “Courant limit”). Other criteria, such as changes in the temperature and density, are also used to set a maximum time step to ensure an accurate and stable solution of the hydro equations.

Coupling

The four areas of interactions are all coupled together allowing for nonlinear effects, such as alteration of the optical and thermal properties by time-dependent variations of temperature. This coupling is done explicitly by the operator splitting method, in which the time advance of each process is calculated using the most recent data from the other processes. The accuracy of this procedure is fixed with time-step controls, ensuring a converged solution.

Applications of LATIS

To date, LATIS has been used to simulate both photothermal and photomechanical laser-tissue interactions. Photochemical applications are planned for future

work in the areas of cancer and arthritis treatment. In the photothermal area, we have used LATIS to study the effects of dynamic optical properties on laser dosimetry¹² (which we summarize below as a detailed example of LATIS in action), welding of intravascular patches,^{13,14} and the thermal environment for general tissue welding.¹⁵ In the photomechanical area, we have applied LATIS to study high-precision tissue ablation with ultrashort pulses¹⁶ and laser thrombolysis for stroke therapy.¹⁷

Laser Dosimetry with Dynamic Optics

Many laser applications are based on raising the temperature of a localized region of tissue for a certain period of time to cause necrosis or other alterations, such as tissue fusion. In these photothermal applications, the local energy dose (energy/unit mass) delivered to the tissue is a critical parameter.

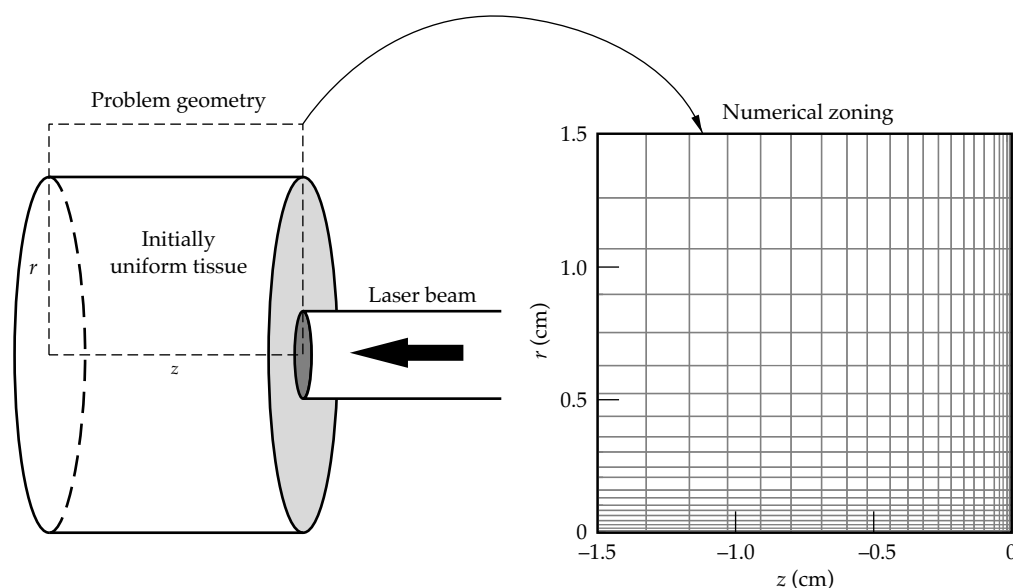
Dynamic optics is defined as the alteration of tissue optical properties by laser irradiation. The effects of dynamic optics on the total dose to the tissue, the size of the damaged region, and the reflected light pattern are very important for photothermal applications of lasers, such as tumor treatments.¹⁸ In this section, we illustrate the application of LATIS to a problem in which the laser scattering coefficient and the blood perfusion change due to thermal damage. We focus on the size of the damage region, and we study how dynamic optics effects vary with the laser-irradiation and tissue parameters.

We chose characteristic, but “generic,” tissue properties to demonstrate the capabilities of LATIS and to illustrate the physical effects involving dynamic optics. The optical properties were those of dog myocardium

at a laser wavelength of 630 nm. The dynamic scattering coefficient was a linear combination of an undamaged and a damaged coefficient: $\mu_s = \mu_u f_u + \mu_d f_d$, where the tissue f_u and f_d are calculated as described in the paragraph following Eq. (1). The scattering coefficients were $\mu_u = 50 \text{ cm}^{-1}$ and $\mu_d = 350 \text{ cm}^{-1}$. The absorption coefficient was fixed at $\mu_a = 0.3 \text{ cm}^{-1}$. Such parameters are also typical of many other soft tissues in the 630–800-nm range. Thermal properties (heat capacity and conductivity) were taken to be those of water, accurate to 30% for most tissues.¹⁹ Damage rate coefficients were fit to average data for whitening of several tissues: dog prostate, dog heart, and rat and pig liver. The coefficients used in Eq. (1) were $\Delta S = 68.2 \text{ cal/deg/mole}$ and $\Delta H = 45.79 \text{ kcal/mole}$. With these coefficients, the damage time scale ($1/k$) varies rapidly with temperature from 100 s at 65°C to 0.5 s at 90°C. In the simulations, the temperature was kept near 72.5°C, at which the damage time scale was 20 s. We also included temperature and damage effects on the blood perfusion.²⁰ The temperature-dependent coefficient increased linearly by a factor of four between 37°C and 42°C to model increased perfusion due to vessel dilation. It was constant at temperatures above 42°C. The damage-dependent coefficient was an exponential cutoff of the perfusion with the damage integral to account for vessel coagulation.

A standard case was defined with the following parameters: laser pulse length 60 s, laser spot size (radius) = 1 mm, scattering anisotropy factor = 0.9, and blood perfusion rate = 0.4 mL/g/min. The laser irradiation pattern was assumed circular with a constant intensity distribution, and the tissue was assumed initially homogeneous. The irradiation geometry and problem zoning are shown in Fig. 3. Fine zones were placed near the laser spot,

FIGURE 3. The laser-tissue interaction is modeled in cylindrical geometry, with fine zoning near the laser spot and course zones far from the spot.
(50-03-0796-1586pb01)



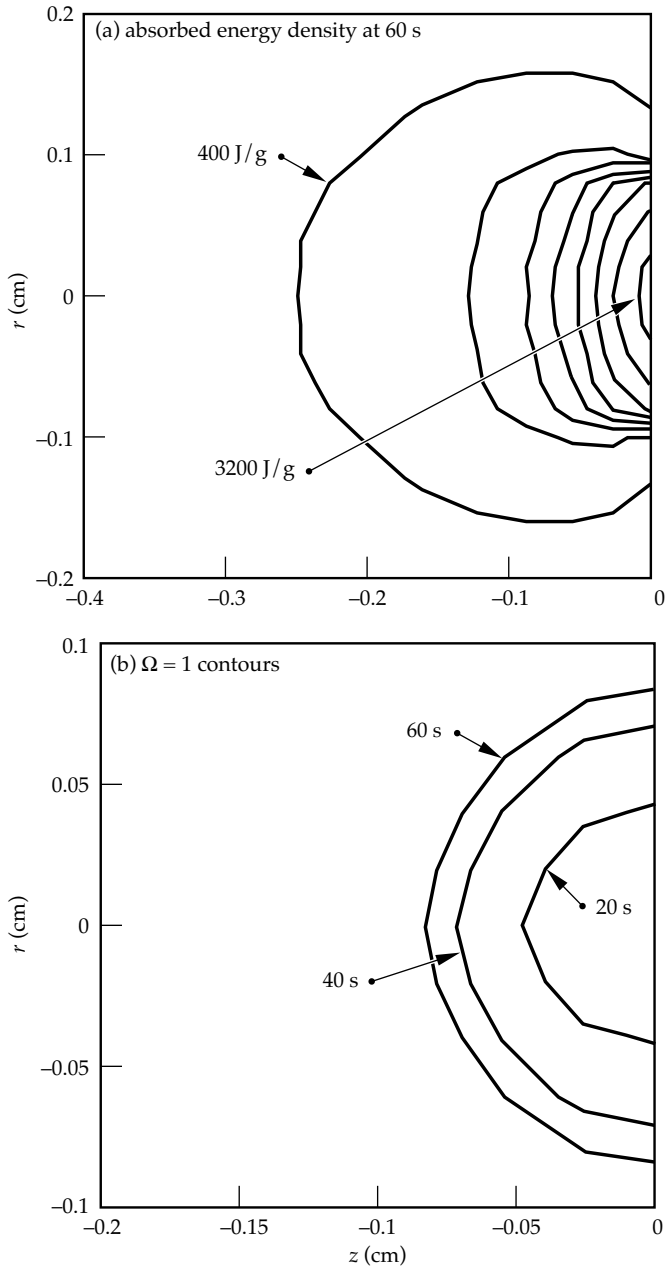


FIGURE 4. The total absorbed energy density integrated over the 60-s pulse is shown in (a). The contour intervals are equal. Laser and tissue conditions are for the standard case. This pattern reflects the light distribution. The damage region ($\Omega = 1$) is shown at various times during the pulse in (b). It grows due to heat diffusion and time-accumulation of damage. (50-03-0796-1587pb01)

where the highest resolution was desired, while courser zones were used far from the laser deposition region. This zoning technique increased the problem resolution while maintaining a relatively small number of zones.

The laser intensity was controlled by a thermostat function that keeps the surface temperature of the directly irradiated region within a desired range. This type of control is motivated by clinical considerations,

such as achieving a maximum damage rate over a specified volume without approaching temperatures near 100°C at which tissue dehydration might occur. We actively controlled the laser intensity by monitoring the average temperature in a 3×3 set of tissue zones within the laser spot. We turned the laser off when the temperature exceeded the desired maximum and then turned it back on when the temperature dropped below the desired minimum. We chose a minimum of 70°C and maximum of 75°C . This technique enabled a very good control of the damage progress and avoided adverse effects associated with dehydration or vaporization as temperatures approached 100°C . Such a temperature-control technique has recently been demonstrated experimentally using infrared radiometry by several groups.^{21,22}

Results for the distribution of absorbed laser energy and the damage zone for a simulation of the standard case are shown in Figs. 4(a) and 4(b). The absorbed laser light reflects the time-average light distribution, since the absorption coefficient is constant. Due to heat diffusion, the temperature distribution (not shown) extended further from the laser focal region than the laser deposition. The size of the damage zone, as indicated by the $\Omega = 1$ contours of Fig. 4(b), grew in time, due to both heat diffusion beyond the energy deposition region and the increasing time for accumulation of damage.

We now compare the damage zone ($\Omega \geq 1$) for the standard case with dynamic optics to that with static optics in Fig. 5. By static optics we mean a simulation in which the scattering coefficient was kept fixed at its undamaged value even though the tissue became damaged. It is clear that the inclusion of dynamic optics reduces the size of the damage zone. To measure this reduction, we defined a damage ratio as the depth of the damage zone with dynamic optics relative to that without dynamic optics:

$$D \equiv \frac{z(\Omega = 1) \text{ dynamic}}{z(\Omega = 1) \text{ static}} \quad (2)$$

For the standard case, as shown in Fig. 5(a), we found $D = 0.67$. For a larger spot size ($r = 0.5 \text{ cm}$), shown in Fig. 5(b), the effect of dynamic optics was somewhat less than for the standard case— $D = 0.77$.

We performed a parametric study that quantified the reduction in the damage zone caused by dynamic optics. For each parameter variation, we performed two simulations—one with dynamic optical coefficients and one with static coefficients. We then formed the damage ratio as defined above. The parameter variations and resultant damage ratios are listed in Table 1.

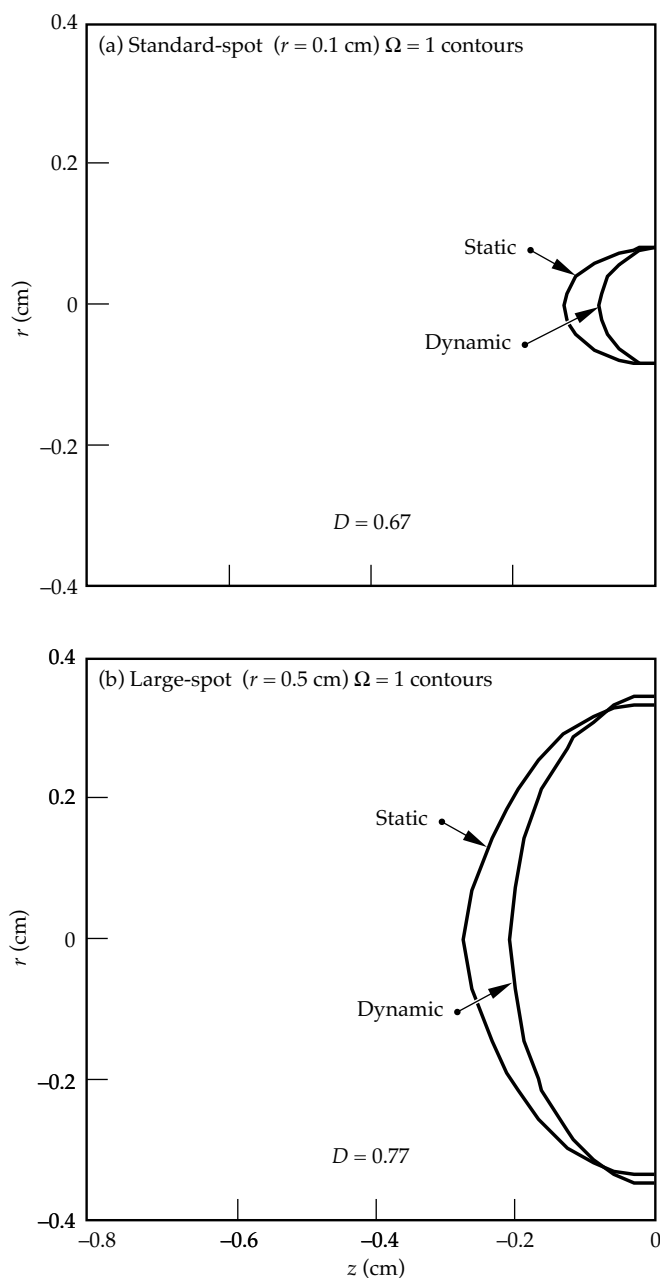


FIGURE 5. The size of the damage regions is reduced by dynamic optics, as shown for the standard case in (a) and for a case with a large spot in (b). The effect of dynamic optics is greater for the standard spot than for the large spot. All curves are for the end of the pulse (at 60 s). (50-03-0796-1588pb01)

The variation with spot size is the greatest. It can be understood by comparing the spot size to the diffusive optical penetration depth $\delta = [3\mu_a(\mu_s + \mu_a)]^{-1/2}$ (see Ref. 1, Chap. 6). For the undamaged tissue, $\delta = 0.46$ cm; for the damaged tissue, $\delta = 0.18$ cm. For spot sizes larger than δ (the case of 0.5 cm spot size), the deposition region is properly given by δ , which scales as $\mu_s^{-1/2}$ for $\mu_s \gg \mu_a$ as is the case. For small spot sizes, the laser light scatters out of the beam, leading to smaller

TABLE 1. Parameter variations and corresponding damage ratios.

Parameter variation	Damage ratio
Standard case	0.67
Short pulse (20 s)	0.76
Long pulse (180 s)	0.63
Small spot (0.01 cm)	0.39
Large spot (0.5 cm)	0.77
Isotropic scattering	0.67
No blood perfusion	0.66

deposition region, scaling approximately as μ_s^{-1} . This higher dependence on μ_s leads to the relatively larger effect of dynamic optics for the smaller spots. The variation with pulse length stems from the relationship to the typical damage time scale. We controlled the surface temperature to an average value of 72.5°C, which gave a characteristic damage time scale of 20 s. Thus pulses of about 20 s or less do not have enough time to produce a large damage zone and therefore show less difference between the dynamic optics and the static optics cases as indicated in Table 1. We also explored variations in the isotropy of scattering and the blood perfusion rate. The isotropic scattering case assumed smaller scattering coefficients, so that the "reduced scattering coefficient" $\mu_s' = \mu_s(1 - g)$ was the same as for the standard case with $g = 0.9$. This was found to have very little effect on the simulation results. The case with no blood perfusion showed 10% larger damage depth in both dynamic and static cases, but very little differential effect, as seen in Table 1.

In summary we see that dynamic optics reduces the depth of damage by about 33% in most cases, with the greatest sensitivity to the irradiation spot size and pulse length. This study illustrates the importance of including such nonlinear effects in designing protocols for laser thermotherapies. Projects on thermotherapy for benign prostate hyperplasia and laser-tissue welding are currently in progress in which similar modeling is being used to design experiments and to compare directly with measured data.

Summary

The LATIS computer program is being developed to treat all of the important aspects of laser-tissue interaction including laser propagation, thermal effects, material effects, and hydrodynamics, in a fully coupled manner. In LATIS, we now have a powerful tool for designing new medical devices and procedures through computational simulation. LATIS is being applied to areas of photothermal therapy, tissue welding, hard-tissue ablation, and thrombolysis.

Notes and References

1. A. J. Welch and M. J. C. Van Gemert, *Optical-Thermal Response of Laser-Irradiated Tissue* (Plenum Press, New York, 1995).
2. G. B. Zimmerman and W. L. Kruer, *Commun. Plasma Phys. Controlled Fusion* **11**, 82 (1975).
3. P. F. DuBois, *Computers in Physics* **8**, 70 (1994).
4. L. G. Henyey and J. L. Greenstein, *Astrophys. J.* **93**, 70 (1941).
5. S. L. Jacques, C. A. Alter, and S. A. Prahl, *Lasers Life Sci.* **1**, 309 (1987).
6. W. E. Alley, *A Maxwell equation solver for the simulation of moderately intense ultra-short pulse laser experiments*, p. 160, UCRL-LR-105820-92, Lawrence Livermore National Laboratory, Livermore, CA (1992).
7. Y. I. Cho, ed., "Bioengineering Heat Transfer," *Advances in Heat Transfer*, vol. 22 (Academic, San Diego, 1992).
8. C.-S. Orr and R. C. Eberhart, *Optical-Thermal Response of Laser-Irradiated Tissue*, p. 367, A. J. Welch and M. J. C. Van Gemert, Eds., Plenum Press, New York, 1995.
9. R. M. More, K. H. Warren, D. A. Young, and G. B. Zimmerman, *Phys. Fluids* **31**, 3059 (1988).
10. D. A. Young and E. M. Corey, *J. Appl. Phys.* **78**, 3748 (1995).
11. J. Pearce and S. Thomsen, *Optical-Thermal Response of Laser-Irradiated Tissue*, p. 561, A. J. Welch and M. J. C. Van Gemert, Eds., Plenum Press, New York, 1995.
12. R. A. London, M. E. Glinsky, G. B. Zimmerman, D. C. Eder, and S. L. Jacques, *Laser-Tissue Interaction VI* (SPIE—The International Society for Optical Engineering, Bellingham, WA, 1995; *Proc. SPIE* **2391**), p. 431.
13. M. E. Glinsky, R. A. London, G. B. Zimmerman, and S. L. Jacques, *Laser-Tissue Interaction VI* (SPIE—The International Society for Optical Engineering, Bellingham, WA, 1995; *Proc. SPIE* **2391**), p. 262.
14. M. E. Glinsky, R. A. London, G. B. Zimmerman, and S. L. Jacques, *Medical Applications of Lasers III* (SPIE—The International Society for Optical Engineering, Bellingham, WA, 1996; *Proc. SPIE* **2623**), p. 349.
15. D. J. Maitland, D. C. Eder, R. A. London, M. E. Glinsky, and B. A. Soltz, *Lasers in Surgery: Advanced Characterization, Therapeutics, and Systems VI* (SPIE—The International Society for Optical Engineering, Bellingham, WA, 1996; *Proc. SPIE* **2671**), p. 234.
16. R. A. London et al., *Laser-Tissue Interaction VII*, Ed. S. L. Jacques, *Proc. SPIE* **2681**, Bellingham WA, 1996, p. 233.
17. M. Strauss et al., *Lasers in Surgery: Advanced Characterization, Therapeutics, and Systems VI*, (SPIE—The International Society for Optical Engineering, Bellingham, WA, 1996; *Proc. SPIE* **2671**), p. 11.
18. G. Muller and A. Roggan, *Laser-Induced Interstitial Thermotherapy* (SPIE—The International Society for Optical Engineering, Bellingham, WA, 1995; *Proc. SPIE*).
19. J. W. Valvano, *Optical-Thermal Response of Laser-Irradiated Tissue*, p. 445, A. J. Welch and M. J. C. Van Gemert, Eds., Plenum Press, New York, 1995.
20. B.-M. Kim, S. L. Jacques, S. Rastegar, S. L. Thomsen, and M. Motamedi, *Laser-Tissue Interaction VI* (SPIE—The International Society for Optical Engineering, Bellingham, WA, 1995; *Proc. SPIE* **2391**), p. 443.
21. B. Lobel et al., *Lasers in Surgery: Advanced Characterization, Therapeutics, and Systems V* (SPIE—The International Society for Optical Engineering, Bellingham, WA, 1995; *Proc. SPIE* **2395**), p. 517.
22. I. Cilesiz, E. K. Chan, A. J. Welch, and S. L. Thomsen, *Lasers in Surgery: Advanced Characterization, Therapeutics, and Systems V* (SPIE—The International Society for Optical Engineering, Bellingham, WA, 1995; *Proc. SPIE* **2395**), p. 523.

THE ENERGETICS OF GAS-FILLED HOHLRAUMS

<i>T. J. Orzechowski</i>	<i>D. E. Desenne*</i>	<i>A. G. Dulieu*</i>
<i>D. Juraszek*</i>	<i>R. L. Kauffman</i>	<i>R. K. Kirkwood</i>
<i>H. N. Kornblum</i>	<i>B. J. MacGowan</i>	<i>D. S. Montgomery</i>
<i>L. V. Powers</i>	<i>A. L. Richard*</i>	<i>G. F. Stone</i>
<i>L. J. Suter</i>	<i>R. J. Wallace</i>	

Introduction

The x-ray drive generated in a laser-driven hohlraum ablates the high-Z wall material¹⁻³ that can then fill the hohlraum with a high-density plasma during the laser pulse. This high-Z plasma absorbs the laser energy in regions well removed from the original location of the hohlraum wall. Because this plasma is high-Z, the conversion from laser energy to x rays can occur in a volume of the hohlraum that is not as well localized as the original hohlraum wall location, and this in turn can effect the drive symmetry in an unwanted way.⁴ To mitigate the problems associated with this high-Z filling of the hohlraum, a low-Z material is introduced to tamp the high-Z wall.⁵ This tamper is typically less than one-tenth of the critical density n_c for the laser light used to illuminate the hohlraum. However, the pressure associated with the tamper is sufficient to keep the hohlraum wall material from moving significant distances into the hohlraum interior, thus preventing the laser deposition region from moving large distances during the laser pulse.

In the experiments we discuss here, the tamper is generated from a gas that is confined in the hohlraum. These gas-filled hohlraums must be designed with low-mass windows over the laser entrance holes (LEHs) and diagnostic holes to confine the gas. Thin (3500-Å) polyimide ($C_{22}H_{10}N_2O_5$) windows cover all of the apertures to provide a gas-tight seal. The laser light rapidly burns through the windows and gas, heating and ionizing the low-Z material as it propagates to the hohlraum wall. In the standard scale-1 Nova hohlraums, this occurs in about 200 ps. We have studied the effect of methane (CH_4), propane (C_3H_8), and neopentane

(C_5H_{12}) on the hohlraum performance. When fully ionized, these gases at 1 atm generate plasmas with 0.025, 0.04, and 0.1 n_c , respectively. As the hohlraum wall moves inward, this low-Z plasma is compressed and the density is slightly higher than the “atmospheric” densities.

The laser beam interacting with the low-density plasma can generate parametric instabilities that can scatter the laser light.⁶ If this scattered laser light leaves the hohlraum, this reduces the energy available to produce the x-ray drive. This article presents the results of hohlraum energetics measurements that are designed to quantify the energy losses in gas-tamped hohlraums. The hohlraum drive is characterized by a Planckian distribution of x rays that defines the hohlraum temperature. We determine this hohlraum temperature by measuring the radiation associated with the interior hohlraum wall, which differs slightly from the actual hohlraum temperature. In addition, we measure the time-dependent losses associated with the stimulated processes: stimulated Brillouin scattering (SBS) and stimulated Raman scattering (SRS).⁶

Measurements of Hohlraum Energy Balance

Hohlraum Temperature Measurements

The gas-tamped hohlraums (shown in Fig. 1) are required to hold 1 atm of the desired tamping gas (CH_4 , C_3H_8 , or C_5H_{12}). This conventional scale-1 Nova hohlraum (2700 μm long and 1600 μm diam) has 75% LEHs (1200 μm diam) and a nominal 500- μm -diam Dante hole, which is lined with Be to reduce the closure of this aperture during the drive pulse. The Dante hole is positioned 20° down from horizontal in the hohlraum’s midplane. All of the apertures are covered

*Centre D’Etudes de Limeil-Valenton, France

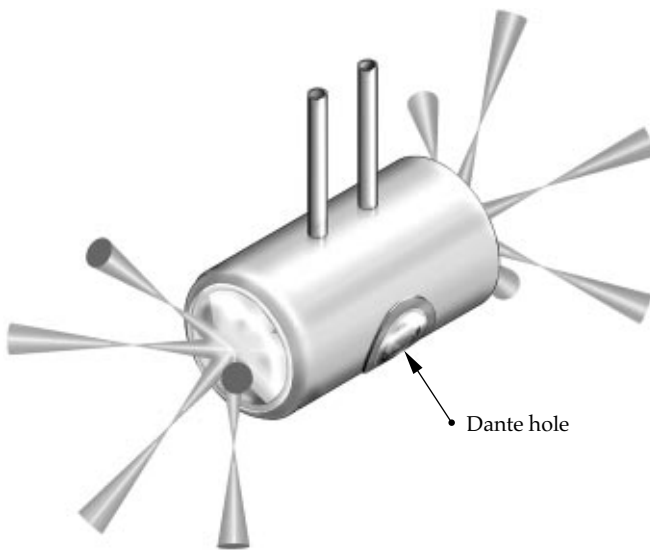


FIGURE 1. Schematic of a gas-filled hohlraum, showing five laser beams entering from each end. The fill gas is admitted through small tubes in the top of the hohlraum. The hohlraum temperature is monitored with an absolutely calibrated time-dependent soft x-ray spectrometer (Dante) that monitors the x-ray emission from the hohlraum wall through a small aperture. All of the apertures are covered with a 3500-Å polyimide membrane to provide a gas-tight seal. (08-00-0596-1242pb01)

with a 3500-Å-thick polyimide membrane to provide a gas-tight seal. The gas enters the side of the hohlraum through two stainless-steel tubes (260 μm o.d. and 80- μm wall thickness). The total area occupied by these tubes is insignificant to the total interior area of the hohlraum.

Nova drives the hohlraum with five beams on each end, and the laser pulse is shaped in time with a foot and a peak. Figure 2 shows examples of the incident laser pulse shape, illustrating the laser power as a function of time and the SBS and SRS time histories, for an empty and a C_5H_{12} -filled hohlraum.[†] The laser beams are aimed at the center of the LEHs and defocused 1000 μm to give a laser spot size of $400 \times 600 \mu\text{m}$ at the hohlraum wall. The spatially averaged laser intensity at the hohlraum wall (without subtracting the SBS and SRS losses) is then $\sim 3 \times 10^{14} \text{ W/cm}^2$ in the foot and rises to $\sim 10^{15} \text{ W/cm}^2$ in the peak of the pulse.

The hohlraum temperature is measured with Dante,⁷ which is an absolutely calibrated 10-channel, time-resolved soft-x-ray spectrometer. This diagnostic is located on the target chamber wall and views the hohlraum midplane along a line-of-sight 72° from vertical. The Dante views a section of the hohlraum wall that is not illuminated by the laser beams.

[†]The absorbed laser power is the difference between the incident and scattered laser power.

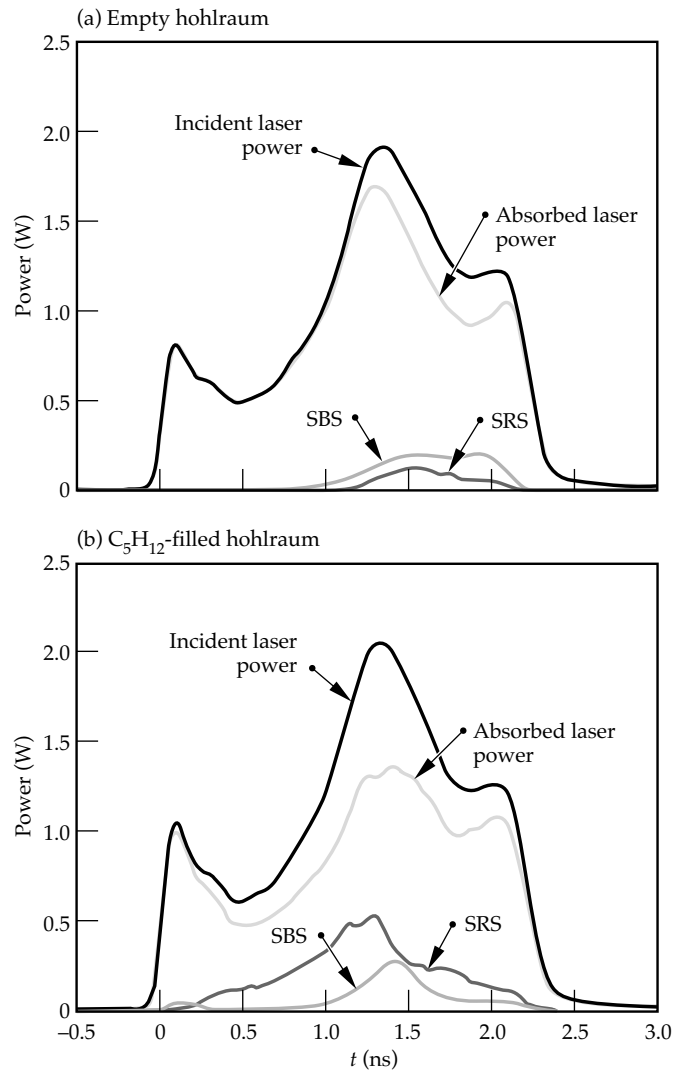


FIGURE 2. Measured incident laser pulse and the measured SRS and SBS for (a) an empty hohlraum and (b) a C_5H_{12} -filled hohlraum. The absorbed laser power is the difference between the incident power and the backscattered optical signal. (20-05-0796-1549pb01)

Dante measures the hohlraum wall temperature, which differs from the actual hohlraum temperature by a factor of the albedo (x-ray re-emission coefficient) to the 0.25 power. This corresponds to about a 5% correction to the hohlraum temperature, or $\sim 10 \text{ eV}$ at the peak of the drive. All of the measurements shown here correspond to the Dante (or wall) temperature.

Figure 3 shows the Dante measurements for various gas-filled hohlraums (the temperature histories for empty hohlraums with no windows; empty hohlraums with windows on the LEHs but no gas fill; and hohlraums filled with CH_4 , C_3H_8 , or C_5H_{12}). Each curve corresponds to two or three measurements with the same configuration (windows and/or gas fill), and the error bars correspond to the minimum and maximum measurement at each configuration. These data

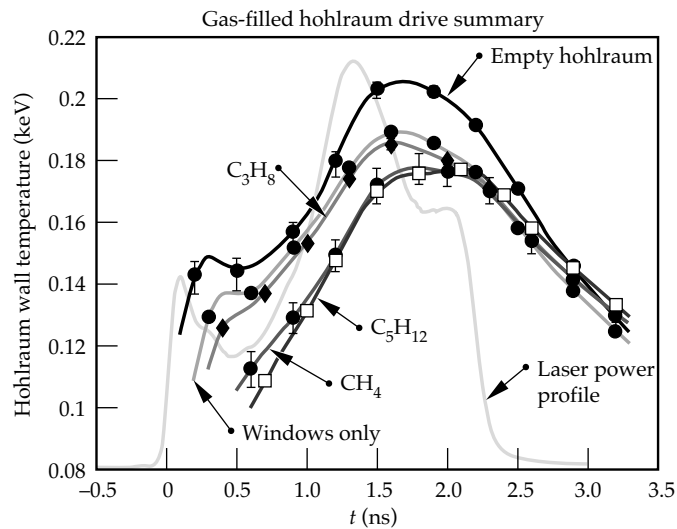


FIGURE 3. Hohlraum wall temperature as a function of time for empty hohlraums (with and without windows) and hohlraums with different gas fills (CH_4 , C_3H_8 , and C_5H_{12}). (20-05-0796-1548pb01)

show the drive to be quite reproducible. As expected, the addition of the gas causes an overall drop in the hohlraum temperature. However, the magnitude of the temperature drop cannot be attributed solely to the heat capacity of the gas and window material.

Two features are immediately apparent. First, the foot of the x-ray drive is significantly degraded in the hohlraum with windows only and the gas-filled hohlraum. This is due to the laser energy expended burning through the windows and then propagating through the gas. The small peak at the beginning of the laser pulse has completely disappeared, and the foot of the x-ray drive pulse rises more slowly. Second, the peak temperature decreases as the plasma density increases. Only a small part of this temperature decrease is attributable to the heat capacity of the gas; the major reduction in hohlraum drive can be attributed to backscattering (SRS and SBS) in the gas (discussed in the following section). Another interesting observation is the drop in temperature when the hohlraum has windows only and no gas. As can be seen from the data, the largest single temperature drop occurs when windows are added to the hohlraum.

Backscattered Energy Measurements

Nova's beamline 7 (BL7) is equipped with diagnostics⁸ to monitor the laser energy that is reflected from the hohlraum via SBS and SRS. The diagnostics include calorimeters to monitor the total backscattered optical light energy (via each of the two processes) and streaked spectrometers to give the time-dependent optical spectra associated with each of the scattering mechanisms.

The full aperture backscatter station (FABS) measures the radiation reflected back into the $f/4.3$ lens while the near beam imager (NBI)⁹ monitors the optical light scattered at angles up to 20° . The temporal evolution of the backscattered radiation is inferred from normalizing the frequency- and time-integrated spectrum to the total backscattered energy.

Figure 4 shows the total reflected energy for the various gases and for the empty and windows-only hohlraums. In the empty hohlraum, most of the energy is reflected via SBS (6%) while an additional 3% is lost via SRS. When gas is introduced, the SRS becomes the dominant backscatter mechanism. The SRS level increases with the electron density n_e . While the time-integrated fraction of energy that is backscattered via stimulated processes can reach significant levels ($\sim 25\%$ SRS + SBS in the C_5H_{12} -filled hohlraums), the time-dependent backscatter shows that during the laser pulse, the levels of backscatter can be even higher (see Fig. 2). Most of the scattered energy is associated with the main peak of the laser pulse, which starts about 1 ns into the pulse. This corresponds to the time at which the SRS and SBS gains are the largest due to the higher laser intensities (in the latter part of the pulse).

The laser beams used in these experiments are the standard, unsmoothed Nova laser beams. These beams include hot spots that can achieve intensities in excess of the average intensities quoted above. These higher intensities can exacerbate the growth of instabilities. To mitigate the problem of energy lost through backscattering, we intend to smooth the laser beams with random

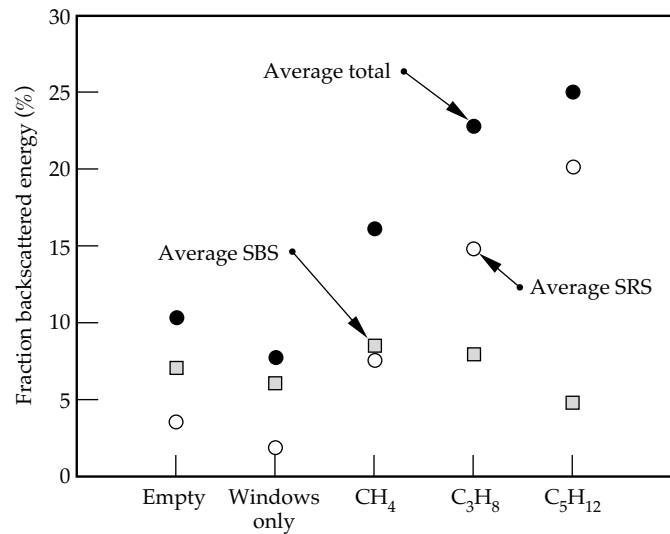


FIGURE 4. Fraction of backscattered laser energy (SRS, SBS, and their sum) for various hohlraum configurations (empty or windows only) and from hohlraums with various gas fills (CH_4 , C_3H_8 , and C_5H_{12}). (20-05-0796-1551pb01)

phase plates (RPPs) or kinoform phase plates (KPPs).⁸ Figure 5 shows the effect of beam smoothing on the backscattered laser signal. We show the total backscatter levels for CH₄- and C₃H₈-filled hohlraums, using the standard Nova beam and a beam (BL7) smoothed with either a RPP or a KPP. The backscattered signal from the smoothed beam is a factor of 4 to 6 less than that for the unsmoothed beam.

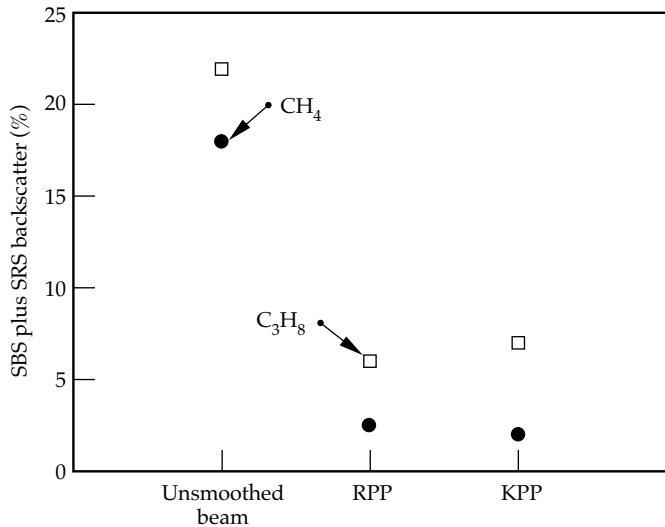


FIGURE 5. Fraction of backscatter laser energy (SRS plus SBS) in CH₄ or C₃H₈ gas corresponding to an unsmoothed laser beam and a laser beam smoothed with a random phase plate (RPP) or a kinoform phase plate (KPP). (20-05-0796-1550pb01)

An anomaly in these data is the energetics of the hohlraum with windows only. Note that the total backscatter fraction is slightly less than that for the standard, empty hohlraum. However, the temperature drop shown in Fig. 3 indicates a significant difference in absorbed energy. Comparing the integral over time of the radiated power (T_r^4) shows a difference of approximately 30% in total radiated energy while the backscatter energy shows virtually no difference. Looking again at Fig. 3, we see that the largest single energy difference is associated with attaching the windows to the hohlraum. We can speculate that the hohlraum is somehow contaminated in the process of installing the windows and that this contamination carries over to the remainder of the hohlraums with gas. On another series of measurements (less complete and with a slightly different temporal profile to the laser pulse), we saw a much smaller temperature drop associated with the hohlraum with windows only and no gas fill. There was no corresponding change in the relative levels of SRS and SBS. The

contamination, if it is the problem, then, is associated with the fabrication technique and can vary from one set of hohlraums to another.

Modeling the Hohlraum Energetics

We use LASNEX¹⁰ to simulate the time-dependent drive in the gas-tamped hohlraums. This code does not calculate the SRS and SRS losses; these losses are incorporated by using the net absorbed laser energy (i.e., measured incident minus SRS and SBS losses) in the calculation. We find that the code does not quite predict the level of temperature reduction that is observed in the experiment. The observed temperature drop in the CH₄-filled hohlraum is 20 eV, while the calculated temperature drop is 12 to 17 eV. This corresponds to a measured reduction in flux of 32% and a calculated reduction in flux of 21 to 28%. Similarly for C₃H₈, the measured reduction in temperature (flux) is 26 eV (40%), while the calculated drop in temperature (flux) is 18 to 21 eV (30 to 34%). This range in calculated temperature drop arises from a difference in calculated vs measured temperature as a function of time. The calculated temperature reaches a peak later in time. Simply comparing the peak calculated vs peak measured temperature results in a smaller difference. Looking at the calculated temperature at the time the measured temperature reaches a peak results in the larger difference.

In the modeling, there are two reasons for the reduction in drive in the gas-filled hohlraums. First, the radiation production is reduced because of the tamper. In the untamped hohlraum, the axial stagnation of the high-Z plasma is itself a source of radiation production. In the simulation, this reduced radiation production results in a temperature drop of 4 to 6 eV. Second, the drive is reduced due to decreased laser absorption (SRS and SBS). As mentioned, this part of the physics is added through the measured input power minus the measured SRS and SBS. In the simulation, this results in a 10- to 15-eV temperature drop.

Summary

We measured the time-dependent drive in gas-tamped hohlraums and compared the measurements with simulations. The addition of the gas tamper can result in as much as a 25-eV reduction in peak drive temperature. The overall drop in flux is as much as 40%, which is about 15% more than predicted by LASNEX simulations. Future experiments will use smoothed laser beams that will significantly reduce the levels of backscatter losses. Since these losses are not calculated by LASNEX, the new measurements will lend themselves to more accurate simulation.

Notes and References

1. R. E. Marshak, *Phys. Fluids* **1**, 24 (1958).
2. R. Pakula and R. Sigel, *Phys. Fluids* **28**, 232 (1985); **29**, 1340(E) (1986).
3. M. D. Rosen, *The Physics of Radiation Driven ICF Hohlraums*, Lawrence Livermore National Laboratory, Livermore, CA, UCRL-ID-121585 (1995); to be published in the *Proceedings of the 1995 Plasma-Physics Summer School of the La Jolla Institute for Advanced Physics*, V. Stefan, Ed. (1995).
4. J. D. Lindl, *Phys. Plasmas* **2**, 3933 (1995).
5. J. D. Lindl, *Laser Program Annual Report 1978*, Lawrence Livermore National Laboratory, Livermore, CA, UCRL-50055-78, 2-77 (1978).
6. W. L. Kruer, *The Physics of Laser Plasma Interactions* (Addison-Wesley Publishing Company, Redwood City, CA, 1988).
7. H. N. Kornblum, R. L. Kauffman, and J. A. Smith, *Rev. Sci. Instrum.* **57**, 2179 (1986).
8. B. J. MacGowan, B. B. Afeyan, C. A. Back, R. L. Berger et al., *Phys. Plasmas* **3**(5), 2029 (1996).
9. R. K. Kirkwood, C. A. Back, M. A. Blain, D. E. Desenne et al., "Imaging Backscattered and Near to Backscattered Light in Ignition Scale Plasmas," Lawrence Livermore National Laboratory, Livermore, CA, UCRL-JC-124041 (1996); submitted to *Rev. Sci. Instrum.*
10. G. B. Zimmerman and W. L. Kruer, *Comments on Plasma Physics and Controlled Fusion* **2**, 51 (1975).

FUSION REACTION-RATE MEASUREMENTS— NOVA AND NIF

R. A. Lerche

M. D. Cable

Introduction

Thermonuclear fusion can occur when laser energy compresses and heats a spherical capsule filled with deuterium (DD) or a deuterium–tritium (DT) mixture. A goal of the Inertial Confinement Fusion (ICF) Program is to achieve a compression of 1000 times liquid density at a temperature of ~ 10 keV for a plasma confined for ~ 100 ps.¹ During confinement, fuel atoms undergo fusion and release energy in the form of energetic charged particles, neutrons, and photons. We want to measure the fusion reaction rate as a function of time relative to the incident laser radiation because it is valuable information for researchers studying laser–target interactions. These measurements characterize the coupling of the drive energy to the target, the hydrodynamics of the capsule implosion, and the plasma conditions during peak emission. The fusion reaction rate, often referred to as “burn rate” or “burn history,” is a sensitive indicator of our ability to accurately model energy transport between the laser and target.

The burn history for a target can be measured by monitoring the production rate of the fusion reaction products. At Nova, most measurements are made by recording the arrival time of 14-MeV neutrons produced in $T(d,n)^4\text{He}$ fusion reactions using a fast (30-ps resolution) detector several centimeters from the target.² Since fusion products are nearly monoenergetic and the target’s emission region is submillimeter in size, the recorded signal is the target burn history with a time-of-flight delay dependent on the target-to-detector distance.

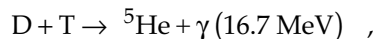
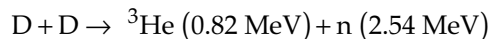
At the future National Ignition Facility (NIF), it is unlikely that the target burn history can be measured with the direct neutron technique used at Nova. This is because the thermal motion of the reacting plasma ions causes a broadening of the neutron energy spectrum, which in turn causes a temporal spread in neutron flight time to a detector. The time spread increases with target-to-detector distance. At NIF, there will be an exclusion zone around the target to minimize damage to blast shields and optics caused by ablated material. At

anticipated detector distances of 1 to 5 m, the resulting spread in the neutron arrival times will mask burn-history information. Gamma rays, however, are virtually unaffected by plasma temperature and have negligible temporal dispersion at a distant detector. For these reasons, we are investigating techniques that use fusion gamma rays to measure burn history.

This article begins with a review of detector system characteristics required for making reaction-rate measurements. A description of the neutron-based measurement system implemented at Nova is followed with examples of reaction-rate measurements made for a variety of Nova targets. Finally, we discuss the challenge of measuring burn history at NIF and summarize current experiments associated with developing a gamma-ray-based technique to measure burn history.

Measurement Concept

One method for measuring the fusion reaction rate of an ICF target is to monitor the production rate of a fusion reaction product. Reactions available for DD- and DT-filled targets are



where the particle energy is indicated in parentheses. The spectrum for each fusion product is nearly monoenergetic. The charged particles are slowed by Coulomb interactions with plasma ions and electrons before leaving the target. Most neutrons and gamma rays, however, escape from the target without collision. Since the reaction region is submillimeter in size, both neutron and gamma-ray temporal distributions at points outside the target preserve burn history. For this

reason, burn history may be measured with either a fast neutron or gamma-ray detector placed some distance away from the target. Since confinement times can be <100 ps, detectors with time resolutions of ~ 20 ps are desirable.

Temporal resolution for a neutron-based measurement is limited by the plasma ion temperature, the target-to-detector distance, and the detector thickness. Thermal motion of the reacting plasma ions causes a broadening of the neutron energy spectrum.³ For neutrons leaving a target at the same instant, the energy spread causes a time spread in their arrival at a detector. The time spread Δt_e , which is proportional to distance, is given by $\Delta t_e = 1.22\sqrt{T} \times d$ for DT neutrons and $\Delta t_e = 7.88\sqrt{T} \times d$ for DD neutrons, where Δt_e is in ps, ion temperature T is in keV, and target-to-detector distance d is in cm. The detector must be placed close to the target to keep the time spread small. For example, to keep Δt_e below 20 ps for a 1-keV plasma requires $d < 16.4$ cm for DT neutrons and < 2.6 cm for DD neutrons.

A neutron detector must also be thin to achieve 20-ps response. In a detector, there is an uncertainty about the exact point of neutron interaction, and a corresponding uncertainty in the instant of the interaction. The uncertainty Δt_x is proportional to the detector thickness Δx and is given by $\Delta t_x = \Delta x / v_n$, where v_n is the speed of the neutron. Thus, to achieve a 20-ps response requires $\Delta x < 1$ mm for DT neutrons and < 0.4 mm for DD neutrons.

The less restrictive requirements of DT neutrons on target-to-detector distance and detector thickness are advantages for selecting DT fuel over DD fuel for making burn-history measurements. Furthermore, the larger fusion cross section for DT reactions results in a neutron yield nearly 100 times greater than for a hydrodynamically equivalent DD-filled target, an important consideration when working with low-yield targets. The 16.7-MeV fusion gamma rays were never seriously considered for Nova reaction-rate measurements because of the low branching ratio (5×10^{-5}) for the reaction.^{4,5} There simply were not enough gamma rays to make burn-history measurements at Nova.

30-ps Neutron Detector

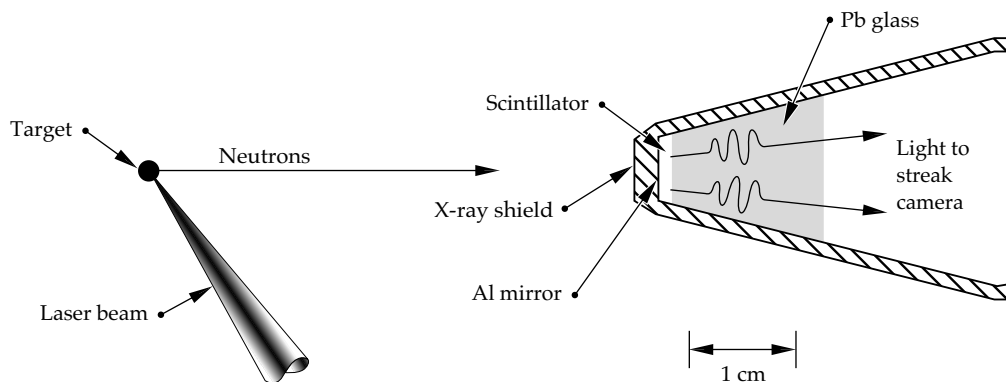
A critical step in our effort to record reaction rates with 30-ps resolution was the development of a sensitive, high-speed neutron detector. RIC (radiation-induced conductivity) detectors,⁶ the fastest available before we developed a streak-camera-based instrument, were not sensitive and fast enough. Coupled to a 7-GHz transient recorder, RIC detectors had an impulse response of 125 ps full-width half-maximum (FWHM) and required yields of $> 5 \times 10^{10}$ DT neutrons for a reaction-rate measurement.

Our detector is based on the fast rise time of a commercially available plastic scintillator. A thin piece of BC-422⁷ converts neutron kinetic energy into light. As neutrons pass through the scintillator, some of them have elastic collisions with hydrogen nuclei. The recoil protons quickly transfer their kinetic energy to luminescent sites in the scintillator. For BC-422 the light output has a rise time < 20 ps and a decay time of ~ 1.2 ns. The temporal distribution of the emitted light is the convolution of the neutron temporal distribution with the scintillator response. Burn-history information is encoded in the leading edge of the light pulse. A fast optical streak camera (< 15 ps FWHM) records the signal.

The detector is the result of three technology advances. First we developed a detector concept based on the fast rise time of a plastic scintillator. At that time, the fastest plastic scintillators had nanosecond decay times and were believed to have rise times > 100 ps, hardly fast enough for 30-ps measurements. Second, an experimental search for a fast-rise-time scintillator using a pulsed electron beam at the LLNL linac identified NE-111 (BC-422) as a potential candidate.⁸ Later experiments at Nova with short bursts of x rays generated by irradiating gold disk targets with 20-ps-wide laser pulses demonstrated the scintillator rise time to be < 20 ps.⁹ Third, we discovered that our streak camera could be operated with a wide input slit without losing temporal resolution.¹⁰ Wide slit operation allowed us a tenfold increase in system sensitivity by using a 1-mm-wide slit rather than the more typical 100- μ m-wide slit used with other streak cameras.

Figure 1 shows the scintillator configuration. A 6-mm-diam, 1-mm-thick piece of BC-422 is housed in a Hevimet

FIGURE 1. Detector nose cone configuration. Scintillator must be thin and close to the target to control temporal dispersion. (08-00-0896-1852pb01)



(90% tungsten) nose cone. The front of the nose cone, which is 3 mm thick, shields the scintillator from target x rays, scattered laser light, and target debris. A thin Al layer deposited on one surface of the scintillator acts as a mirror to double the light output directed towards the streak camera. A piece of Pb glass shields the back side of the scintillator from scattered x rays.

The detector system, which is called the NTD (for neutron timing diagnostic), features a nose cone assembly that can be positioned between 2 and 50 cm from the target. An achromatic $f/2$ zoom lens relays the scintillator image along a 4-m optical path to the S-20 photocathode of the streak camera located outside the vacuum chamber. Lens coupling produces minimal temporal dispersion. In contrast, using 4 m of graded-index optical fibers would produce ~ 80 ps of dispersion for the 350- to 450-nm scintillator light. Baffling and a light shield prevent scattered laser light from entering the lens system. Scintillator light passes through a glass window at the vacuum chamber wall. Components inside the chamber can operate at either vacuum or atmospheric pressure. The streak camera image is recorded with a charge-coupled device (CCD) camera. The relatively long distance between target and streak camera is an advantage of this configuration. Background caused by target x rays and neutrons interacting with the streak camera and the CCD decreases inversely with the square of the distance from the target.

Besides recording a neutron-induced signal, the streak camera also records an optical fiducial signal to provide an absolute time base. The Nova facility generates a 100-ps, 0.53- μm , optical timing pulse that is split and distributed to various diagnostic instruments via optical fibers. We insert a 527-ps etalon into its path to form a series of evenly spaced pulses. The first pulse provides an absolute timing reference required to temporally relate the neutron signal to the laser power recorded with other streak cameras with ± 10 -ps precision.¹¹ The pulse train provides a calibration check for the streak camera time base. The optical fiducial amplitude, timing, and pulse shape are easily controlled because they are independent of target type, incident laser energy, and target-to-detector distance. This is not the case when target-generated x rays are used as the fiducial.

Excellent data have been recorded with the NTD. Figure 2(a) shows an image recorded with the scintillator 2 cm from a low-yield target producing 6.7×10^8 DT neutrons. Figure 2(b) shows image exposure versus time averaged across the spatial extent of the neutron signal. Streak camera flat-field and time-base corrections are included in the signal processing. Information about the target burn history is encoded in the leading edge of the pulse.

We obtain the shape of the neutron temporal distribution by deconvolving the effect of the scintillator decay rate from the recorded neutron signal. The result, which is approximately the derivative of the recorded

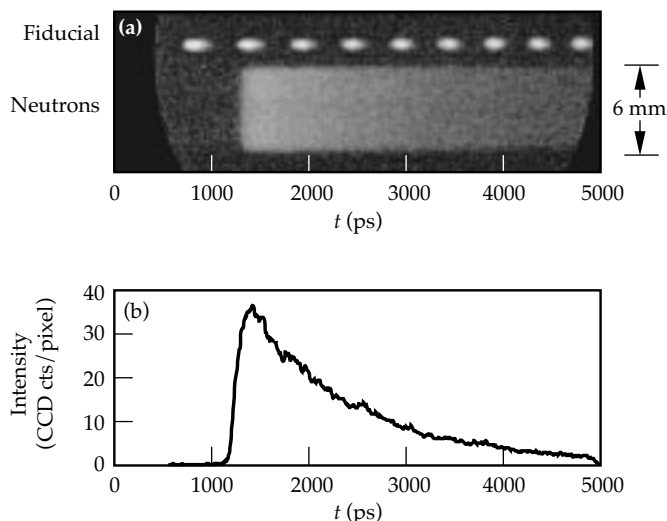


FIGURE 2. Neutron signal. (a) Streak camera image for a target producing 6.7×10^8 DT neutrons. (b) Average neutron signal intensity vs time. Burn history is encoded in the leading edge of the pulse. Pulse tail shows the characteristic decay of the scintillator. The complete burn history for this data is shown in Fig. 3(b). (08-00-0896-1853pb01)

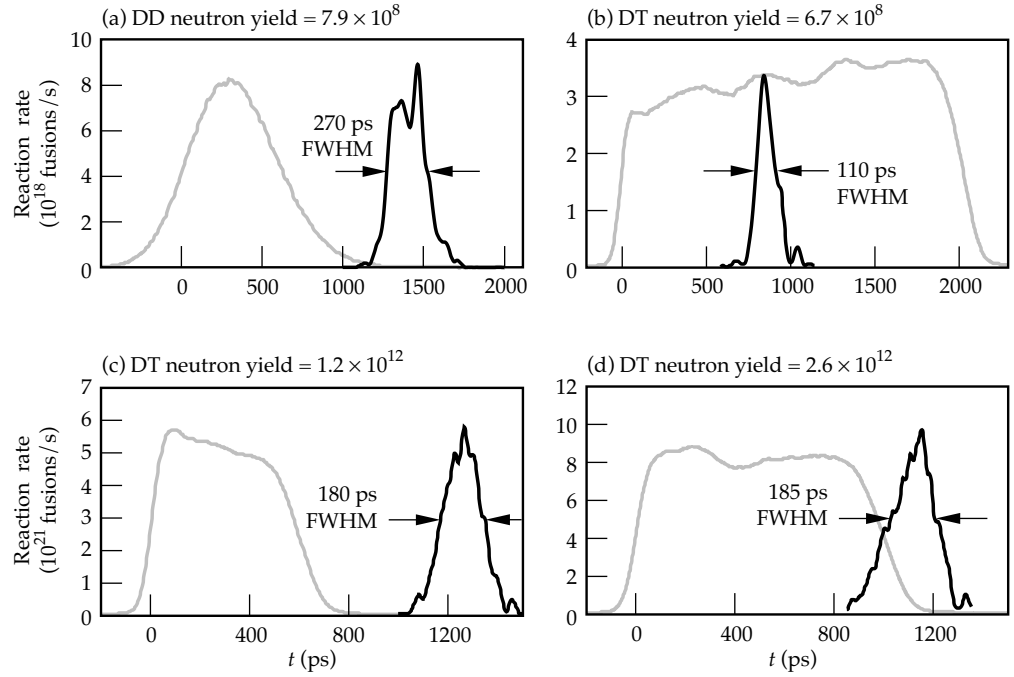
signal, actually represents the convolution of the target burn history with the streak camera response and the derivative of the scintillator rise time. Since the rise time and camera response are both < 20 ps, the deconvolved signals are a good representation of the fusion reaction rate. The quality of each deconvolution is checked by comparing the recorded signal with the convolution of the burn history and the exponential decay of the scintillator.

Nova Reaction-Rate Measurements

Reaction-rate measurements with 30-ps resolution have been made for a variety of Nova targets whose DT yields ranged from 10^8 to 3.6×10^{13} neutrons. Measurements have also been made for targets with DD neutron yields between 10^9 and 10^{11} , but with temporal resolutions of ~ 50 ps. In this section, examples of burn histories for several different target types are presented. The intent of this section is to demonstrate the variety in burn-history signatures, and not to present a detailed examination of the performance of any particular target.

Direct-drive glass-microballoon targets are used for instrument development and calibration at Nova. Burn history is affected by target diameter, fill pressure, and wall thickness along with laser power and beam focusing. Diameters for microballoon targets range from 360 to 1500 μm , fill pressures from 10 to 100 atm, and wall thicknesses from 2 to 8 μm . High-yield targets ($> 10^{12}$ DT neutrons) typically have diameters > 900 μm and are irradiated with temporally flat laser pulses 1 or 1.5 ns long. These targets typically have a burn duration between 175 and 250 ps (FWHM) and an emission time between 700 and 1500 ps after the leading edge of the laser pulse.

FIGURE 3. Reaction rates for four glass microballoon targets irradiated directly with $0.351\text{-}\mu\text{m}$ light. The black curves represent the reaction-rate history; the gray curves show the shape of the laser-power history. The target diameter/wall thickness, fill pressure, and incident laser energy for each experiment are (a) $360\text{ }\mu\text{m}/6\text{ }\mu\text{m}$, 25 atm DD fuel, 15 kJ; (b) $360\text{ }\mu\text{m}/6\text{ }\mu\text{m}$, 25 atm DT fuel, 20 kJ; (c) $800\text{ }\mu\text{m}/3\text{ }\mu\text{m}$, 50 atm DT fuel, 11 kJ; and (d) $1000\text{ }\mu\text{m}/3\text{ }\mu\text{m}$, 50 atm DT fuel, 22 kJ. (08-00-0896-1854pb01)



A small ($360\text{-}\mu\text{m}$) microballoon can have a burn duration as short as ~ 100 ps and an emission time as early as 500 ps after the leading edge of the laser pulse. Reaction history for microballoons is usually smooth but often shows an asymmetry of either a slow rise time or a slow fall time. Generally, larger, higher-pressure targets tend to burn later.

In July 1995, burn-history measurements provided the information needed to increase Nova's maximum yield from 2.1×10^{13} to 3.6×10^{13} neutrons. It was observed that neutron emission for large diameter ($>1300\text{ }\mu\text{m}$), thin-walled targets irradiated with 1-ns square pulses was occurring around 1400 ps, well after the laser pulse turned off. By changing to a 1.5-ns pulse with the same power, yield was immediately increased nearly twofold. Figure 3 shows the burn history for several microballoon targets along with the power history of the laser drive.

Our program has devoted significant effort to developing, designing, characterizing, and understanding indirect-drive targets. Fuel capsules for these targets are typically smaller diameter ($360\text{ }\mu\text{m}$) than direct-drive capsules, and are compressed to a higher convergence ratio at a lower temperature. Most indirect-drive capsules use deuterium fuel in a plastic capsule and produce yields between 10^7 and a few 10^9 DD neutrons. Reasonable burn-history measurements can only be made when DD yields are above 10^9 , and signal quality for these low-yield targets depends very strongly on the background signal induced by x-ray emission from the target. Capsules in indirect-drive targets filled with DT fuel produce yields from 10^9 to over 10^{11} . Burn duration for these targets range from 50 to 125 ps. Two examples are shown in Fig. 4. Figure 4(a) is for a high-convergence implosion of a DT-filled glass capsule (from the HEP1 series of

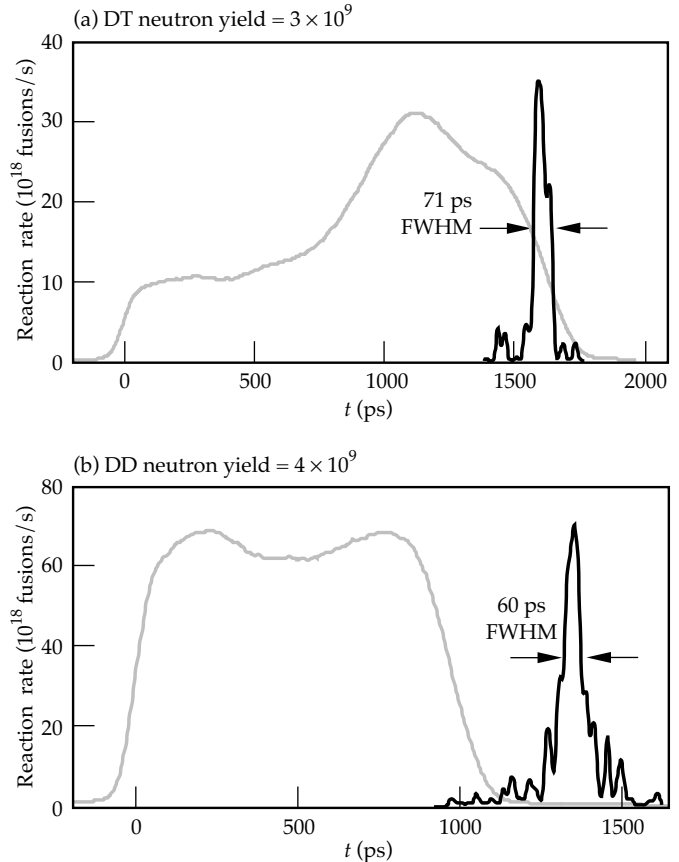


FIGURE 4. Reaction rates for two indirectly driven targets irradiated with $0.351\text{-}\mu\text{m}$ light. The black curves represent the reaction-rate history, the gray curves show the shape of the laser-power history. The type of target and its inner/outer diameters, fill pressure, and incident laser energy for each experiment are (a) glass capsule with CH layer, $180\text{ }\mu\text{m}/240\text{ }\mu\text{m}$, 100 atm DT fuel, 25 kJ, and (b) plastic ball with CH layer, $430\text{ }\mu\text{m}/520\text{ }\mu\text{m}$, 50 atm DD fuel, 27 kJ. (08-00-0896-1855pb02)

experiments)^{12,13}; Fig. 4(b) is for an implosion of a DD-filled, Br-doped plastic capsule (from the HEP4 series of experiments)¹⁴. The reaction rate for the HEP4 capsule approaches the 50-ps resolution limit for DD neutrons in a 1-mm-thick detector.

Figure 5 shows the burn history for a special target used to resolve a “bang time” calibration issue with another detector used at Nova. The burn-history details differ significantly from the previous examples. The most important target characteristic is the very short time delay between laser irradiation and the start of

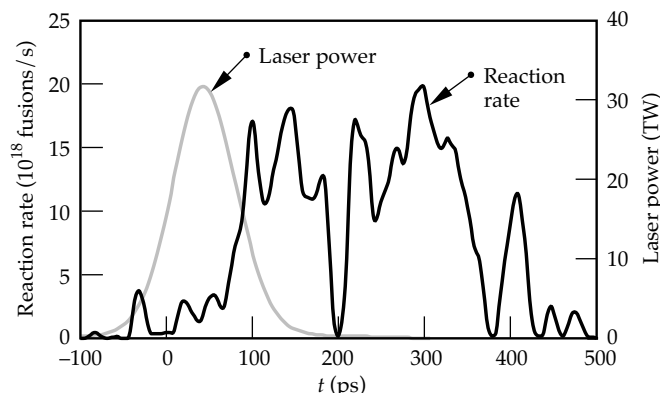


FIGURE 5. Reaction rate for a polystyrene target with a 400- μm -diam hole. There is almost no delay between laser irradiation and the start of neutron emission. (08-00-0896-1856pb01)

neutron emission. Targets were 1-mm-by-2-mm, 320- μm -thick pieces of deuterated polystyrene (C_8D_8), each with a 400- μm hole drilled through it. Tritium was added to the targets by placing them in a tritium gas where tritium atoms replaced deuterium atoms. Targets were irradiated with 2.7 kJ of 0.351- μm laser light delivered in simultaneous 90-ps pulses from each of the ten Nova laser beams. Beams were set at best focus halfway down the inner wall of the hole and evenly spaced at five points around the circumference, one beam from each side of the target focused to each point. DT yields of 5×10^9 neutrons were high enough to produce good burn-history measurements. Low-level neutron emission was observed when the laser pulse reached 50% of its peak power. Significant neutron emission began 70 ps later and lasted ~ 300 ps. The other detector showed neutron emission starting ~ 250 ps earlier, before the start of the laser pulse.

A serious concern for direct-drive ICF implosions is the early time “imprint” of laser-beam nonuniformity that can seed Rayleigh–Taylor instability growth. Los Alamos National Laboratory personnel recently conducted Nova experiments in their investigation of foam buffering as a way to reduce the effect of imprinting.¹⁵ Figure 6 shows burn histories recorded for the three different target configurations irradiated in this study:

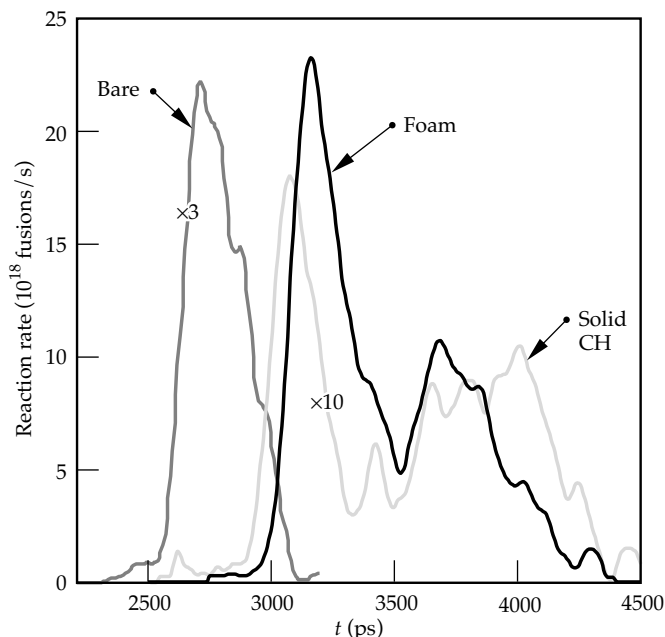


FIGURE 6. Reaction rates for three target types: a “bare” glass microballoon, a CH-foam-coated target, and a solid-CH-covered target. Laser power was delivered at a wavelength of 0.527- μm in 1.5-ns flat-topped pulses. Laser irradiation ends ~ 1.5 ns before fusion begins. The time base is relative to the beginning of the 1.5-ns wide laser pulse. The “bare” and “solid CH” curves have been scaled by factors of three and ten, respectively. (08-00-0896-1857pb01)

- A 1300- μm -diam, “bare” glass microballoon with a 4- μm -thick wall filled with 20 atm of DT fuel.
- Targets coated with a 200- μm -thick layer of 45-mg/ cm^3 polystyrene (CH) foam.
- Targets covered with a 10- μm -thick layer of solid density CH.

Foam-coated targets were irradiated with 0.527- μm light at full Nova energy (34 kJ) delivered in a 1-ns flat-topped pulse. The bare microballoon and solid-CH-covered targets were irradiated at reduced energies of 9 kJ and 21 kJ, respectively, to better match implosion parameters with the foam-coated targets irradiated at 34 kJ. The bare microballoon had a single burn peak 290 ps FWHM. The peak is significantly delayed (~ 1.5 ns) from the peaks of bare microballoons irradiated under standard conditions. This delay is due to the large target diameter and low drive energy. Both the foam and solid-CH-covered targets show a narrow first peak followed by a broader second peak. Calculations suggest the first peak is caused by heating and compression of the first shock reaching target center and the second peak is from DT burn at the time of peak shell compression.

NIF Reaction-Rate Measurements

At the future NIF, fusion reaction rates cannot be measured with 30-ps resolution using the direct neutron-based technique employed at Nova. The target-to-detector spacing required by the NIF exclusion zone will cause

an excessive spreading in the neutron arrival times at the detector. Consider a very conservative example of a detector 1 m from a 4-keV plasma. The detector will see a temperature induced time spread of ~ 240 ps for DT neutrons. Since the plasma temperature and distance will likely be larger than these nominal values, this 240-ps time spread is a lower limit for neutron-based measurements at NIF. It is for this reason that we are investigating the use of gamma rays for making burn-history measurements.^{16,17}

The increased neutron and gamma-ray yields expected for NIF targets should make a gamma-ray-based burn-history measurement possible. Measurements with gamma-rays are attractive because the gamma rays are virtually unaffected by the plasma temperature, have a large interaction cross section in many materials, and have no time dispersion at a distant detector. There are two possible sources of useful gamma rays in ICF experiments. The $T(d,\gamma)^5\text{He}$ fusion reaction produces gamma rays with energies up to 16.7 MeV. The major disadvantage of this reaction is its low branching ratio of 5×10^{-5} . Another possible source of gamma rays is a small converter placed near the target, possibly built as a part of the target, that would convert neutrons to gamma rays through (n,γ) reactions. In this section, one detector concept and the first experimental observation of fusion gamma rays in an ICF experiment are described.¹⁶ Much work remains to develop the sensitive, high-speed gamma-ray detector needed for NIF burn-history measurements.

Gamma-Ray Detector Concept

Figure 7 shows one concept for a gamma-ray-based burn-history measurement. Burning fuel isotropically emits fusion gamma rays, which travel radially outward from the compressed core of an ICF target. Some of the gamma rays interact with a two-stage converter to produce Cerenkov light. In the first converter stage, gamma rays produce forward-directed, relativistic electrons and positrons by Compton scattering and pair production. The charged particles move into a second converter stage, where they produce Cerenkov

light. An optical system collects the Cerenkov light and relays it to a fast optical detector for recording.

Detector design will focus on providing an instrument with good time resolution ($\Delta t < 30$ ps) and sensitivity. The choice of low-Z or high-Z material for the first-stage gamma-ray converter determines whether the primary interaction is Compton scattering or pair production. For 16.7-MeV gamma rays, the interaction cross section for high-Z materials is ~ 100 times greater than it is for low-Z materials. Electron range, however, is much greater in low-Z materials. We estimate that about 15% of 16.7-MeV gamma rays incident on a high-Z converter several millimeters thick will produce electron-positron pairs that enter an adjacent Cerenkov converter.

The second converter stage determines the characteristics of the Cerenkov light. The threshold energy for production of Cerenkov radiation, the cone angle for its emission, and the number of photons emitted per centimeter of track length all depend on the index of refraction n of the converter material. Cerenkov light is produced in a material only when the speed of a charged particle exceeds the speed of light in that media. Thus, Cerenkov light is produced only when a particle's velocity relative to that of light in a vacuum β and n are such that $n\beta > 1$. Cerenkov radiation is emitted into a cone whose half angle θ relative to the direction of charged particle motion is given by $\cos\theta = (1/n\beta)$. The photon production rate in the visible spectrum (400 to 700 nm) is given by

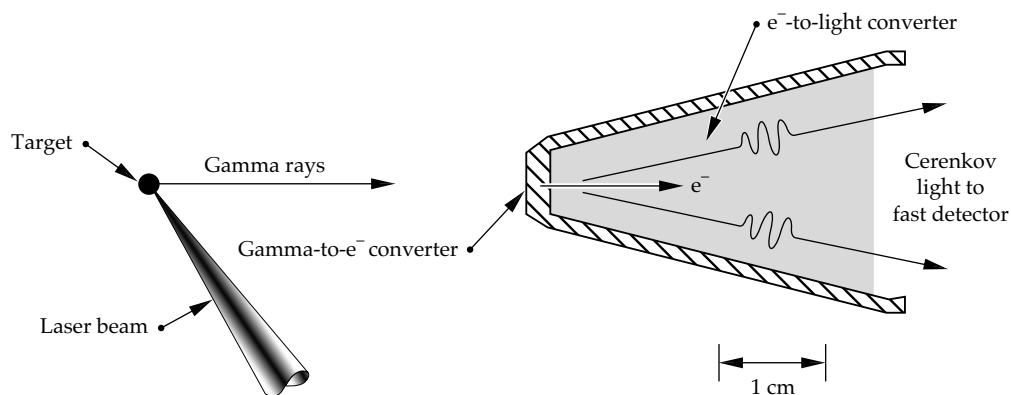
$$\frac{dN}{dx} = 490 \left(1 - \frac{1}{n^2\beta^2} \right) \text{photons/cm}.$$

In Ref. 17, the secondary converter also forms part of the collection optics.

First Observation of Fusion Gamma Rays

We have conducted a set of direct-drive target experiments at Nova to assess our ability to detect fusion gamma rays. Yields from nominally 1-mm-diam DT-filled microballoons irradiated with 1-ns square

FIGURE 7. Cerenkov detector concept. A high-Z material converts target gamma rays to relativistic electrons and positrons that pass into a second converter stage. Since the charged particles are traveling faster than the speed of light in the second converter, Cerenkov light is produced. (08-00-0896-1858pb01)



pulses ranged from 10^{12} to 2×10^{13} neutrons. For these experiments, we adapted equipment normally used for our neutron burn-history measurements. The Hevimet (90% tungsten) nose cone (Fig. 1) acted as the first converter stage in which gamma rays interact primarily by pair production to produce electron-positron pairs. A 0.241-g/cm^3 silica aerogel filled the interior of the nose cone replacing the 1-mm-thick plastic scintillator and Pb glass. The aerogel acted as the second converter stage, converting relativistic electron energy into Cerenkov light. The aerogel, with $n = 1.06$, requires an electron energy >1.03 MeV to produce Cerenkov light. In our experiments, the high threshold level makes the detector relatively insensitive to target x rays and gamma rays from (n,γ) reactions near the target. A shallow cone angle of 19° allows some of the Cerenkov light to be collected by the $f/2$ optic and relayed to the streak camera. We estimate photon production at the rate of 53 photons per centimeter of track length. No modifications were made to the NTD optics to optimize collection of the Cerenkov light. Indeed, the optics, which were designed to pass scintillator light between 350 and 450 nm, have very poor transmission for Cerenkov light below 350 nm.

We observed weak gamma-ray signals in a set of target experiments with target-to-aerogel distances of 2, 3, and 4 cm (see Fig. 8). The signal for each experiment has a low-level gamma-ray pulse followed by a large 550-ps-wide pulse produced by 14-MeV target neutrons interacting with the 75-mm-diam $f/2$ optic of the telescope. The burn duration for these targets is nominally 200 ps FWHM. The neutron pulse width corresponds to the neutron transit time across the four-element optic ~ 2.5 cm behind the aerogel converter. The neutron

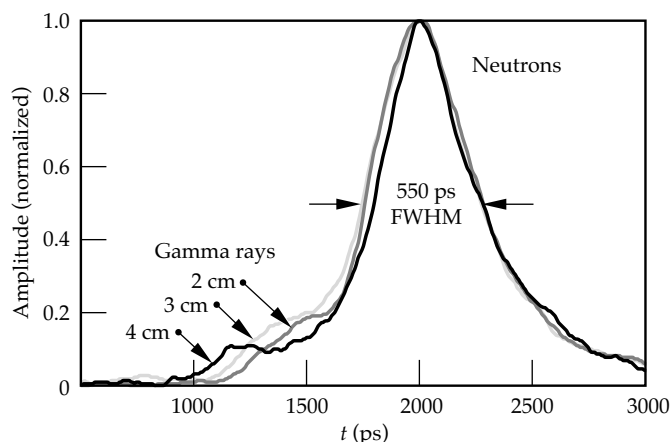


FIGURE 8. Aerogel signal intensity vs time for target-to-aerogel distances of 2, 3, and 4 cm. Neutron-induced signals from the first elements of the imaging optics are normalized, temporally aligned, and overlaid. Presented in this fashion, changes in the timing of the smaller gamma-ray signal relative to the neutron signal are easily observed. Time base is relative to incident laser power for the 4-cm gamma-ray data. (08-00-0896-1859pb01)

signal amplitudes are normalized, temporally aligned, and overlaid. This allows us to easily observe the evolution of a small pulse to the left of the neutron peak. Its time relative to the neutron pulse changes with target-to-aerogel distance in a manner consistent with fusion gamma rays. Because the optic moves with the aerogel, a 1-cm increase in target-to-aerogel distance produces a 162-ps increase in the time separation between gamma-ray- and neutron-induced signals.

The streak camera simultaneously recorded a fiducial signal along with the aerogel signal. This allows us to determine the time of a gamma-ray signal relative to the laser power incident on a target. The time of the gamma-ray signal corresponds to the neutron emission time that we measure with a separate bang-time detector. For these targets, the nominal neutron emission time is at ~ 1 ns.

An additional experiment was performed with an aluminum nose cone replacing the Hevimet nose cone. In this configuration, the pair production cross section for 16.7-MeV gamma rays is reduced by a factor of 25 and the primary interaction mechanism changes to Compton scattering. The result (see Figure 9) is consistent with

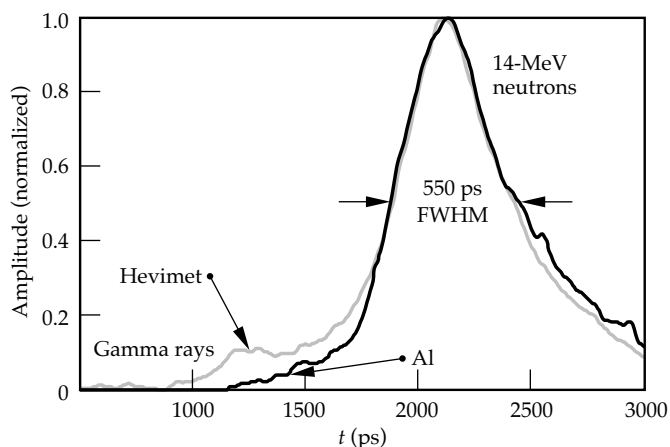


FIGURE 9. Aerogel signal intensity vs time for Hevimet and Al nose cones. The gamma-ray signal depends on high-Z converter material. (08-00-0896-1860pb01)

the small peak being caused by pair production in the high-Z nose cone. The gamma-ray signal observed with the Hevimet nose cone is not observed with the aerogel inside an aluminum nose cone. Also, with the substantially reduced shielding of the aluminum nose cone, there is no x-ray signal observed between the start of target irradiation and bang time, indicating a very low sensitivity to target x rays.

We believe these experiments are the first to detect fusion gamma rays emitted by $T(d,\gamma)^5\text{He}$ reactions in ICF targets. The experimental evidence is consistent with this conclusion. First the change in time-of-flight

separation between gamma-ray and neutron pulses is consistent with the target-to-aerogel distances used. Second, the gamma-ray signals occur at the bang time of the target as determined with a separate neutron detector. Finally, the gamma-ray signal depends on the material used for the first converter stage in a manner consistent with pair production. The reduced shielding of the aluminum nose cone resulted in a decrease rather than an increase in the gamma-ray signal, indicating that the aerogel is a good threshold detector and that we are not detecting lower energy target x rays and gamma rays.

Conclusion

A neutron-based technique and a fast, sensitive neutron detector have been developed for measuring the fusion reaction rate of ICF targets. An absolute timing of ± 20 ps and a temporal resolution of 30 ps have been achieved. Fusion reaction rates have been recorded for a variety of targets irradiated at the Nova Laser Facility. Target yields have ranged from 10^8 to 3.6×10^{13} DT neutrons.

Effort is now being directed towards developing a fast, sensitive burn-history detector based on fusion gamma rays. With a modification to our neutron detector, we have observed fusion gamma rays emitted from Nova high-yield targets, a significant first step in the development of a gamma-ray-based measurement. To obtain a temporal response < 30 ps, we imagine the recording device of our final detector will remain a streak camera. Improved optical transmission of the second converter stage and imaging optics should enhance the signal by about a hundredfold. Based on the initial aerogel experiments, we predict a gamma-ray-based burn history can be made with a 25-cm-diam detector at the wall of the NIF chamber (5 m) when DT neutron yields are above $\sim 10^{13}$.

Acknowledgments

The following people contributed to the successful development of the fast neutron detector system: D. Phillion, G. Tietbohl, R. Ellis, J. Waldrep, J. Wass, G. Mant, R. Griffith, J. Hatch, J. Prior, N. Selchow, and D. Kumpf. The bang-time experiment with the deuterated polystyrene targets was designed and executed by T. Murphy. The initial gamma-ray experiments were done in collaboration with P. Dendooven. We also want to acknowledge S. Thomas for the development of the LLNL optical streak camera that made this work possible.

Notes and References

1. J. D. Lindl, R. L. McCrory, and E. M. Campbell, *Phys. Today* **45**, pp. 32–40 (1992); J. D. Lindl, *Phys. Plasmas* **2** (11), (1995).
2. R. A. Lerche, D. W. Phillion, and G. L. Tietbohl, *Rev. Sci. Instrum.* **66**(1), pp. 933–935 (1995).
3. H. Brysk, *Plasma Phys.* **15**, pp. 611–617 (1973).
4. F. E. Cecil and F. J. Wilkinson, III, *Phys. Rev. Lett.* **53**, pp. 767–770 (1984).
5. J. Kammeraad, J. Hall, K. E. Sale, C. A. Barnes, S. E. Kellogg, and T. R. Wang, *Phys. Rev. C* **47**(1), pp. 29–35, (1993).
6. D. R. Kania, S. M. Lane, and S. G. Prussin, *Appl. Phys. Lett.* **53** (20), pp. 1988–1989 (1988).
7. Bicorn Corp., Newbury, OH.
8. W. R. Graves, D. R. Slaughter, and R. A. Lerche, *Laser Program Annual Report 84*, pp. 5–64–5–65, Lawrence Livermore National Laboratory, Livermore, CA, UCRL-50021-84 (1985).
9. R. A. Lerche and D. W. Phillion, *Conference Record of the 1991 IEEE Nuclear Science Symposium and Medical Imaging Conference*, Vol. I, pp. 167–170, (IEEE, Piscataway, NJ, 91CH3100-5 1991).
10. R. A. Lerche and R. L. Griffith, "Resolution Limitations and Optimization of LLNL Streak Camera Focus," in *High-Speed Photography, Videography, and Photonics V*, H. C. Johnson, Ed., (SPIE—International Society for Optical Engineering, Bellingham, WA, 1988; *Proc. SPIE* **832**), pp. 266–274.
11. R. A. Lerche, "Timing Between Streak Cameras with a Precision of 10 ps," in *Ultra-high- and High-Speed Photography, Videography, Photonics, and Velocimetry '90: Eighth in a Series*, L. L. Shaw, P. A. Jaanimagi, B. T. Neyer, Eds. (SPIE—International Society for Optical Engineering, Bellingham, WA, 1990; *Proc. SPIE*, **1346**) pp. 376–383.
12. M. D. Cable et al., *Phys. Rev. Lett.* **73**, pp. 2316–2319, (1994).
13. S. P. Hatch et al., *ICF Quarterly Report* **5**(4), pp. 226–231, Lawrence Livermore National Laboratory, Livermore, CA, UCRL-LR-105821-95-4.
14. O. L. Landen et al., *ICF Quarterly Report* **5**(4), pp. 271–280, Lawrence Livermore National Laboratory, Livermore, CA, UCRL-LR-105821-95-4.
15. R. G. Watt et al., "Foam-Buffered Spherical Implosions at 527 nm," submitted for publication in *Phys. Plasmas*.
16. R. A. Lerche, "ICF Burn-History Measurements Using 17-MeV Fusion Gamma Rays," *12th International Conference on Laser Interaction and Related Plasma Phenomena, AIP Conference Proceedings* **369** Part 1, pp. 527–532 (1995).
17. K. P. Lewis, M. J. Moran, J. Hall, and M. Graser, *Rev. Sci. Instrum.* **63**(3), pp. 1988–1990 (1992).

MEASUREMENTS OF LASER-SPECKLE-INDUCED PERTURBATIONS IN LASER-DRIVEN FOILS

S. G. Glendinning

*M. H. Key**

B. A. Remington

S. N. Dixit

J. D. Kilkenny

R. J. Wallace

B. A. Hammel

*J. P. Knauer***

S. V. Weber

D. H. Kalantar

D. M. Pennington

Introduction

Growth of modulations in an inertial confinement fusion (ICF) capsule, whether initially due to capsule surface finish or drive nonuniformity, may fatally disrupt an ICF implosion by causing cold shell material to mix into the fuel.^{1,2} When a capsule is driven by x rays produced inside a hohlraum, the dominant modulations are seeded by the capsule surface finish. When laser light directly drives the capsule, the modulations in the driver may be significant. Recent experiments^{3,4} have reported reductions in imprint using smoothed laser beams, i.e., laser beams that have a reduced level of spatial nonuniformities. Another technique for reducing imprint has been the use of foams and gold layers.^{5,6} In this article, we report measurements that quantified the equivalence between laser-imprinted modulations and surface perturbation.

Experimental Description

In our experiment, we used laser ablation to accelerate 20- μm -thick CH_2 foils with one arm of the Nova laser at 0.53- μm wavelength. This arm was smoothed with a random phase plate (RPP)⁷ and spectral dispersion⁸ (SSD), for three different bandwidths in separate experiments: 0.003 THz (the intrinsic bandwidth, introduced by the pulse-shaping system), 0.6 THz, and 0.9 THz. A diffraction grating gave 0.086- $\mu\text{rad}/\text{THz}$ dispersion and a temporal skew of 110 ps to the pulse front (that is, one side arrived earlier than the other). The beam was split into nine segments, each independently steered in space with a glass wedge to form a flat-topped intensity distribution. We measured the

time-integrated laser modulation level from an equivalent target-plane image of the beam. The drive pulse was a linear 1-ns ramp to about $10^{14} \text{ W}/\text{cm}^2$, held constant at this level for 2 ns.

The shock reached the back surface of the 20- μm -thick foil at about 0.7 ns after the start of the laser pulse. The foil then accelerated at about $50 \mu\text{m}/\text{ns}^2$, allowing for 2 ns of constant acceleration to study Rayleigh–Taylor (RT) growth. We measured the areal-density modulations on the foils by conventional x-ray backlighting. We used a gated pinhole camera with 8- μm and 100-ps resolution,⁹ which provided up to 12 frames per shot with arbitrary time spacing. The x-ray back-lighter¹⁰ was a uranium disk illuminated by a second 0.53- μm -wavelength Nova beam (smoothed with an RPP) at about $10^{15} \text{ W}/\text{cm}^2$, giving a broad spectrum peaked at $\sim 1 \text{ keV}$.

Simulations

To examine the predicted evolution of imprinted modes compared to surface modes, we used the two-dimensional code LASNEX¹¹ to separately predict the evolution of a surface single mode and of an imprinted single mode (produced by modulating the incident laser intensity) under the same drive conditions. The LASNEX results showed that the evolution of a laser-imprinted single mode parallels that of a surface single mode after the shock reaches the back surface t_s (see Fig. 1). This suggested that, for our conditions, the laser imprint could be calibrated to an equivalent surface finish. We also used the simulations to estimate the correspondence of a spatial amplitude η with a measured modulation in optical depth $\Delta\tau$, finding that $\eta/\Delta\tau = 10 \mu\text{m}/\tau$ after t_s . This allowed us to make use of the Haan criterion¹² to establish the onset of multi-mode nonlinear saturation. We restricted our analysis to data that were estimated to be in the linear regime.

* Rutherford Appleton Laboratory and University of Oxford, United Kingdom.

** Laboratory for Laser Energetics, Rochester, New York.

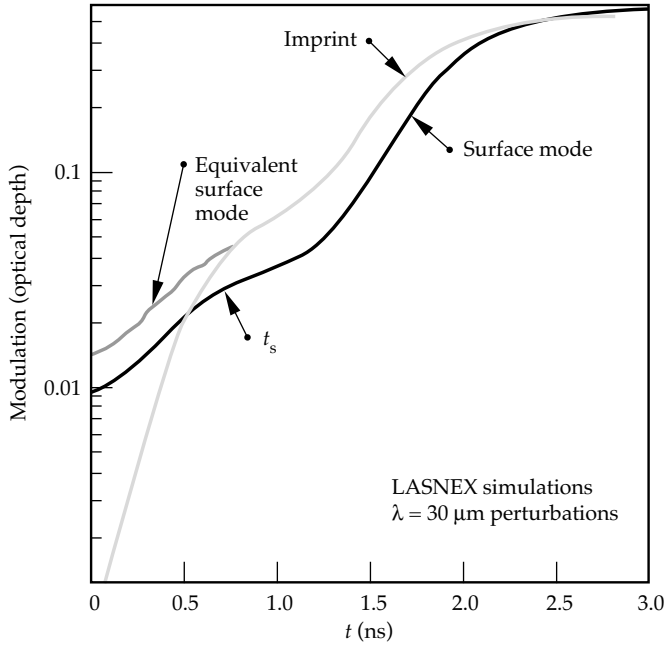


FIGURE 1. LASNEX simulation of optical-depth modulation vs time for a single surface mode and a single imprinted mode of the same wavelength ($30\ \mu\text{m}$). The growth rate between t_s (0.7 ns) and the onset of saturation at $\Delta\tau = 0.3$ is $2.2\ \text{ns}^{-1}$ for the imprinted mode and $2.5\ \text{ns}^{-1}$ for the surface mode. While the imprint begins at zero modulation, an equivalent surface mode would begin at 0.02. (20-03-0796-1564pb01)

We analyzed each frame by converting the film density to exposure; removing the long-scale-length backlighter shape; filtering out noise with a parametric Wiener filter; converting to the natural logarithm of exposure; and taking the two-dimensional power spectrum of the result. A typical image of $\ln(\text{exposure})$ is shown in Fig. 2(a). A vertical profile, which is the horizontal

average of the image, is shown in Fig. 2(b). The surface mode in this case was $\lambda = 30\ \mu\text{m}$ (mode 10, initial amplitude $\eta_0 = 0.25\ \mu\text{m}$) with the modulation vector \mathbf{k} vertical in the image, and the bandwidth was 0.9 THz. We removed the contribution of the surface mode by using a notch filter at the point in Fourier space where the surface mode appears. The same image with the surface mode removed is shown in Fig. 2(c) and its corresponding horizontal average is the dark gray line in Fig. 2(b). Figures 3(a) and 3(b) show the radial power spectra (azimuthal integrals of the two-dimensional power spectra) for this shot at three different times, the noise power spectrum (measured on a separate shot with an undriven foil), and the instrument modulation transfer function (MTF). The laser imprint was almost indistinguishable from the noise for the higher bandwidths at t_s (not shown), but subsequent growth gave clearly measurable modulations at later times. Figures 4(a) and 4(b) show the time-integrated power spectra of the laser speckle and the imprinted spectra at $t = 1.5\ \text{ns}$ as measured for the different bandwidths. As is characteristic with SSD, while there was smoothing at all modes, the higher modes were smoothed preferentially.

To test the LASNEX prediction that the evolution of a laser-imprinted mode parallels the surface mode after t_s , we examined the growth for several shots. Figure 5 shows the results for the shot of Figs. 2 and 3. The modulation amplitudes for the surface mode ($\lambda = 30\ \mu\text{m}$), for the imprinted spectrum at mode 10, and for the root-mean-square (rms) of the $\ln(\text{exposure})$ are shown as a function of time after the start of the laser pulse. We subtracted in quadrature the noise component due to the instrument and backlighter from the values for the imprint modes. The

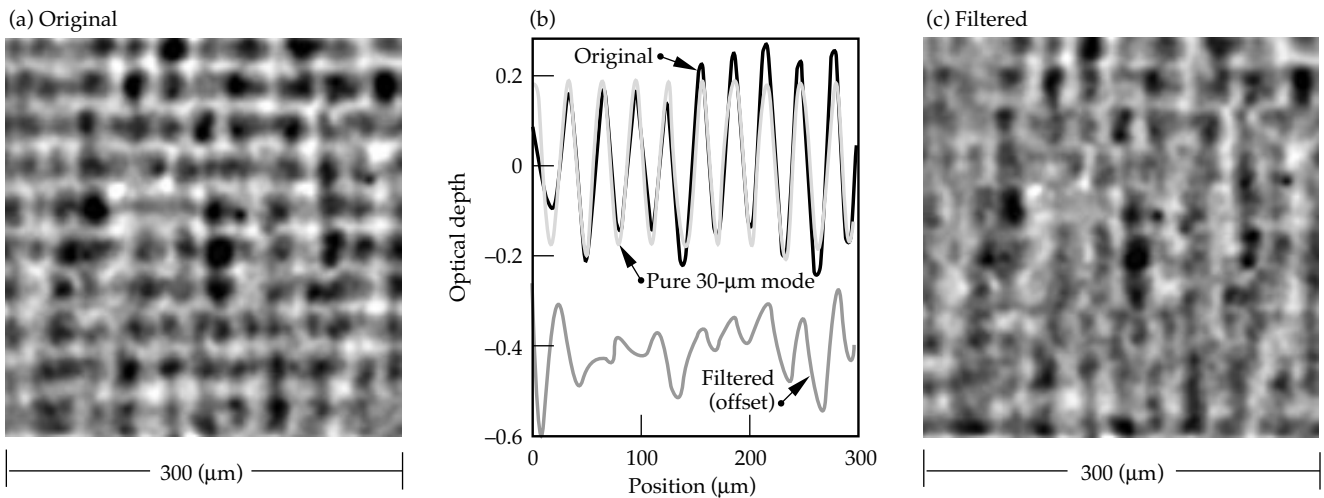


FIGURE 2. A single image from a framing camera radiograph at $t = 1.9\ \text{ns}$ (1.2 ns after t_s), shown in $\ln(\text{exposure})$. (a) is the original image, with a $\lambda = 30\ \mu\text{m}$, $\eta_0 = 0.25\ \mu\text{m}$ surface mode. The vertical profiles in (b) are made by horizontally averaging the images. In (b), the black curve is from (a) and the light gray curve is a pure $30\text{-}\mu\text{m}$ mode with $\Delta\tau = 0.2$ (optical depth), while the dark gray curve corresponds to (c). (c) has been digitally filtered to remove the $\lambda = 30\ \mu\text{m}$ mode in the vertical direction only. (20-03-0796-1565pb01)

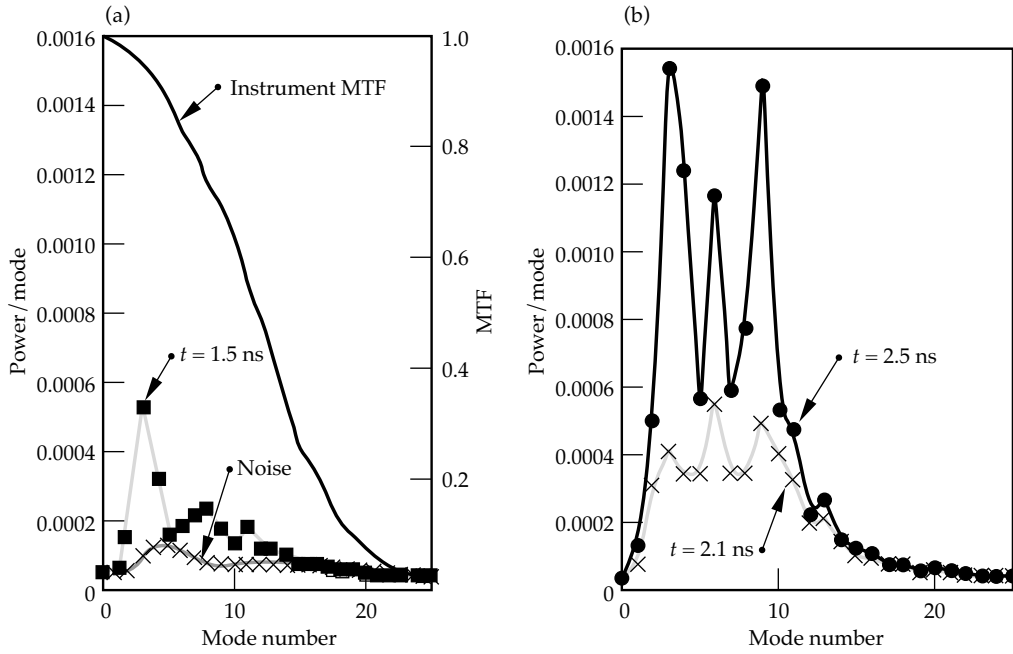


FIGURE 3. Azimuthally integrated radial profiles at three different times of the two-dimensional Fourier power spectra for the shot shown in Fig. 2. Also shown are the instrument noise (measured on a shot with an undriven foil) and the modulation transfer function (MTF) of the measurement system. The MTF uses the right axis. (20-03-0796-1566pb01)

two $\lambda = 30 \mu\text{m}$ modes from surface and imprint modulations grew at the same rate ($0.9 \pm 0.2 \text{ ns}^{-1}$). The rms grew at nearly the same rate ($0.8 \pm 0.2 \text{ ns}^{-1}$), suggesting that the growth rates for the dominant modes were similar.

At a given time in the linear regime, the ratio of the rms to the surface mode times the initial surface-mode amplitude gave the equivalent surface finish in microns at $t = 0$. The inferred rms surface finish was insensitive to the calibration wavelength we used,

suggesting little variation in growth rate for the dominant wavelengths. We calculated the equivalent surface finish to be $0.26 \pm 0.07 \mu\text{m}$ with 0.9 THz of bandwidth on the drive laser, $0.51 \pm 0.24 \mu\text{m}$ with 0.6 THz bandwidth, and $1.24 \pm 0.27 \mu\text{m}$ with minimum bandwidth. Figure 6 shows these results vs bandwidth, along with the time-integrated rms modulation in the laser speckle. The imprinted-modulation rms appeared to decrease only about half as fast as the laser modulation as a function of bandwidth.

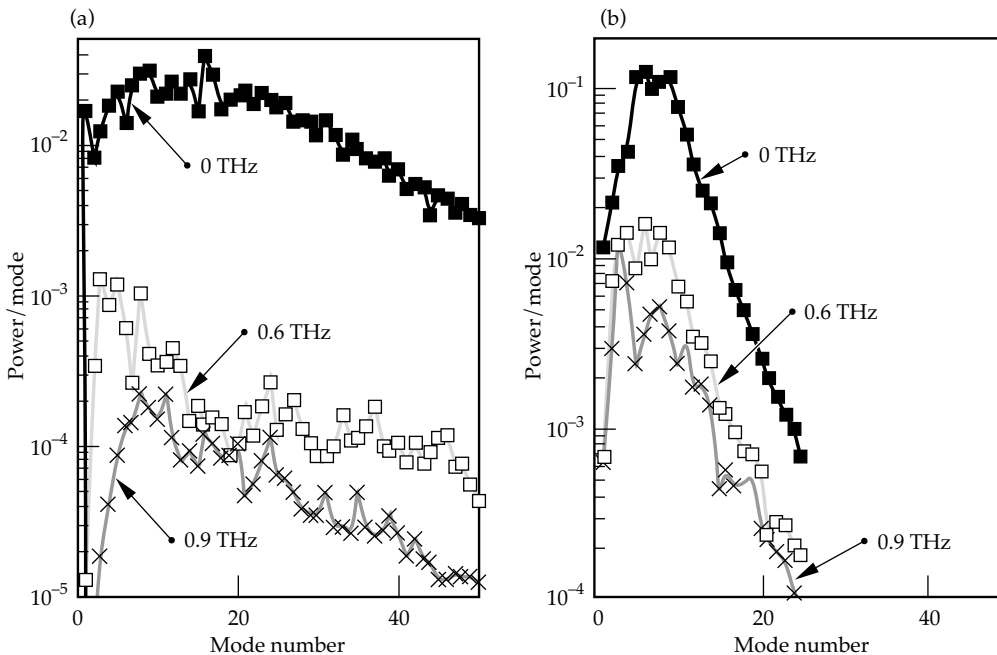


FIGURE 4. Power spectra of (a) the laser spots and (b) the imprinted modulation, converted to initial surface amplitudes, for the three bandwidths. (20-03-0796-1567pb01)

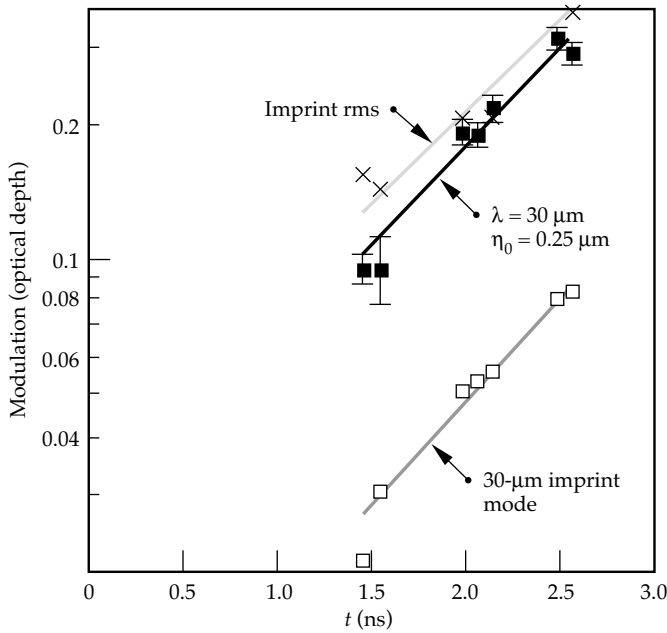


FIGURE 5. Modulation amplitudes for the shot shown in Figs. 2 and 3 vs t . The surface mode (shown with characteristic error bars), the imprinted mode at the same wavelength, and the rms grow at the same rate. (20-03-0796-1568pb01)

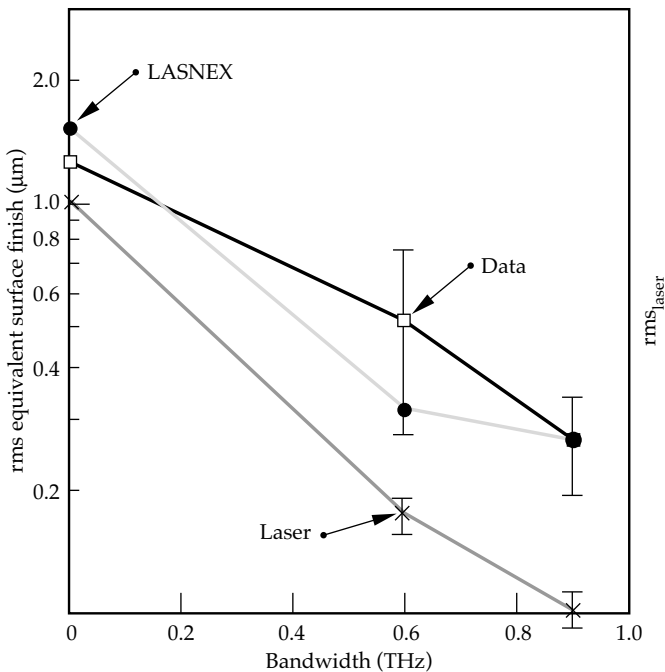


FIGURE 6. Equivalent surface finish for three bandwidths, as measured and simulated. The measured time-integrated laser-rms modulation vs bandwidth is also shown. The lines are a guide to the eye. (20-03-0796-1569pb01)

We used LASNEX to simulate the equivalent surface finish due to the laser imprinted modulations. The single-surface-mode simulation was done separately from the laser-imprint simulation. Since LASNEX is a two-dimensional code, the laser speckle

is represented by a one-dimensional slice of the predicted laser-modulation pattern. With minimum bandwidth, the speckle is isotropic and the direction of the slice is not important. When SSD was added to the simulation, we used two directions—parallel and perpendicular to the direction of dispersion—and averaged the resulting predictions. The simulations propagated the measured backlighter spectrum through the simulated package and convolved the result with the instrument response function. The results are also shown on Fig. 6.

Conclusions

The predictions agreed with the experimental results. In particular, the predicted imprinted modulations did not decrease as rapidly with bandwidth as the time-integrated laser modulation. This effect has also been observed in experiments using a different measurement technique.^{13,14} One possible explanation is the thermal smoothing of the drive modulations in the region between the laser light deposition and the ablation surface. In this region, the energy is propagated by electron thermal conduction and nonuniformities are smoothed inversely with the spatial scale of the nonuniformity. Thus, the minimum-bandwidth case showed more thermal smoothing because more of the laser modulation is at smaller spatial scales. If we calculate the laser time-integrated smoothing level including only lower modes (spatial structure $> 30 \mu\text{m}$), the rate of decrease of target imprint and the laser time-integrated smoothing level with increased bandwidth is the same. This suggests that the thermal smoothing for this experiment is most effective for modes with $\lambda < \sim 30 \mu\text{m}$. Unfortunately, the instrument response greatly affects our ability to measure spatial structures less than $30 \mu\text{m}$. While the LASNEX simulations predict that such structures are not present in the imprinted modulations, we cannot confirm this with the available data.

Summary

In summary, we have observed modulations due to laser speckle and we have shown that for a modest (less than a factor of three) amount of Rayleigh–Taylor growth, the speckle-imprinted modes grow at the same rate as a pre-imposed single-mode surface perturbation. We used this relationship to characterize the observed imprinted-rms modulation in optical depth as an equivalent surface finish for different bandwidths. The imprinted-foil modulations decreased with increasing bandwidth but not as rapidly as the time-integrated laser modulations, which is in agreement with numerical simulations. We suggest that this decrease is due to the additional smoothing of high spatial frequencies between the laser deposition region and the ablation surface.

Notes and References

1. J. Nuckolls, L. Wood, A. Thiessen, and G. Zimmerman, *Nature* **239**(5368), pp. 139–142 (1972).
2. M. M. Marinak, R. E. Tipton, O. L. Landen, T. J. Murphy et al., *Phys. Plasmas* **3** (5), pp. 2070–2075, (1996).
3. D. K. Bradley, J. A. Dellettrez, and C. P. Verdon, *Phys. Rev. Lett.* **68** (18), pp. 2774–1777 (1992).
4. J. D. Kilkenney, S. G. Glendinning, S. W. Haan, B. A. Hammel et al., *Phys. Plasmas* **1** (5), pp. 1379–1389 (1994).
5. M. Desselberger, T. Afshar-rad, F. Khattak, S. Viana et al., *Phys. Rev. Lett.* **68** (10), pp. 1539–1542 (1992).
6. R. J. Taylor, J. P. Dahlburg, A. Iwase, J. H. Gardner et al., *Phys. Rev. Lett.* **76** (10), pp. 1643–1646 (1996).
7. S. N. Dixit, I. M. Thomas, B. W. Woods, A. J. Morgan et al., *Appl. Optics* **32** (14), pp. 2543–2554 (1993).
8. S. Skupsky, R. W. Short, T. Kessler, R. S. Craxton, S. Letzring, and J. M. Soures, *J. Appl. Phys.* **66** (8), pp. 3456–3462 (1989).
9. O. L. Landen, P. M. Bell, J. A. Oertel, J. J. Satariano, and D. K. Bradley, *Ultrahigh- and High-Speed Photography, Videography, and Photonics '93* (SPIE—The International Society for Optical Engineering, Bellingham, WA, 1993; *Proc. SPIE* **2002**), pp. 2–13.
10. S. G. Glendinning, P. Amendt, K. S. Budil, B. A. Hammel et al., *Applications of Laser Plasma Radiation II* (SPIE—The International Society for Optical Engineering, Bellingham, WA, 1995; *Proc. SPIE* **2523**), pp. 29–39.
11. G. B. Zimmerman and W. L. Kruer, *Comments Plasma Phys. Controlled Fusion* **2** (2), pp. 51–61 (1975).
12. S. W. Haan, *Phys. Rev. A* **39** (11), pp. 5812–5825 (1989).
13. D. H. Kalantar, M. H. Key, L. B. Da Silva, S. G. Glendinning et al., *Phys. Rev. Lett.* **76** (19), pp. 3574–3577 (1996).
14. M. H. Key, *XUV Lasers and Applications* (SPIE—The International Society for Optical Engineering, Bellingham, WA, 1995; *Proc. SPIE* **2520**), pp. 279–86.

NOVA/BEAMLET/NIF UPDATES

APRIL-JUNE 1996

G. Hermes/R. Speck/A. Clobes

Nova Operations

During this quarter, Nova Operations fired a total of 274 system shots resulting in 288 experiments. These experiments were distributed among ICF experiments, Defense Sciences experiments, X-Ray Laser experiments, Laser Sciences, and facility maintenance shots.

As a result of gradual budget reductions over the past several years, the number of Nova Operations staff has been slowly reduced to the point that a standard double-shift operation is no longer able to be supported. In an attempt to improve facility performance, the Nova Operations group formed a team to evaluate the use of an alternate work schedule for system operations. The previous schedule consisted of two standard eight-hour shifts overlapping by one hour, five days per week. The team reviewed a variety of work schedules to determine which schedule would best meet criteria provided by the Program. As a result of their study, the team recommended four ten-hour days per week of two shifts overlapping by three hours. This alternate schedule provides slightly more time for experiments, while leaving adequate maintenance time and without requiring the use of regularly scheduled overtime. As of June 10, the operations personnel have been working this new shift. Preliminary evaluation of this work schedule indicates that the system shot rate is very near that of the standard two-shift operation and that system maintenance has improved.

A final design review was presented by Los Alamos National Laboratory for phase 2 of the Full Aperture Backscatter Station (FABS II). This diagnostic incorporates a reflecting telescope to produce a high-resolution image of the target plane. Subsequent to the review, LANL determined that the primary turning mirror produced a second surface reflection that resulted in unacceptable interference with the signal from the first

surface. An alternate mirror will be coated with a wide-band, high-reflective coating on the first surface to eliminate this issue. The installation schedule for FABS II will be reevaluated after the coating of this mirror.

The Gated X-Ray Imager #5 (GXI 5), modified last quarter to use a charge-coupled-device (CCD) camera readout, is still undergoing development. During initial activation, several problems were noted and repaired. We are continuing to use this camera as opportunities arise to complete testing and work out any additional issues. The use of a CCD camera allows immediate viewing of data following a system shot.

In ongoing support of the Petawatt Project, we completed the following:

- Installation and activation of the compressor vacuum system.
- Installation and alignment of a subaperture beam-diagnostic station to support the May shot series.
- Demonstration of subaperture pulse compression in a vacuum by achieving 1.25 PW during the May shots.
- Continued system installation and activation in preparation for the full-aperture Petawatt demonstration.

We are developing a plan to install a minichamber between the Petawatt compressor and the ten-beam target chamber. This minichamber will be used during the initial Petawatt demonstration to measure system performance and beam spot at focus. The detailed engineering continues for the parabolic mirror mount, target alignment viewer, and miscellaneous diagnostic hardware required to support target experiments with the Petawatt system.

We are removing the one-beam chamber located in the west end of the two-beam area to provide a lab area for the testing of the NIF final optics assembly. Other assembly processes and hardware stored in this area are also being relocated.

Beamlet

Beamlet continues to provide the testbed to validate the laser physics foundations of the National Ignition Facility (NIF) and to check laser engineering concepts and components proposed for the NIF. During the quarter, activities on Beamlet included the following:

- We quantified the limits on power output of the NIF 1.06- μm laser design that are safe from beam filamentation in the system's 1 ω optics.
- We obtained far-field images in the new dark-field-imaging diagnostic that quantified the fraction of the 1 ω power scattered at small angle as a function of laser output power.
- We installed reworked 37-cm aperture frequency-conversion crystals.
- We upgraded the 3 ω focal-plane diagnostic system.
- We began a series of shots to characterize the 3 ω focal spot and assess the damage threat to the final optics components.
- We activated an improved control system for the deformable mirror that will allow correction for gas turbulence.

The shots to study beam filamentation propagated 200-ps-duration pulses through the unpumped booster amplifier to simulate the conditions at the end of long, high-energy, saturating pulses. The short pulses provided a "snapshot" of the most stressful part of the saturating pulse and greatly reduced the irradiance averaging that takes place when a near-field image of the entire pulse is taken. The most important diagnostic in this series was a high-magnification near-field camera recorded by a 1024×1024 -pixel CCD camera. The results confirmed that the NIF can operate safe from filamentation with delta-B values of up to 1.8 and can have adequate margin for beam-to-beam and shot-to-shot fluctuations in output. Smaller pinholes (130 μrad in the cavity spatial filter and 100 μrad in the transport filter) provide added margin over the standard 200- μrad pinholes and are preferable.

Dark-field image data of the 1 ω output were also gathered from 200-ps pulses and an unpumped booster amplifier. Much of the data came from the same shots as the 1 ω near-field modulation data. The diagnostic system measured the fraction of the power scattered outside far-field beam blocks of ± 33 , ± 66 , and ± 100 μrad . The data provides a measurement of (1) power scattered from imperfections and finishing errors on the optics at low laser output power and (2) the growth in this scattered power with increasing laser power. This information is useful in determining noise source values for use in laser propagation modeling.

Beginning in mid-May, we installed refinished 37-cm-aperture frequency-conversion crystals on Beamlet following their characterization on the high-resolution phase matching interferometer. At this time we also aligned and calibrated the Phase II diagnostics for the

3 ω focal-plane diagnostics system. New diagnostics include a very-high-resolution near-field camera that records on photographic film, a medium-resolution near-field camera that records on a CCD array, a wide-field-of-view calorimeter, a 3 ω streak camera, a multiple-plane 3 ω far-field camera, and a number of new and upgraded energy sensors.

Experiments to investigate 3 ω beam quality and focusability began in early June following the calibration of the new diagnostics and the angle tuning of the conversion crystals. We fired a total of 19 shots in this campaign; 14 to measure the 3 ω beam quality and focal spot and 5 to characterize the focal spot obtained with a kinoform phase plate (KPP). Ten of the 14 shots without the KPP were with 200-ps-duration pulses and with the booster amplifiers unpumped to achieve delta-Bs of up to 1.8 rad at power levels up to 2 TW. We investigated both small pinholes (130- μrad cavity / 100- μrad booster) and large pinholes (200- μrad / 200- μrad). The focal spot data at 2.8 TW power with and without a KPP yielded 80% power half angles of 33 μrad and 20 μrad respectively and 95% power half angles of 53 μrad and 32 μrad . Preliminary analysis indicates that the spot size is strongly influenced by thermal effects in the amplifiers, as well as by output power.

At the end of June, we completed the activation of the T₀-1 second wavefront correction system. This system allows the deformable mirror to run in closed loop up to one second before shot time and thus provides the capability for wavefront correction up to the last second before shot time. On a limited number of shots during its activation, the system corrected wavefront error caused by turbulence on shots taken early in the day but was increasingly unable to make the correction as the heat accumulation in the amplifiers and the corresponding turbulence increased after repeated shots, indicating that turbulence cell sizes become smaller than the deformable mirror could correct due to its finite actuator separation.

National Ignition Facility

We made significant progress in Title I design this quarter; based on current accomplishments, the Project is expected to meet all FY 1996 critical-path milestones and complete the design as planned in September (Laser and Target Area Building conventional facility) and October (special equipment and Optical Assembly Building). The Mid-Title I Design Review, completed at the end of May, served as an interim checkpoint in the design process. The status of the mid-Title I design was presented to a review committee consisting of individuals from all the participating Laboratories as well as outside reviewers. The recommendations and comments were documented and assembled into a package and distributed to Project personnel for use in updating the design.

While the three-month total estimated cost (TEC) funding delay slowed NIF staffing and delayed the start of design, a catch-up plan was developed and implemented and is working well. This catch-up is based on a well integrated NIF/ICF team, augmented by effective use of Master Task Agreements (MTAs) with commercial companies, coupled with rapid narrowing of design options.

Engineering documentation and infrastructure are developed to the degree necessary for the current design effort. The Computer Aided Design and Drafting (CADD) systems are fully operational, the Product Data Management (Sherpa) hardware and software are implemented, and the required subsystem design requirements and interface control documents are in place.

In addition and in parallel with the intensive design effort, Title I cost and schedule estimates are being developed in all areas. The system and database are operational, with inputs generated by the responsible engineers and the system and rates controlled by the NIF Project Office. Initial inputs are essentially complete, and verification is under way.

Specific progress in the various areas is outlined below.

- The contract for construction management services was awarded to Sverdrup, and personnel were on-board for the Mid-Title I Design Review. Fast tracking is being considered to meet the construction schedule milestones, and special construction methods are being evaluated.
- The NIF general arrangement drawings for the NIF Laser and Target Area Building (LTAB) have been completed and are under configuration control. Design iterations continue for cost containment and reduction to assure that the design results in the minimum platform to achieve the requirements.
- An embedded laser-amplifier structure that offers important installation and operational advantages over the original conceptual design was developed and is the basis of the Title I design. This approach also simplifies utility interfaces above the amplifiers, which are now an integral part of the structure.
- Following an extensive technical and cost tradeoff evaluation, we selected flexible transmission lines for power conditioning over rigid lines and established a routing layout. Flexible lines result in easier installation and improved accessibility.
- We optimized the preamplifier module/preamplifier beam transport system layout to permit the output sensor packages to be located underneath the transport spatial filter for reduced cost and improved stability and operational accessibility. We completed the preamplifier module maintenance area layout and utility requirements.
- We have successfully resolved numerous conflicting requirements in the beam transport system and have established an end-to-end comprehensive design solution (see Fig. 1). Space allocations have been frozen for all laser bay and switchyard subsystems. Baseline switchyard and laser bay structures, which meet all stability, access and safety requirements, have been established and integrated with the other systems.
- We selected a hybrid concrete-steel construction early in the quarter for use on all the laser bay support structures. Detailed analysis confirmed the performance advantage of the hybrid structure over all-steel or all-concrete structures. The laser support structures have been integrated with all other subsystems.

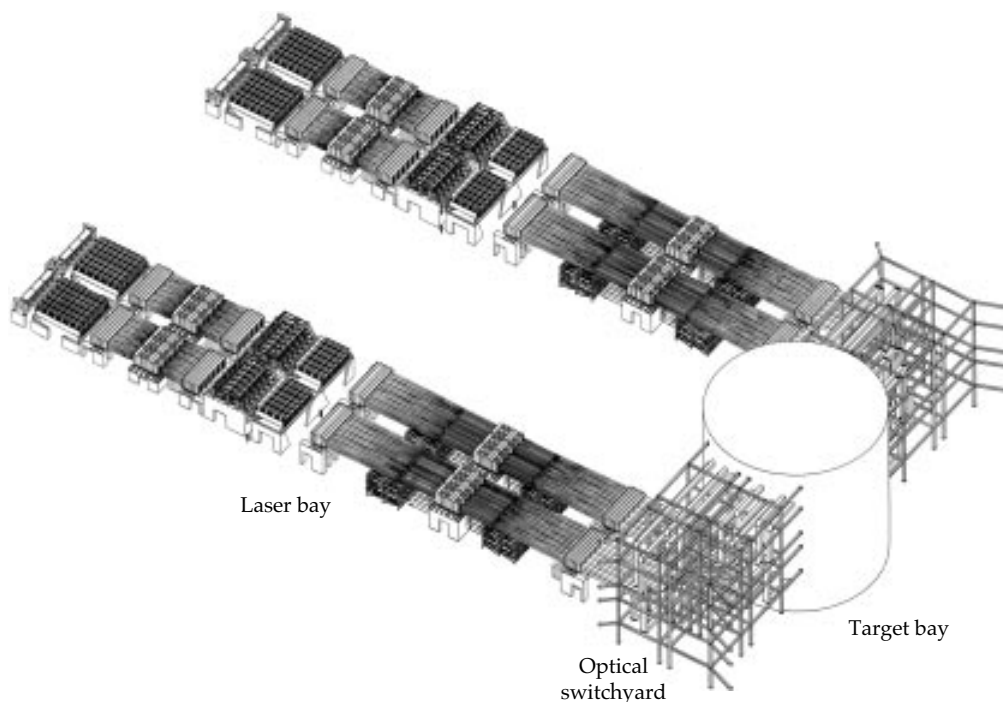


FIGURE 1. A comprehensive "end-to-end" integrated design has been developed. (40-00-0796-1771pb01)

- In collaboration with the ICF Core Science and Technology Program, a NIF prototype automatic-alignment loop, based on analysis of the beam profile and commercial Datacube processing system, was activated and is undergoing tests. CORBA and Ada95 software, which are planned for NIF use, are currently being tested in the front-end processors.
- We established the optical component layout for the main laser system. Title I optics sizes and thickness have been established, component spacing issues resolved, and configuration drawings generated for the laser optical train. We have completed individual system elements of the clear-aperture budget analysis, and integration and consistency checks are in progress.
- We resolved complicated design issues in the transport spatial filter, including optics locations, and paths for injection, alignment, diagnostics, wavefront control, and main beams. The optical stability has been improved by use of top-loading towers separate from the vacuum chamber.
- Major revisions to the target area design were carried out to incorporate the color separation filter in the final optics assembly. The beam transport codes were revised, the building configuration modified, new analytic models of the building developed, and the mirror supports redesigned and presented at the Mid-Title I Design Review.
- The finite-element integrated target-building/switchyard-structures model was refined to reflect the most recent design details (see Fig. 2). We continue to analyze structural/damping supports between the chamber/pedestal and target building floors. We delivered structural drawings of the target room floors, ribs, columns, and associated

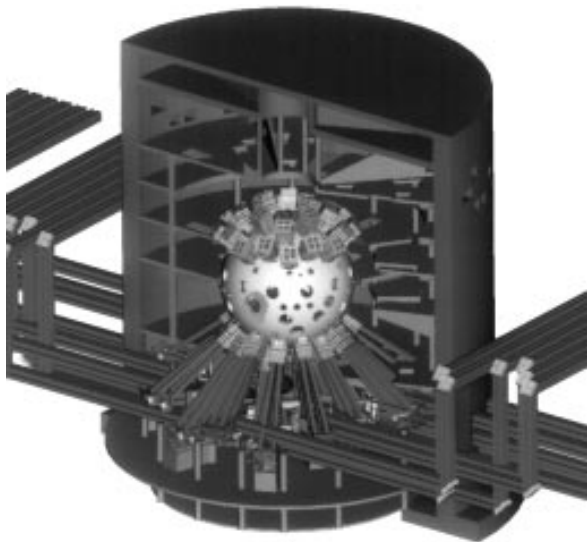
equipment loads to the LTAB Architecture/Engineering firm, Parsons, for their civil and structural analysis. Layouts of the target room floors and special equipment lasers were also delivered so that Parsons could model the area for the thermal analysis.

- Material flow studies have been effective in resolving LTAB corridor, doorway, and elevator size requirements. Development continued on requirements for optics transport and handling, and requirements for top-loading line replaceable units were evaluated.
- The *Final Programmatic Environmental Impact Statement* is complete except for DOE comment resolution. The *Preliminary Safety Analysis Report* was completed as scheduled and submitted to DOE for concurrence review.

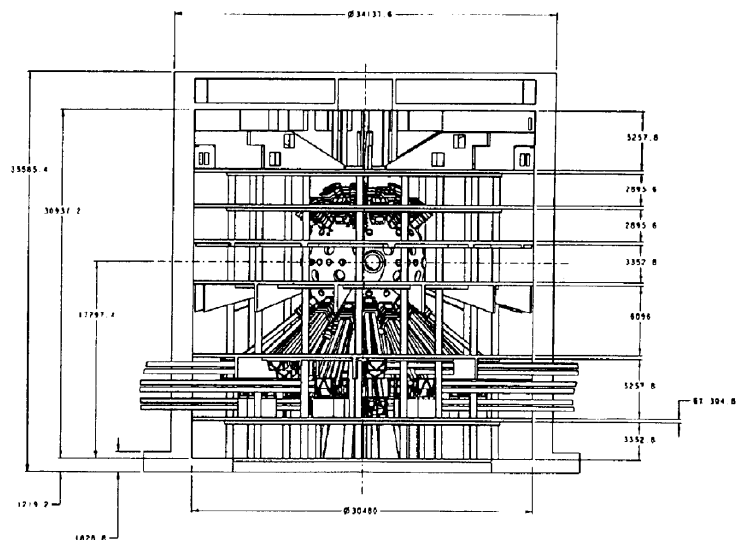
Twelve students from colleges and universities throughout the country, representing a number of technical disciplines, are employed by the NIF Project for the summer supporting the above activities.

Planning for the Title I Design Review is well under way. The Title I Design Review Plan was completed and released to Project personnel for their use in detailed planning of the remaining Title I work. The plan includes the overall objectives, organization, and schedules, as well as the agenda for the review meetings and contents of the Design Basis Books. The overall chairman of the review committee was selected and considerable progress made in identifying review committee members that will include DOE and external reviewers.

During the coming quarter, Title I documentation packages including design, cost, and schedule will be prepared, and the Title I Design Reviews will begin.



3-D CADD model



NIF drawing no. NM96-1.8.1-000044-A

FIGURE 2. Engineering drawings are rapidly emerging from a comprehensive 3-D solid CADD model. (40-00-0796-1633pb01)

PUBLICATIONS

A

Afeyan, B. B., and Chou, A. E., *SOFTSTEP Simulations of Stimulated Raman Scattering in Multidimensional Inhomogeneous Plasmas Driven by Structured Laser Beams*, Lawrence Livermore National Laboratory, Livermore, CA, UCRL-JC-124458 ABS. Prepared for the 26th Annual Anomalous Absorption Conf, Fairbanks, AK, Aug 26–30, 1996.

Afeyan, B. B., Kruer, W. L., and Chou, A. E., *Electron Plasma and Ion Acoustic Waves in Flat Top Electron Velocity Distributions*, Lawrence Livermore National Laboratory, Livermore, CA, UCRL-JC-124459 ABS. Prepared for the 26th Annual Anomalous Absorption Conf, Fairbanks, AK, Aug 26–30, 1996.

Amendt, P., Glendinning, S. G., Hammel, B., Landen, O., and Suter, L. J., *Shocked Witness Foam-Ball Drive Diagnostic at Target Center*, Lawrence Livermore National Laboratory, Livermore, CA, UCRL-JC-124462 ABS. Prepared for the 26th Annual Anomalous Absorption Conf, Fairbanks, AK, Aug 26–30, 1996.

Amendt, P., Glendinning, S. G., Hammel, B., Landen, O., and Suter, L. J., *Evidence of Drive Enhancement in Modified Nova Hohlraums from Backlit Ablatively-Shocked Surrogate Targets*, Lawrence Livermore National Laboratory, Livermore, CA, UCRL-JC-124464. Submitted to *Phys. Rev. Lett.*

Amendt, P., Murphy, T. J., and Hatchett, S. P., *Novel Symmetry Tuning in Nova Hohlraums Using Axial Gold Discs*, Lawrence Livermore National Laboratory, Livermore, CA, UCRL-JC-124292. Submitted to *Phys. of Plasmas*.

Anderson, A. T., Burnham, A. K., Tobin, M. T., and Peterson, P. F., *Modeling and Experiments of X-Ray Ablation of National Ignition Facility First Wall Materials*, Lawrence Livermore National Laboratory, Livermore, CA, UCRL-JC-123553. Prepared for the American Nuclear Society 12th Topical Mtg on the Technology of Fusion Energy, Reno, NV, Jun 16–20, 1996.

Anderson, A. T., Managan, R. A., Tobin, M. T., Peterson, P. F., *X-Ray Emission from National Ignition Facility Indirect Drive Targets*, Lawrence Livermore National Laboratory, Livermore, CA, UCRL-JC-123557. Prepared for the American Nuclear Society 12th Topical Mtg on the Technology of Fusion Energy, Reno, NV, Jun 16–20, 1996.

Auerbach, J. M., Eimerl, D., Milam, D., and Milonni, P. W., *A Perturbation Theory for Electric Field Amplitude and Phase Ripple Transfer in Frequency Doubling and Tripling*, Lawrence Livermore National Laboratory, Livermore, CA, UCRL-JC-124005. Submitted to *Applied Optics: Lasers, Photonics, & Environ. Optics*.

B

Back, C. A., Glenzer, S. H., Lee, R. W., MacGowan, B. J., Moreno, J. C., Nash, J. K., Powers, L. V., and Shepard, T. D., *Spectroscopic Temperature Measurements of Non-Equilibrium Plasmas*, Lawrence Livermore National Laboratory, Livermore, CA, UCRL-JC-123074. Prepared for the 10th American Physical Society Topical Conf on Atomic Processes in Plasmas, San Francisco, CA, Jan 14–18, 1996.

Back, C. A., Glenzer, S. H., Landen, O. L., MacGowan, B. J., and Shepard, T. D., *X-Ray Diagnostics of Hohlraum Plasma Flow*, Lawrence Livermore National Laboratory, Livermore, CA, UCRL-JC-123283. Prepared for the 11th Topical Conf on High Temperature Plasma Diagnostics, Monterey, CA, May 12–16, 1996.

Beach, R. J., *Medical Applications of High Power Laser Diode Arrays*, Lawrence Livermore National Laboratory, Livermore, CA, UCRL-JC-124018 ABS. Prepared for the Optical Society of America Annual Mtg & Exhibit, Rochester, NY, Oct 20–25, 1996.

Berger, R. L., Still, C. H., Hinkel, D. E., Langdon, A. B., Williams, E. A., Kirkwood, R. K., MacGowan, B. J., Montgomery, D. S., and Moody, J. D., *Multi-Dimensional Evolution of Stimulated Scattering and Filamentation*, Lawrence Livermore National Laboratory, Livermore, CA, UCRL-JC-124465 ABS. Prepared for the 26th Annual Anomalous Absorption Conf, Fairbanks, AK, Aug 26–30, 1996.

Bernat, T. P., *Technologies and Prospects for Fabricating NIF Targets*, Lawrence Livermore National Laboratory, Livermore, CA, UCRL-JC-124238 SUM. Prepared for the 16th Intl Atomic Energy Agency Fusion Energy Conf on Plasma Physics and Controlled Nuclear Fusion Research, Montreal, Canada, Oct 7–11, 1996.

Bernat, T. P., *Design and Reality for NIF Ignition Targets*, Lawrence Livermore National Laboratory, Livermore, CA, UCRL-JC-124276. Prepared for the 24th European Conf on Laser Interaction with Matter, Madrid, Spain, Jun 3–7, 1996.

Bibeau, C., and Beach, R., *CW and Q-Switched Performance of a Diode End-Pumped Yb:YAG Laser*, Lawrence Livermore National Laboratory, Livermore, CA, UCRL-JC-124042 ABS & SUM. Prepared for the 1996 Conf on Lasers and Electro-Optics/Quantum Electronics and Laser Science Conf, Anaheim, CA, Jun 2–7, 1996.

Bibeau, C., Beach, R., Honea, E., Page, R., Sutton, S., Emanuel, M., Skidmore, J., and Payne, S., *High Power Diode End-Pumped Yb:YAG and Tm:YAG Laser Systems*, Lawrence Livermore National Laboratory, Livermore, CA, UCRL-JC-123789 ABS. Prepared for the 9th Annual Diode Laser Technology Review, Albuquerque, NM, Apr 15–18, 1996.

Budil, K., Perry, T. S., Alvarez, S. A., Hargrove, D., Mazuch, J. R., Nikitin, A., and Bell, P. M., *Point Projection Radiography with the FXI*, Lawrence Livermore National Laboratory, Livermore, CA, UCRL-JC-123135. Prepared for the 11th Topical Conf on High Temperature Plasma Diagnostics, Monterey, CA, May 12–16, 1996.

Budil, K. S., Remington, B. A., Peyser, T. A., Mikaelian, K. O., Rubenchik, A. M., Berning, M., and Wood-Vasey, M. W., *Experimental Investigation of the Classical Rayleigh-Taylor Instability*, Lawrence Livermore National Laboratory, Livermore, CA, UCRL-JC-123293. Prepared for the 24th European Conf on Laser Interaction with Matter, Madrid, Spain, Jun 3–7, 1996.

Budil, K. S., Remington, B. A., Perry, T. S., Rubenchik, A. M., Berning, M., Peyser, T. A., Louis, H., Demir, T., and Wallace, R., *A Novel Method for Diagnosing the Growth of Subresolution-Scale Perturbations*, Lawrence Livermore National Laboratory, Livermore, CA, UCRL-JC-124033. Prepared for the 11th Topical Conf on High-Temperature Plasma Diagnostics, Monterey, CA, May 12–14, 1996.

Budil, K. S., Remington, B. A., Rubenchik, A. M., Berning, M., Wood-Vasey, W. M., Miller, P. L., Perry, T. S., Peyser, T. A., and Mikaelian, K. O., *Multimode Classical Rayleigh-Taylor Experiments at Nova*, Lawrence Livermore National Laboratory, Livermore, CA, UCRL-JC-124278 ABS. Prepared for the 26th Anomalous Absorption Conf, Fairbanks, AK, Aug 26–30, 1996.

Burnham, A. K., Tobin, M. T., Anderson, A. T., Honea, E. C., Skulina, K. M., Milam, D., Evans, M., Rainer, F., and Gerassimenko, M., *Development and Evaluation of First Wall Materials for the National Ignition Facility*, Lawrence Livermore National Laboratory, Livermore, CA, UCRL-JC-123561. Prepared for the American Nuclear Society 12th Topical Mtg on the Technology of Fusion Energy, Reno, NV, Jun 16–20, 1996.

Busby, L. E., *Gist: a Scientific Graphics Package for Python*, Lawrence Livermore National Laboratory, Livermore, CA, UCRL-JC-124008 ABS. Prepared for the 4th Intl Python Workshop, Livermore, CA, Jun 3–6, 1996.

Busby, L. E., *Gist: a Scientific Graphics Package for Python*, Lawrence Livermore National Laboratory, Livermore, CA, UCRL-JC-124228. Prepared for the 4th Intl Python Workshop, Livermore, CA, Jun 3–6, 1996.

C

Cable, M. D., Barbee, T. W., Lerche, R. A., Nelson, M. B., Moran, M. J., Ress, D. B., Sangster, T. C., Trebes, J. E., Turner, R. E., Phillips, T. W., Hicks, D., Li, C. K., Petrasso, R. D., and Seguin, F., *Diagnostics for High Density Implosions at the National Ignition Facility*, Lawrence Livermore National Laboratory, Livermore, CA, UCRL-JC-124239 SUM. Prepared for the 16th Intl Atomic Energy Agency Fusion Energy Conf on Plasma Physics and Controlled Nuclear Fusion Research, Montreal, Canada, Oct 7–11, 1996.

- Caird, J. A., Auerbach, J. M., Behrendt, W. C., Bliss, E. S., Barker, C., Campbell, J. H., Hackel, R. P., Hartley, R. G., Hennesian, M. A., Hinz, A. F., Hunt, J. T., Kartz, M. W., Lawson, J. K., Mathieu, F., Murray, J. E., Pollock, G. G., Powell, H. T., Salmon, J. T., Smith, I. C., and Speck, D. R., *The Beamlet Laser System as a Prototype for the National Ignition Facility (NIF)*, Lawrence Livermore National Laboratory, Livermore, CA, UCRL-JC-124500 ABS & SUM. Prepared for the 9th Annual Mtg of the IEEE Lasers and Electro-Optics Society, Boston, MA, Nov 18–21, 1996.
- Campbell, E. M., Holmes, N. C., Libby, S. B., Remington, B. A., and Teller, E., *The Evolution of High Energy-Density Physics: from Nuclear Testing to the Superlasers*, Lawrence Livermore National Laboratory, Livermore, CA, UCRL-JC-124258. Submitted to *Laser and Particle Beams*.
- Campbell, J. H., *Recent Advances in Phosphate Laser Glasses for High Power Applications*, Lawrence Livermore National Laboratory, Livermore, CA, UCRL-JC-124244. Prepared for the Society of Photo-Optical Instrumentation Engineers 1996 Intl Symp on Optical Science, Engineering and Instrumentation, Denver, CO, Aug 4–9, 1996.
- Celliers, P., Da Silva, L. B., Heredia, N. J., Mammini, B. M., London, R. A., and Strauss, M., *Dynamics of Laser-Induced Transients Produced by Nanosecond Duration Pulses*, Lawrence Livermore National Laboratory, Livermore, CA, UCRL-JC-124047. Prepared for the Society of Photo-Optical Instrumentation Engineers '96 Conf, San Jose, CA, Jan 28–Feb 2, 1996.
- Celliers, P. M., Da Silva, L. B., Hammel, B. A., Cauble, R., Ng, A., Chiu, G., Forsman, A., and Chandler, G., *Interferometric Techniques for Probing Laser-Generated Shocks in Transparent Solids*, Lawrence Livermore National Laboratory, Livermore, CA, UCRL-JC-124030 ABS. Prepared for the 24th European Conf on Laser Interaction with Matter, Madrid, Spain, Jun 3–7, 1996.
- Celliers, P. M., Da Silva, L., Dane, C. B., Norton, M., Mrowka, S., Harder, J., Hackel, L., Matthews, D., Abate, J., and Moldonado, J., *X-Ray Conversion Efficiency Using a High Average Power Nd:glass Laser System*, Lawrence Livermore National Laboratory, Livermore, CA, UCRL-JC-122656 ABS Rev. 1. Prepared for the 23rd IEEE Intl Conf on Plasma Science, Boston, MA, Jun 3–5, 1996.
- Clark, G. A., Glinsky, M. E., Sandhya Devi, K. R., Robinson, J. H., Cheng, P. K. Z., and Ford, G. E., *Automatic Event Picking in Pre-Stack Migrated Gathers Using a Probabilistic Neural Network*, Lawrence Livermore National Laboratory, Livermore, CA, UCRL-JC-124022. Prepared for the 1996 Society of Exploration Geophysicists, Denver, CO, Nov 10–15, 1996.
- Collins, G. W., Bernat, T. P., Mapoles, E. R., and Duriez, C., *Heat-Flux Induced Changes to Multicrystalline D₂ Surfaces*, Lawrence Livermore National Laboratory, Livermore, CA, UCRL-JC-124261. Submitted to *Phys. Rev. Lett.*
- Collins, G. W., Bittner, D. N., Monsler, E., Tiszauer, D., Feit, M., Mapoles, E., and Bernat, T. P., *Forming and Smoothing D₂ and HD Layers for ICF by Infra-Red Heating*, Lawrence Livermore National Laboratory, Livermore, CA, UCRL-JC-124255. Prepared for the 24th European Conf on Laser Interaction with Matter, Madrid, Spain, Jun 3–7, 1996.
- Colvin, J., Hogan, W., Perry, M., and Tabak, M., *Inertial Fusion Energy Development at LLNL: the National Ignition Facility, 100-1000 TW Lasers, and Fast Ignitor Physics*, Lawrence Livermore National Laboratory, Livermore, CA, UCRL-JC-124285 ABS. Prepared for the 8th Intl Conf on Emerging Nuclear Energy Systems, Obninsk, Russia, Jun 24–28, 1996.
- Correll, D., *1995 ICF Annual Report*, Lawrence Livermore National Laboratory, Livermore, CA, UCRL-LR-105820-95.
- Crane, J., Martinez, M., Moran, B., Laumann, C., Davin, J., Rothenberg, J., Beach, R., Golick, B., Jones, R., Wing, R., Braucht, J., Skulina, K., and Mitchell, S., *High-Gain, Nd-Doped-Glass Preamplifier for the National Ignition Facility (NIF) Laser System*, Lawrence Livermore National Laboratory, Livermore, CA, UCRL-JC-124483 ABS & SUM. Prepared for the Lasers and Electro-Optics Society '96, Boston, MA, Nov 18–21, 1996.

D

- Da Silva, L. B., Barbee, T. W., Cauble, R., Celliers, P., Decker, C. D., London, R. A., Moreno, J. C., Trebes, J. E., Wan, A. S., and Weber, F., *Applications of Soft X-Ray Lasers for Probing High Density Plasmas*, Lawrence Livermore National Laboratory, Livermore, CA, UCRL-JC-124006 ABS. Prepared for the 5th Intl Conf on X-Ray Lasers, Lund, Sweden, Jun 10–14, 1996.

Da Silva, L. B., Barbee, T. W., Cauble, R., Celliers, P., Decker, C. D., London, R. A., Moreno, J. C., Trebes, J. E., Wan, A. S., and Weber, F., *Electron Density Measurements Using Soft X-Ray Lasers*, Lawrence Livermore National Laboratory, Livermore, CA, UCRL-JC-124028 ABS. Prepared for the 24th European Conf on Laser Interaction with Matter, Madrid, Spain, Jun 3–7, 1996.

Da Silva, L. B., Barbee, T. W., Cauble, R., Celliers, P., Kalantar, D. H., Key, M. H., Libby, S., Matthews, D. L., Moreno, J. C., Trebes, J. E., Wan, A. S., and Weber, F., *Application of X-Ray Laser to Probe High Density Plasmas*, Lawrence Livermore National Laboratory, Livermore, CA, UCRL-JC-124048 ABS. Prepared for the 23rd IEEE Intl Conf on Plasma Science, Boston, MA, Jun 3–5, 1996.

Da Silva, L. B., Stuart, B. C., Celliers, P. M., Chang, T. D., Feit, M. D., Glinsky, M. E., Heredia, N. J., Herman, S., Lane, S. M., London, R. A., Matthews, D. L., Neev, J., Perry, M. D., and Rubenchik, A. M., *Comparison of Soft and Hard Tissue Ablation with Sub-ps and ns Pulse Lasers*, Lawrence Livermore National Laboratory, Livermore, CA, UCRL-JC-124044. Prepared for the Society of Photo-Optical Instrumentation Engineers '96 Conf, San Jose, CA, Jan 28–Feb 2, 1996.

Davis, J. F., *Final Report Facilitization of the National Ignition Facility (NIF) for Radiation Sciences Experiments*, Lawrence Livermore National Laboratory, Livermore, CA, UCRL-CR-123781.

Decker, C. D., and London, R. A., *Design Calculations of a Compact Ni-Like Tungsten Soft X-Ray Laser*, Lawrence Livermore National Laboratory, Livermore, CA, UCRL-JC-124489 ABS. Prepared for the 26th Annual Anomalous Absorption Conf, Fairbanks, AK, Aug 26–30, 1996.

Decker, C. D., Mori, W. B., Tzeng, K. C., and Katsouleas, T., *Modeling Single-Frequency Laser-Plasma Acceleration Using Particle-in-Cell Simulations: the Physics of Beam Breakup*, Lawrence Livermore National Laboratory, Livermore, CA, UCRL-JC-124016. Submitted to *Transactions on Plasma Science*.

Dixit, S., and Feit, M., *Synthesis of Fully Continuous Phase Screens for Tailoring the Focal Plane Irradiance Profiles*, Lawrence Livermore National Laboratory, Livermore, CA, UCRL-JC-124012. Prepared for the 1996 Diffractive Optics and Micro Optics Topical Mtg, Boston, MA, Apr 29–May 2, 1996.

Dixit, S. N., Feit, M. D., Perry, M. D., and Powell, H. T., *Designing Fully Continuous Phase Screens for Tailoring Focal Plane Irradiance Profiles*, Lawrence Livermore National Laboratory, Livermore, CA, UCRL-JC-123842. Submitted to *Opt Lett*.

Dixit, S. N., Feit, M. D., Perry, M. D., and Powell, H. T., *Designing Fully Continuous Phase Screens for Tailoring Focal Plane Irradiance Profiles*, Lawrence Livermore National Laboratory, Livermore, CA, UCRL-JC-123842 Rev. 1. Submitted to *Opt Lett*.

Dubois, P. F., *Introduction to Python*, Lawrence Livermore National Laboratory, Livermore, CA, UCRL-JC-124262. Prepared for the 4th Intl Python Workshop, Livermore, CA, Jun 3–6, 1996.

Dubois, P. F., *Object Technology for Scientific Computing*, Lawrence Livermore National Laboratory, Livermore, CA, UCRL-JC-124451. Prepared for the Tools USA '96, Santa Barbara, CA, Jul 28–Aug 2, 1996.

Dubois, P. F., and Yang, T.-Y. B., *Extending Python*, Lawrence Livermore National Laboratory, Livermore, CA, UCRL-JC-123346. Submitted to *Comput. Phys*.

E

Emanuel, M. A., Carlson, N. W., and Skidmore, J. A., *High Efficiency AlGaAs-Based Laser Diode at 808 nm with Large Transverse Spot Size*, Lawrence Livermore National Laboratory, Livermore, CA, UCRL-JC-124003. Submitted to *IEEE Photonics Technology Letters*.

Estabrook, K. G., Celliers, P., Murray, J., Wallace, R., Stone, G., Van Wouterghem, B., MacGowan, B., Hunt, J., and Manes, K., *An Improved Pinhole Spatial Filter*, Lawrence Livermore National Laboratory, Livermore, CA, UCRL-JC-124475 ABS. Prepared for the 26th Annual Anomalous Absorption Conf, Fairbanks, AK, Aug 26–30, 1996.

Estabrook, K. G., Glenzer, S. H., Back, C. A., MacGowan, B. J., Montgomery, D. S., Stone, G. F., Moody, J. D., and Kirkwood, R. K., *Electron Temperature and Density Measurements in Large Scale-Length Gasbag Plasmas by K-Shell Spectroscopy*, Lawrence Livermore National Laboratory, Livermore, CA, UCRL-JC-124474 ABS. Prepared for the 26th Annual Anomalous Absorption Conf, Fairbanks, AK, Aug 26–30, 1996.

F

Ficini, G., and Campbell, J. H., *Development of Large Scale Production of Nd-Doped Phosphate Glasses for Megajoule-Scale Laser Systems*, Lawrence Livermore National Laboratory, Livermore, CA, UCRL-JC-124027. Prepared for the EUROPTO Conf, Berlin, Germany, May 13–17, 1996. Submitted to *European Optical Society and The Intl Society for Optical Engineering*.

Franco, E. D., Ryon, R. W., Janssens, L. V., and Janssens, K., *Capillary Optics for Microanalysis Applications*, Lawrence Livermore National Laboratory, Livermore, CA, UCRL-JC-124358 ABS. Prepared for the *European Conf on X-Ray Spectrometry*, Universidade de Lisboa, Portugal, Jun 23–29, 1996.

G

Glendinning, S. G., Powers, L. V., Kauffman, R. L., Landen, O. L., Ress, D. B., Stone, G. F., Suter, L. J., and Richard, A. L., *Measurements of Wall X-Ray Emission Patterns in Gas-Filled Hohlraums*, Lawrence Livermore National Laboratory, Livermore, CA, UCRL-JC-123021. Submitted to *Phys. Rev. Lett.*

Glenzer, S. H., Back, C. A., Estabrook, K. G., and MacGowan, B. J., *Thomson Scattering in the Corona of Laser-Produced Gold Plasmas*, Lawrence Livermore National Laboratory, Livermore, CA, UCRL-JC-123282. Prepared for the *11th Topical Conf on High Temperature Plasma Diagnostics*, Monterey, CA, May 12–16, 1996.

Glenzer, S. H., Back, C. A., Estabrook, K. G., Wallace, R., Baker, K., MacGowan, B. J., Hammel, B. A., Cid, R. E., and DeGroot, J. S., *Thomson Scattering from Two Species Laser-Produced Plasmas*, Lawrence Livermore National Laboratory, Livermore, CA, UCRL-JC-123752 ABS Rev. 1. Prepared for the *26th Annual Anomalous Absorption Conf*, Fairbanks, AK, Aug 26–30, 1996.

Glenzer, S. H., Back, C. A., Estabrook, K. G., Wallace, R., Baker, K., MacGowan, B. J., Hammel, B. A., Cid, R. E., and DeGroot, J. S., *Observation of Two Ion Acoustic Waves in a Two-Species Laser-Produced Plasma with Thomson Scattering*, Lawrence Livermore National Laboratory, Livermore, CA, UCRL-JC-124283. Submitted to *Phys. Rev. Lett.*

H

Hammer, J. H., Eddleman, J. L., Tabak, M., Toor, A., Zimmerman, G. B., and DeGroot, J. S., *Sheath Broadening in Imploding Z-Pinches due to Large-Bandwidth Rayleigh-Taylor Instability*, Lawrence Livermore National Laboratory, Livermore, CA, UCRL-JC-123519. Prepared for the *Institute of Plasma Physics*, Czech, Republic, Jun 10–14, 1996.

Hatchett, S. P., Moody, J. D., Hammer, J. H., and Tabak, M., *Designs for Hole-Boring and Integrated Fast Ignitor Experiments*, Lawrence Livermore National Laboratory, Livermore, CA, UCRL-JC-124485 ABS. Prepared for the *26th Annual Anomalous Absorption Conf*, Fairbanks, AK, Aug 26–30, 1996.

Hinkel, D. E., Still, C. H., Afeyan, B. B., Berger, R. L., Langdon, A. B., and Williams, E. A., *Simulation of Filamentation in Plasmas with Transverse and Axial Flows*, Lawrence Livermore National Laboratory, Livermore, CA, UCRL-JC-124473 ABS. Prepared for the *26th Annual Anomalous Absorption Conf*, Fairbanks, AK, Aug 26–30, 1996.

Hinkel, D. E., Williams, E. A., Berger, R. L., and Langdon, A. B., *Filamentation and Beam Deflection in Flowing Plasmas: Latest Results*, Lawrence Livermore National Laboratory, Livermore, CA, UCRL-JC-124466 ABS. Prepared for the *26th Annual Anomalous Absorption Conf*, Fairbanks, AK, Aug 26–30, 1996.

Hsieh, E. J., Greenfield, B. J., Behymer, R. D., Lindsey, E. F., and King, C. M., *The Coating Structure and H₂ Fill Characteristics of Be Micro Shells Produced by Sputter Coating with Gas Pulsing*, Lawrence Livermore National Laboratory, Livermore, CA, UCRL-JC-124227 ABS. Prepared for the *American Vacuum Society 43rd Natl Symp*, Philadelphia, PA, Oct 14–18, 1996.

K

Kalantar, D. H., Bell, P. M., Costa, R., Landen, O. L., and Orzechowski, T. J., *Characterization of X-Ray Streak Cameras for Use on Nova*, Lawrence Livermore National Laboratory, Livermore, CA, UCRL-JC-123776 ABS. Prepared for the *22nd Intl Congress on High Speed Photography and Photonics*, Santa Fe, NM, Oct 27–Nov 1, 1996.

Kalantar, D. H., Da Silva, L. B., Glendinning, S. G., Weber, F., Remington, B. A., Weber, S. V., Key, M. H., Neely, D., Wolfrum, E., Demir, A., Lin, J., Smith, R., Tallents, G. J., Kim, N., Zhang, J., Wark, J. S., McPhee, A., Warwich, J., Lewis, C. L. S., and Knauer, J. P., *XUV Probing of Laser Imprint in a Thin Foil Using an X-Ray Laser Backlighter*, Lawrence Livermore National Laboratory, Livermore, CA, UCRL-JC-123284. Prepared for the *11th Topical Conf on High Temperature Plasma Diagnostics*, Monterey, CA, May 12–16, 1996.

Kalantar, D. H., Da Silva, L. B., Glendinning, S. G., Weber, F., Remington, B. A., Weber, S. V., Wolfrum, E., Key, M. H., Neely, D., Kim, N. S., Wark, J. S., Zhang, J., Lewis, C. L. S., McPhee, A., Warwich, J., Demir, A., Lin, J., Smith, R., Tallents, G. J., and Knauer, J. P., *Measurements on Laser Imprint by XUV Radiography Using an X-Ray Laser*, Lawrence Livermore National Laboratory, Livermore, CA, UCRL-JC-123289. Prepared for the *24th European Conf on Laser Interaction with Matter*, Madrid, Spain, Jun 3–7, 1996.

Kalantar, D. H., Da Silva, L. B., Glendinning, S. G., Weber, F., Remington, B. A., Weber, S. V., Key, M. H., Neely, D., Wolfrum, E., Demir, A., Lin, J., Smith, R., Tallents, G. J., Kim, N. S., Wark, J. S., Zhang, J., Lewis, C. L. S., McPhee, A., Warwick, J., and Knauer, J. P., *Measurements of Laser Imprint in a Thin Foil Using an X-Ray Laser for XUV Radiography*, Lawrence Livermore National Laboratory, Livermore, CA, UCRL-JC-124288 ABS. Prepared for the 26th Annual Anomalous Absorption Conf, Fairbanks, AK, Aug 26–30, 1996.

Kalantar, D. H., Demir, A., Key, M. H., Kim, N. S., Lewis, C. L. S., Lin, J., Neely, D., McPhess, A., Remington, B. A., Smith, R., Talents, G. J., Wark, J. S., Warwick, J., Weber, S. V., Wolfrum, E., and Zhang, J., *XUV Radiography Measurements of Direct Drive Imprint in Thin Aluminum Foils Using a GE X-Ray Laser on Vulcan*, Lawrence Livermore National Laboratory, Livermore, CA, UCRL-ID-123779.

Kalantar, D. H., Haan, S. W., Hammel, B. A., Landen, O. L., Keane, C. J., and Munro, D. H., *X-Ray Backlit Imaging Measurement of In-Flight Pusher Density for an Indirect Drive Capsule Implosion*, Lawrence Livermore National Laboratory, Livermore, CA, UCRL-JC-123285. Prepared for the 11th Topical Conf on High Temperature Plasma Diagnostics, Monterey, CA, May 12–16, 1996.

Kalantar, D. H., Haan, S. W., Hammel, B. A., Keane, C. J., Landen, O. L., and Munro, D. H., *Measurement of the In-Flight Pusher Density of an Indirect Drive Capsule Implosion Core Using X-Ray Backlighting*, Lawrence Livermore National Laboratory, Livermore, CA, UCRL-JC-123294. Prepared for the 24th European Conf on Laser Interaction with Matter, Madrid, Spain, Jun 3–7, 1996.

Kauffman, R. L., Glendinning, S. G., Powers, L. V., Berger, R. L., Hinkel, D. E., Landen, O. L., Ress, D., Suter, L. J., Shepard, T. D., Williams, E. A., Richard, A. L., and Blain, M. A., *Effects of Beam Conditioning on Wall Emission from Gas-Filled Hohlräume*, Lawrence Livermore National Laboratory, Livermore, CA, UCRL-JC-124468 ABS. Prepared for the 26th Annual Anomalous Absorption Conf, Fairbanks, AK, Aug 26–30, 1996.

Keane, C. J., *Applications of Plasma Spectroscopy to the Study of High Energy Density Matter*, Lawrence Livermore National Laboratory, Livermore, CA, UCRL-JC-123782 ABS. Prepared for the Intl Seminar on Physics of High Energy Density Matter, Vancouver, Canada, May 26–29, 1996.

Kilkenny, J. D., Bernat, T. P., Hammel, B. A., Kauffman, R. L., Landen, O. L., MacGowan, B. J., Orzechowski, T. J., Powers, L. V., Rosen, M. D., and Suter, L. J., *The Status of the ICF Target Physics Program at Lawrence Livermore National Laboratory*, Lawrence Livermore National Laboratory, Livermore, CA, UCRL-JC-123543. Prepared for the 24th European Conf on Laser Interaction with Matter, Madrid, Spain, Jun 3–7, 1996.

Kirkwood, R. K., Afeyan, B. B., Back, C. A., Blain, M. A., Estabrook, K. G., Glenzer, S. H., Kruer, W. L., MacGowan, B. J., Montgomery, D. S., Moody, J. D., and Williams E. A., *The Effect of Ion Wave Damping on Stimulated Raman Scattering in High Z Laser Produced Plasmas*, Lawrence Livermore National Laboratory, Livermore, CA, UCRL-JC-124019. Submitted to *Phys. Rev. Lett.*

Kirkwood, R. K., Afeyan, B. B., Back, C. A., Blain, M. A., Berger, R. L., Estabrook, K. G., Glenzer, S. H., Kruer, W. L., Lasinski, B. F., MacGowan, B. J., Montgomery, D. S., Moody, J. D., Wallace, R., and Williams, E. A., *Saturation of SRS by the Stimulation of Ion Waves in Ignition Relevant Plasmas*, Lawrence Livermore National Laboratory, Livermore, CA, UCRL-JC-124297 ABS. Prepared for the 26th Annual Anomalous Absorption Conf, Fairbanks, AK, Aug 26–30, 1996.

Kirkwood, R. K., Back, C. A., Glenzer, S. H., MacGowan, B. J., Montgomery, D. S., and Moody, J. D., *Imaging Back Scattered and Near Back Scattered Light in Ignition Scale Plasmas*, Lawrence Livermore National Laboratory, Livermore, CA, UCRL-JC-124041. Prepared for the 11th Topical Conf on High Temperature Plasma Diagnostics, Monterey, CA, May 12–16, 1996.

Kruer, W. L., Afeyan, B. B., Wilks, S. C., and Chou, A., *Strongly-Driven Laser Plasmas with Self-Consistent Electron Distribution*, Lawrence Livermore National Laboratory, Livermore, CA, UCRL-JC-124491 ABS. Prepared for the 26th Annual Anomalous Absorption Conf, Fairbanks, AK, Aug 26–30, 1996.

L

Land, T., Malkin, A., Kuznetsov, Y., McPherson, A., and De Yoreo, J., *Mechanisms of Protein and Virus Crystal Growth; an Atomic Force Microscopy Study of Canavalin and STMV Crystals*, Lawrence Livermore National Laboratory, Livermore, CA, UCRL-JC-124110. Prepared for the 11th Intl Conf on Crystal Growth, The Hague, the Netherlands, Jun 1995. Submitted to *J. of Crystal Growth*.

- Land, T., Malkin, A. J., Kuznetsov, Y. G., McPherson, A., and De Yoreo, J. J., *Investigation of Virus Crystal Growth Mechanisms by In Situ Atomic Force Microscopy*, Lawrence Livermore National Laboratory, Livermore, CA, UCRL-JC-121141. Submitted to *Phys. Rev. Lett.*
- Landen, O. L., Lobban, A., Bell, P., and Costa, R., *Simple Model for X-Ray Sensitivity of Microchannel Plate-Based X-Ray Framing Cameras*, Lawrence Livermore National Laboratory, Livermore, CA, UCRL-JC-123777 ABS. Prepared for the 22nd Intl Congress on High Speed Photography and Photonics, Santa Fe, NM, Oct 27–Nov 1, 1996.
- Langdon, A. B., and Williams, E. A., *Spot and Speckle Motion in SSD Illumination*, Lawrence Livermore National Laboratory, Livermore, CA, UCRL-JC-124453 ABS. Prepared for the 26th Annual Anomalous Absorption Conf, Fairbanks, AK, Aug 26–30, 1996.
- Langer, S. H., Keane, C. J., Scott, H. A., *Yield and Emission Line Ratios from ICF Target Implosions with Multi-Mode Raleigh-Taylor Perturbations*, Lawrence Livermore National Laboratory, Livermore, CA, UCRL-JC-124484 ABS. Prepared for the 26th Annual Anomalous Absorption Conf, Fairbanks, AK, Aug 26–30, 1996.
- Lasinski, B. F., Cohen, B. I., Langdon, A. B., and Williams, E. A., *Stimulated Brillouin Scatter in PIC-Fluid Simulations*, Lawrence Livermore National Laboratory, Livermore, CA, UCRL-JC-124457 ABS. Prepared for the 26th Annual Anomalous Absorption Conf, Fairbanks, AK, Aug 26–30, 1996.
- Latkowski, J. F., Sanz, J., Vujic, J. L., and Tobin, M. T., *Sequential Charged-Particle and Neutron Activation of Flibe in the HYLIFE-II Inertial Fusion Energy Power Plant Design*, Lawrence Livermore National Laboratory, Livermore, CA, UCRL-JC-123558. Prepared for the American Nuclear Society 12th Topical Mtg on the Technology of Fusion Energy, Reno, NV, Jun 16–20, 1996.
- Latkowski, J. F., and Tobin, M. T., *Time and Motion Study for the National Ignition Facility Target Area*, Lawrence Livermore National Laboratory, Livermore, CA, UCRL-JC-123552. Prepared for the American Nuclear Society Intl Topical Mtg on Probabilistic Safety Assessment '96, Park City, UT, Sept 29–Oct 3, 1996.
- Lawson, J. K., Aikens, D. M., English, R. E., and Wolfe, C. R., *Power Spectral Density Specifications for High-Power Laser Systems*, Lawrence Livermore National Laboratory, Livermore, CA, UCRL-JC-123105. Prepared for the Intl Symp on Optical Systems Design and Production II, Glasgow, Scotland, May 12–16, 1996.
- Lerche, R. A., *Neutron-Induced Noise in NIF-Class Diagnostic Instruments*, Lawrence Livermore National Laboratory, Livermore, CA, UCRL-JC-123556. Prepared for the 11th Topical Conf on High-Temperature Plasma Diagnostics, Monterey, CA, May 12–16, 1996.
- Lerche, R. A., Ehrlich, R. B., Laumann, C. W., and Miller, J. L., *Streak Camera Power Measurements for Large-Aperture, High-Power Laser Beams*, Lawrence Livermore National Laboratory, Livermore, CA, UCRL-JC-124240 ABS. Prepared for the 22nd Intl Conf on High-Speed Photography and Photonics, Santa Fe, NM, Oct 27–Nov 1, 1996.
- Liang, E. P., Wilks, S. C., and Tabak, M., *Pair Production by Ultra-Intense Lasers*, Lawrence Livermore National Laboratory, Livermore, CA, UCRL-JC-124499. Submitted to *Phys. Rev. Lett.*
- Lindl, J. D., *Progress on the Physics of Ignition for Radiation Driven Inertial Confinement Fusion (ICF) Targets*, Lawrence Livermore National Laboratory, Livermore, CA, UCRL-JC-124004 ABS. Prepared for the 16th Intl Atomic Energy Agency Fusion Energy Conf on Plasma Physics and Controlled Nuclear Fusion Research, Montreal, Canada, Oct 7–11, 1996.
- Lindl, J. D., and Campbell, E. M., *Inertial Confinement Fusion with High Powered Lasers*, Lawrence Livermore National Laboratory, Livermore, CA, UCRL-JC-124461. Submitted to *Scientific American*.
- Logan, B. G., Lindl, J. D., and Meier, W. R., *Inertial Fusion Energy Development Approaches for Direct and Indirect-Drive*, Lawrence Livermore National Laboratory, Livermore, CA, UCRL-JC-123788 EXT ABS. Prepared for the 16th Intl Atomic Energy Agency Fusion Energy Conf on Plasma Physics and Controlled Nuclear Fusion Research, Montreal, Canada, Oct 7–11, 1996.
- Logory, L. M., Bell, P. M., Conder, A. D., and Lee, F. D., *Development and Characterization of a CCD Camera System for Use on Six-Inch Manipulator Systems*, Lawrence Livermore National Laboratory, Livermore, CA, UCRL-JC-123281. Prepared for the 11th Topical Conf on High Temperature Plasma Diagnostics, Monterey, CA, May 12–16, 1996.

M

- MacGowan, B. J., *Laser Scattering in Large-Scale-Length Plasmas Relevant to National Ignition Facility Hohlräume*, Lawrence Livermore National Laboratory, Livermore, CA, UCRL-JC-123545 ABS Rev. 1. Prepared for the 16th Intl Atomic Energy Agency Fusion Energy Conf on Plasma Physics and Controlled Nuclear Fusion Research, Montreal, Canada, Oct 7–11, 1996.

- MacGowan, B. J., Afeyan, B. B., Back, C. A., Blain, M. A., Berger, R. L., Canaud, B., Glenzer, S. H., Hinkel, D. E., Kirkwood, R. K., Kornblum, H. N., Langdon, A. B., Lasinski, B. F., Montgomery, D. S., Moody, J. D., Munro, D. H., Powers, L. V., Rousseaux, C., Still, C. H., Wallace, R. J., and Williams, E. A., *The influence of smoothing by spectral dispersion on laser scattering and beam propagation in large-scale-length plasmas relevant to National Ignition Facility hohlraums*, Lawrence Livermore National Laboratory, Livermore, CA, UCRL-JC-124467 ABS. Prepared for the 26th Annual Anomalous Absorption Conf, Fairbanks, AK, Aug 26–30, 1996.
- Maitland, D. J., Eder, D. C., London, R. A., Glinsky, M. E., and Soltz, B. A., *Dynamic Simulations of Tissue Welding*, Lawrence Livermore National Laboratory, Livermore, CA, UCRL-JC-121630. Prepared for the Society of Photo-Optical Instrumentation Engineers '96 Conf, San Jose, CA, Jan 28–Feb 2, 1996.
- Mapoles, E. R., Sater, J. D., Monsler, E., and Pipes, J., *Reducing Deuterium-Tritium ICF Roughness by Electrical Heating of the Saturated Vapor*, Lawrence Livermore National Laboratory, Livermore, CA, UCRL-JC-124253. Prepared for the 24th European Conf on Laser Interaction with Matter, Madrid, Spain, Jun 3–7, 1996.
- Marcy, H. O., Rosker, M. J., Cunningham, P. H., DeLoach, L. A., Ebberts, C. A., Kanatzidis, M. G., Thomas, C. A., Warren, L. F., Velsko, S. P., and Liao, J.-H., *L-Histidine Tetrafluoroborate: a Solution-Grown "Semiorganic" Crystal for Nonlinear Frequency Conversion*, Lawrence Livermore National Laboratory, Livermore, CA, UCRL-JC-116737. Submitted to *Appl. Phys. Lett.*
- Marinak, M. M., Haan, S. W., Pollaine, S. M., Tipton, R. E., and Zimmerman, G. B., *Three-Dimensional Simulations of National Ignition Facility Capsule Implosions*, Lawrence Livermore National Laboratory, Livermore, CA, UCRL-JC-123783 ABS. Prepared for the 16th Intl Atomic Energy Agency Fusion Energy Conf on Plasma and Controlled Nuclear Fusion Research, Montreal, Canada, Oct 7–11, 1996.
- McEachern, R., and Correll, D., *Inertial Confinement Fusion Quarterly Report*, vol. 6, No. 1, Oct–Dec 1995, Lawrence Livermore National Laboratory, Livermore, CA, UCRL-LR-105821-96-1.
- Meier, W. R., and Logan, B. G., *Developing Inertial Fusion Energy—Where Do We Go From Here?*, Lawrence Livermore National Laboratory, Livermore, CA, UCRL-JC-123079. Prepared for the American Nuclear Society 12th Topical Mtg on the Technology of Fusion Energy, Reno, NV, Jun 16–20, 1996.
- Moody, J. D., MacGowan, B. J., Kirkwood, R. K., and Montgomery, D. S., *Measurements of High Intensity Laser Beam Transmission through Large Scalelength Plasmas*, Lawrence Livermore National Laboratory, Livermore, CA, UCRL-JC-123321. Submitted to *Rev. Sci. Instrum.*
- Moody, J. D., MacGowan, B. J., Berger, R. L., and Munro, D. E., *Optical Spectral Characteristics of Light Transmitted through Nova Gasbag Plasmas*, Lawrence Livermore National Laboratory, Livermore, CA, UCRL-JC-124293 ABS. Prepared for the 26th Annual Anomalous Absorption Conf, Fairbanks, AK, Aug 26–30, 1996.
- Moody, J. D., MacGowan, B. J., Kirkwood, R. K., Back, C. A., Glenzer, S. H., Munro, D. E., and Berger, R. L., *Power Balance Studies of a Nova Gasbag Plasma*, Lawrence Livermore National Laboratory, Livermore, CA, UCRL-JC-124294 ABS. Prepared for the 26th Annual Anomalous Absorption Conf, Fairbanks, AK, Aug 26–30, 1996.
- Moody, J. D., MacGowan, B. J., Berger, R. L., and Munro, D. E., *Analysis of Transmitted Light Angular Divergence in Nova Gasbag Plasmas*, Lawrence Livermore National Laboratory, Livermore, CA, UCRL-JC-124296 ABS. Prepared for the 26th Annual Anomalous Absorption Conf, Fairbanks, AK, Aug 26–30, 1996.
- Moon, S. J., and Eder, D. C., *Target Considerations for Inner-Shell Photo-Ionized X-Ray Lasing*, Lawrence Livermore National Laboratory, Livermore, CA, UCRL-JC-123798 ABS. Prepared for the 5th Intl Conf on X-Ray Lasers, Lund, Sweden, Jun 10–14, 1996.
- Moran, M. J., *Nuclear Diagnostics in Support of ICF Experiments*, Lawrence Livermore National Laboratory, Livermore, CA, UCRL-JC-124232 ABS & VG. Prepared for the 11th Topical Conf on High Temperature Plasma Diagnostics, Monterey, CA, May 12–16, 1996.
- Moran, M. J., *A Thresholded Cherenkov Detector for ICF Diagnostics*, Lawrence Livermore National Laboratory, Livermore, CA, UCRL-JC-124242 ABS. Prepared for the 11th Topical Conf on High Temperature Plasma Diagnostics, Monterey, CA, May 12–16, 1996.
- Moran, M. J., and Hall, J., *Nuclear Diagnostics in Support of ICF Experiments*, Lawrence Livermore National Laboratory, Livermore, CA, UCRL-JC-124232. Prepared for the 11th Topical Conf on High-Temperature Plasma Diagnostics, Monterey, CA, May 12–16, 1996.
- Motteler, Z. C., *A Python Interface with Narcisse Graphics*, Lawrence Livermore National Laboratory, Livermore, CA, UCRL-JC-124001. Prepared for the 4th Intl Python Workshop, Livermore, CA, Jun 3–6, 1996.

N

Neev, J., Nelson, S., Critelli, M., Cheung, E., Carrasco, W. A., Rubenchik, A. M., Da Silva, L. B., Perry, M. D., and Stuart, B. C., *Ablation of Human Nail by Pulsed Lasers*, Lawrence Livermore National Laboratory, Livermore, CA, UCRL-JC-124251. Submitted to *Lasers in Surgery and Medicine*.

O

Orzechowski, T. J., Afeyan, B., Berger, R. L., Blain, M. A., Kirkwood, R. K., Kruer, W. L., MacGowan, B. J., Powers, L. V., Springer, P. S., Rosen, M. D., Moody, J. D., and Suter, L. J., *Energetics of Small, High-Temperature Laser-Driven Hohlraums*, Lawrence Livermore National Laboratory, Livermore, CA, UCRL-JC-124279 ABS. Prepared for the *26th Annual Anomalous Absorption Conf*, Fairbanks, AK, Aug 26–30, 1996.

P

Page, R. H., Schaffers, K. I., DeLoach, L. D., Wilke, G. D., Patel, F. D., Tassano, J. B., Payne, S. A., Krupke, W. F., Chen, K.-T., and Burger, A., *Cr²⁺-Doped Zinc Chalcogenides as Efficient, Widely-Tunable Mid-Infrared Lasers*, Lawrence Livermore National Laboratory, Livermore, CA, UCRL-JC-123768. Submitted to *J. of Quantum Electronics*.

Paisner, J. A., and Powell, H. T., *The National Ignition Facility and Its Laser Technology*, Lawrence Livermore National Laboratory, Livermore, CA, UCRL-JC-123764 ABS Rev. 1. Prepared for the *16th Intl Atomic Energy Agency Conf on Plasma Physics and Controlled Nuclear Fusion Research*, Montreal, Canada, Oct 7–11, 1996.

Payne, S. A., *Materials and Techniques for Scaling Lasers to High Power*, Lawrence Livermore National Laboratory, Livermore, CA, UCRL-JC-124488 ABS. Prepared for the *Materials Research Society Fall Mtg*, Boston, MA, Dec 2–6, 1996.

Payne, S. A., *Conduction Band States and 5d-to-4f Laser Transition of Rare Earth Ion Dopants*, Lawrence Livermore National Laboratory, Livermore, CA, UCRL-JC-124497 ABS. Prepared for the *2nd Intl Conf on Tunable Solid State Lasers*, Warsaw, Poland, Sept 1–4, 1996.

Payne, S. A., and Krupke, W. F., *Beyond the Present: a Glimpse into the Laser-Crystal Ball*, Lawrence Livermore National Laboratory, Livermore, CA, UCRL-JC-124274. Submitted to *Optics & Photonics News*.

Payne, S. A., Page, R. H., Marshall, C. D., Schaffers, K. I., and Krupke, W. F., *New Tunable Laser Materials for Potential Use in LIDAR Systems*, Lawrence Livermore National Laboratory, Livermore, CA, UCRL-JC-124015 ABS. Prepared for the *Society of Photo-Optical Instrumentation Engineers 1996 Intl Symp on Optical Science, Engineering and Instrumentation*, Denver, CO, Aug 4–9, 1996.

Phillips, T. W., Cable, M. D., Hicks, D. G., Li, C. K., Petrasso, R. D., and Seguin, F. H., *A Study of CR-39 Track Response to Charged Particles from Nova Implosions*, Lawrence Livermore National Laboratory, Livermore, CA, UCRL-JC-124231. Prepared for the *11th Topical Conf on High Temperature Plasma Diagnostics*, Monterey, CA, May 12–16, 1996.

Phillips, T. W., Cable, M. D., Hicks, D., Li, C. K., Petrasso, R. D., and Seguin, F., *A Study of Solid-State Track Response to Charge Particles from Nova Implosions*, Lawrence Livermore National Laboratory, Livermore, CA, UCRL-JC-124231 ABS & VG. Prepared for the *11th Topical Conf on High Temperature Plasma Diagnostics*, Monterey, CA, May 12–16, 1996.

Pollaine, S. M., and Haan, S. W., *Selection of Beam Angles for the National Ignition Facility (NIF)*, Lawrence Livermore National Laboratory, Livermore, CA, UCRL-JC-124266 ABS. Prepared for the *26th Annual Anomalous Absorption Conf*, Fairbanks, AK, Aug 26–30, 1996.

Powers, L. V., Back, C. A., Berger, R. L., Glendinning, S. G., Glenzer, S., Hinkel, D. E., Kauffman, R. L., Kruer, W. L., MacGowan, B. J., Orzechowski, T. J., Pollaine, S. M., Ressler, D. B., Shepard, T. D., Suter, L. J., Williams, E. A., Delamater, N. D., Hauer, A. A., Lindman, E. L., Magelssen, G. R., and Murphy, T. J., *Studies of Energetics and Symmetry in Gas-Filled Hohlraums*, Lawrence Livermore National Laboratory, Livermore, CA, UCRL-JC-123784 ABS. Prepared for the *16th Intl Atomic Energy Agency Fusion Energy Conf on Plasma and Controlled Nuclear Fusion Research*, Montreal, Canada, Oct 7–11, 1996.

Powers, L. V., Berger, R. L., Kirkwood, R. K., Kruer, W. L., Langdon, A. B., MacGowan, B. J., Orzechowski, T. J., Rosen, M. D., Springer, P. T., Still, C. H., Suter, L. J., and Williams, E. A., *Radiation Temperature Scaling in Hohlraums for Nova and NIF*, Lawrence Livermore National Laboratory, Livermore, CA, UCRL-JC-123572 ABS Rev. 1. Prepared for the *26th Annual Anomalous Absorption Conf*, Fairbanks, AK, Aug 26–30, 1996.

R

Remington, B. A., Glendinning, S. G., Kalantar, D. H., Budil, K. S., Landen, O. L., Hammel, B. A., Marinak, M. M., Weber, W. V., Keane, C. J., Haan, S. W., Rubenchik, A., Wallace, R. J., Key, M. H., Knauer, J. P., Hsing, W. W., Galmiche, D., Blain, M. A., Kane, J., Arnett, D., and Berning, M., *Hydrodynamic Instability Experiments on the Nova Laser*, Lawrence Livermore National Laboratory, Livermore, CA, UCRL-JC-123775 ABS. Prepared for the 16th Intl Atomic Energy Agency Fusion Energy Conf on Plasma Physics and Controlled Nuclear Fusion Research, Montreal, Canada, Oct 7–11, 1996.

Remington, B. A., Glendinning, S. G., Kalantar, D. H., Budil, K. S., Marinak, M. M., Weber, S. V., Colvin, J., Griswold, D., Knauer, J. P., Key, M., Hsing, W. W., Galmiche, D., Rubenchik, A., Kane, J., Arnett, W. D., and Wood-Vasey, W. M., *Laser-Driven Hydrodynamics Experiments at Nova*, Lawrence Livermore National Laboratory, Livermore, CA, UCRL-JC-124480 ABS. Prepared for the 26th Annual Anomalous Absorption Conf, Fairbanks, AK, Aug 26–30, 1996.

Remington, B. A., Marinak, M. M., Budil, K. S., Wallace, R. J., Weber, S. V., and Robey, H., *Ablation Front Rayleigh-Taylor Experiments in 2D and 3D*, Lawrence Livermore National Laboratory, Livermore, CA, UCRL-JC-124000. Submitted to *Phys. of Plasmas*.

Robey, H. F., Budil, K. S., and Remington, B. A., *Spatial Resolution of Gated X-Ray Pinhole Cameras*, Lawrence Livermore National Laboratory, Livermore, CA, UCRL-JC-123044. Prepared for the 11th Topical Conf on High Temperature Plasma Diagnostics, Monterey, CA, May 12–16, 1996.

Rothenberg, J. E., *A Comparison of Beam Smoothing Methods for Direct Drive Inertial Confinement Fusion*, Lawrence Livermore National Laboratory, Livermore, CA, UCRL-JC-124038. Submitted to *J. of the Optical Society of America B*.

Rothenberg, J. E., and Weber, S. V., *Effects of Beam Smoothing on the Hydrodynamics of Direct Drive Inertial Confinement Fusion*, Lawrence Livermore National Laboratory, Livermore, CA, UCRL-JC-124476 ABS. Prepared for the 26th Annual Anomalous Absorption Conf, Fairbanks, AK, Aug 26–30, 1996.

Rushford, M., Dixit, S., Thomas, I., and Perry, M. D., *Fabrication of Large Aperture Kinoform Phase Plates in Fused Silica for Smoothing Focal Plane Intensity Profiles*, Lawrence Livermore National Laboratory, Livermore, CA, UCRL-JC-124013. Prepared for the 1996 *Diffraction Optics and Micro Optics Topical Mtg*, Boston, MA, Apr 29–May 2, 1996.

S

Sangster, T. C., Cable, M. D., Kilkenny, J. D., Lerche, R. A., Nelson, M. B., Moran, M. J., Ress, D., Trebes, J. E., Turner, R. E., and Phillips, T. W., *Diagnostic Development at LLNL for the National Ignition Facility*, Lawrence Livermore National Laboratory, Livermore, CA, UCRL-JC-124452. Prepared for the 24th European Conf on Laser Interaction with Matter, Madrid, Spain, Jun 3–7, 1996.

Schnittman, J. D., and Pollain, S. M., *Tetrahedral Hohlräume on the NIF*, Lawrence Livermore National Laboratory, Livermore, CA, UCRL-JC-124267 ABS. Prepared for the 26th Annual Anomalous Absorption Conf, Fairbanks, AK, Aug 26–30, 1996.

Shepard, T. D., Landen, O. L., Lindl, J. D., Rosen, M. D., and Suter, L. J., *Acceleration of a High-Z Foil by Hydrodynamic Pressure of Radiatively Heated Matter*, Lawrence Livermore National Laboratory, Livermore, CA, UCRL-JC-124494 ABS. Prepared for the 26th Annual Anomalous Absorption Conf, Fairbanks, AK, Aug 26–30, 1996.

Shepard, T. D., and Powers, L. V., *Simulation of Indirectly Driven Implosions Using a Gas-Filled Hohlraum Heated by KPP-Smoothed Laser Beams*, Lawrence Livermore National Laboratory, Livermore, CA, UCRL-JC-124493 ABS. Prepared for the 26th Annual Anomalous Absorption Conf, Fairbanks, AK, Aug 26–30, 1996.

Small, W., Heredia, N. J., Celliers, P. M., Da Silva, L. B., Eder, D. C., Glinsky, M. E., London, R. A., Maitland, D. J., Matthews, D. L., Soltz, B. A., *Laser Tissue Welding Mediated with a Protein Solder*, Lawrence Livermore National Laboratory, Livermore, CA, UCRL-JC-124046. Prepared for the *Society of Photo-Optical Instrumentation Engineers '96 Conf*, San Jose, CA, Jan 28–Feb 2, 1996.

Still, C. H., Berger, R. L., Langdon, A. B., Powers, L. V., Williams, E. A., and Young, P. E., *Laser Filamentation Simulations with Nonlinear Hydrodynamics*, Lawrence Livermore National Laboratory, Livermore, CA, UCRL-JC-124472 ABS. Prepared for the 26th Annual Anomalous Absorption Conf, Fairbanks, AK, Aug 26–30, 1996.

Suter, L. J., Kauffman, R. L., Maxon, M. S., and Davis, J. F., *Efficient Production of 2–10 keV X Rays by Laser Heated "Underdense Radiators,"* Lawrence Livermore National Laboratory, Livermore, CA, UCRL-JC-123590. Prepared for the 24th European Conf on Laser Interaction with Matter, Madrid, Spain, Jun 3–7, 1996.

Suter, L. J., Kauffman, R. L., Maxon, M. S., and Davis, J. F., *Efficient Production of 2–10 keV X Rays by Laser-Heated “Underdense Radiators,”* Lawrence Livermore National Laboratory, Livermore, CA, UCRL-JC-123590 ABS Rev. 1. Prepared for the 26th Annual Anomalous Absorption Conf, Fairbanks, AK, Aug 26–30, 1996.

Suter, L. J., Thiessen, A. R., Ze, F., Kauffman, R., Price, R. H., Rupert, V. C., Slivinsky, V. W., and Wang, C., *Use of Thin Wall Imaging in the Diagnosis of Laser Heated Hohlräume*, Lawrence Livermore National Laboratory, Livermore, CA, UCRL-JC-116323. Prepared for the 11th Topical Conf on High Temperature Plasma Diagnostics, Monterey, CA, May 12–16, 1996.

T

Tabak, M., and Ho, D., *A Distributed Radiator Heavy Ion Target Design*, Lawrence Livermore National Laboratory, Livermore, CA, UCRL-JC-124460 ABS. Prepared for the 26th Annual Anomalous Absorption Conf, Fairbanks, AK, Aug 26–30, 1996.

Tobin, M., Karpenko, V., Foley, D., Anderson, A., Burnham, A., Reitz, T., Latkowski, J., and Bernat, T., *Confinement of Ignition and Yield on the National Ignition Facility*, Lawrence Livermore National Laboratory, Livermore, CA, UCRL-JC-123562. Prepared for the American Nuclear Society 12th Topical Mtg on the Technology of Fusion Energy, Reno, NV, Jun 16–20, 1996.

Tobin, M., Karpenko, V., Kauffman, R., Anderson, A., Simonson, G., Kruger, H., Davis, J. F., and Hoover, T., *Utility of the National Ignition Facility for Inertial Fusion Energy and Radiation Sciences Experiments*, Lawrence Livermore National Laboratory, Livermore, CA, UCRL-JC-123568. Prepared for the American Nuclear Society 12th Topical Mtg on the Technology of Fusion Energy, Reno, NV, Jun 16–20, 1996.

Tobin, M., Karpenko, V., Burnham, A., and Peterson, R., *Target Area Design Issues for Implementing Direct Drive on the National Ignition Facility*, Lawrence Livermore National Laboratory, Livermore, CA, UCRL-JC-124479. Prepared for the American Nuclear Society 12th Topical Mtg on the Technology of Fusion Energy, Reno, NV, Jun 16–20, 1996.

Tobin, M. T., Anderson, A., Burnham, A., and Bernat, T., *Assessment of First Wall Damage from Target X-Ray Emission and Scattered Laser Light for the National Ignition Facility*, Lawrence Livermore National Laboratory, Livermore, CA, UCRL-JC-124265. Prepared for the 24th European Conf on Laser Interaction with Matter, Madrid, Spain, Jun 3–7, 1996.

Tobin, M. T., Anderson, A., Burnham, A., Managan, R., Reitz, T., and Bernat, T., *Results of Life-Cycle Testing for the National Ignition Facility First Wall against Damage from Target Emissions and Decontamination Procedures*, Lawrence Livermore National Laboratory, Livermore, CA, UCRL-JC-124241 SUM. Prepared for the 16th Intl Atomic Energy Agency Fusion Energy Conf on Plasma Physics and Controlled Nuclear Fusion Research, Montreal, Canada, Oct 7–11, 1996.

Tokheim, R. E., Seaman, L., and Curran, D. R., *NIF Target Area Design Support*, Lawrence Livermore National Laboratory, Livermore, CA, UCRL-CR-124257.

W

Weber, F. A., Da Silva, L. B., Barbee, T. W., Ciarlo, D., and Mantler, M., *Quantitative XRFA of Carbon in a Special Matrix by the Fundamental Parameter Method*, Lawrence Livermore National Laboratory, Livermore, CA, UCRL-JC-124249. Prepared for the 44th Annual Denver X-Ray Conf, Colorado Springs, CO, Jul 31–Aug 4, 1995.

Weber, S. V., Glendinning, S. G., Kalantar, D. H., Remington, B. A., Rothenberg, J. E., Key, M. H., Wolfram, E., Verdon, C. P., and Knauer, J. P., *Simulations of Laser Imprint on Nova, Vulcan, and NIF*, Lawrence Livermore National Laboratory, Livermore, CA, UCRL-JC-124490 ABS. Prepared for the 26th Annual Anomalous Absorption Conf, Fairbanks, AK, Aug 26–30, 1996.

Wharton, K., Zakharenkov, Y., Brown, C., Hammel, B., Joshi, C., Moody, J., Offenberger, A., Perry, M., Wilks, S., and Yanovsky, V., *Investigation of the Conversion of Laser Energy to Relativistic Electrons at Intensities of 1020 W/cm²*, Lawrence Livermore National Laboratory, Livermore, CA, UCRL-JC-124295 ABS. Prepared for the 26th Annual Anomalous Absorption Conf, Fairbanks, AK, Aug 26–30, 1996.

Wilcox, R. B., and Browning, D. F., *A Single Frequency, Fiber Ring Laser in Yb:Silica*, Lawrence Livermore National Laboratory, Livermore, CA, UCRL-JC-124236 ABS. Prepared for the 1996 Conf on Lasers and Electro-Optics/Quantum Electronics and Laser Science Conf, Anaheim, CA, Jun 2–7, 1996.

Wilks, S. C., Freeman, R., Hartmann, F., Kerman, A., Langdon, A. B., and Woodworth, J., *Foil-Terminated Free Wave Acceleration*, Lawrence Livermore National Laboratory, Livermore, CA, UCRL-JC-124454 ABS. Prepared for the 26th Annual Anomalous Absorption Conf, Fairbanks, AK, Aug 26–30, 1996.

Wilks, S. C., Kruer, W. L., and Rozmus, W., *Theory and PIC Simulations on the Competition between SBS and SRS*, Lawrence Livermore National Laboratory, Livermore, CA, UCRL-JC-124455 ABS. Prepared for the 26th Annual Anomalous Absorption Conf, Fairbanks, AK, Aug 26–30, 1996.

Wilks, S. C., and Kruer, W. L., *Absorption Mechanisms for Ultra-Intense Laser-Plasma and Solid Target Interactions*, Lawrence Livermore National Laboratory, Livermore, CA, UCRL-JC-124456 ABS. Prepared for the 26th Annual Anomalous Absorption Conf, Fairbanks, AK, Aug 26–30, 1996.

Williams, E. A., Berger, R. L., Afeyan, B. B., Cohen, B. I., Estabrook, K. G., Hinkel, D., Kruer, W. L., Langdon, A. B., Lasinski, B. F., Still, C. H., Yang, B., and Wilks, S., *Theory and Simulation of Laser Plasma Instabilities in Ignition Scale Plasmas*, Lawrence Livermore National Laboratory, Livermore, CA, UCRL-JC-123794 ABS. Prepared for the 16th Intl Atomic Energy Agency Fusion Energy Conf on Plasma Physics and Controlled Nuclear Fusion Research, Montreal, Canada, Oct 7–11, 1996.

Williams, E. A., Cohen, B. I., Berger, R. L., Lasinski, B. F., and Langdon, A. B., *Ion Wave Parametric Instabilities*, Lawrence Livermore National Laboratory, Livermore, CA, UCRL-JC-124471 ABS. Prepared for the 26th Annual Anomalous Absorption Conf, Fairbanks, AK, Aug 26–30, 1996.

Y

Yang, T.-Y. B., Dubois, P. F., and Motteler, Z. C., *Building a Programmable Interface for Physics Codes Using Numeric Python*, Lawrence Livermore National Laboratory, Livermore, CA, UCRL-JC-123785. Prepared for the 4th Intl Python Workshop, Livermore, CA, Jun 3–6, 1996.

Z

Zaitseva, N. P., DeHaven, M. R., Vital, R. L., Carman, M. L., Spears, R., Montgomery, K., Atherton, L. J., and De Yoreo, J. J., *Rapid Growth of Large-Scale (20–50 cm) KDP Crystals*, Lawrence Livermore National Laboratory, Livermore, CA, UCRL-JC-124011 ABS. Prepared for the Nonlinear Optics: Materials, Fundamentals, and Applications, Wailea, Maui, HI, July 8–12, 1996.

Ze, F., Langer, S. H., Kauffman, B. L., Kilkenny, J. D., Ress, D., Rosen, M. D., Suter, L. J., Wallace, R. J., and Wiedwald, J. D., *A Comparative Study of X-Ray Emission from Laser Spots in Laser Heated Hohlraums Relative to Spots on Simple Disk Target*, Lawrence Livermore National Laboratory, Livermore, CA, UCRL-JC-124298. Submitted to *Phys. of Plasmas*.

ICF Program

Lawrence Livermore National Laboratory

P.O. Box 808, L-475

Livermore, California 94551

Address Correction Requested